Multiple weak shock waves induced by heavy ion beams in solid matter

Vom Fachbereich Physik der

TECHNISCHEN UNIVERSITÄT DARMSTADT

zur Erlangung des Grades

eines Doktors der Naturwissenschaften

(Dr.rer.nat.)

genehmigte Dissertation von

Carmen Constantin

aus New York

Darmstadt 2002

D17

Referent:	Professor Dr.Dr.h.c./RUS D.H.H. Hoffmann
Korreferent:	Professor Dr. P. Mulser

Tag der Einreichung:	7.2.2002
Tag der Prüfung:	6.5.2002

Zusammenfassung

Die Erzeugung und Untersuchung von hoher Energiedichte in Materie ist von grundlegender Bedeutung für viele verschiedene Forschungsgebiete, wie die Plasmaphysik, Astrophysik, Geophysik und für Anwendungen wie die Trägheitsfusion als mögliche zukünftige Energiequelle. Relativistische Schwerionenstrahlen sind in vielerlei Hinsicht ideal für die Erzeugung von hoher Energiedichte in Materie geeignet. Aufgrund ihrer großen Reichweite, dringen sie tief in Festkörper ein und erzeugen so relativ große Volumina stark gekoppelter Plasmen.

Das Schwerionensynchrotron SIS-18 an der Gesellschaft für Schwerionenforschung (GSI) stellt intensive Schwerionenstrahlen mit circa 10^9 U^{92+} Ionen in 550 ns kurzen Pulsen zur Verfügung. Als Folge der Energiedeposition von mehr als 1 kJ/g werden Plasmen mit fast Festkörper- dichte bei relativ geringen Temperaturen ($\sim$ 1 eV) erzeugt. Die induzierten Drücke, die im Bereich von einigen zehn kbar liegen, erzeugen schwache Schockwellen, die die Materie bis zu einem Faktor von 1.1 komprimieren. Sie stellen die Grundlage dieser Arbeit dar, die die experimentellen Möglichkeiten zur Untersuchung schwerionengeheizter Festkörpertargets beschreibt. Eine Vielzahl verschiedener Diagnostik-Verfahren wurde angewandt, um die Druckwellen zu untersuchen, die von dem Schwerionenstrahl in mehrschichtigen Targets induziert und für eine kalte Kompression verwendet werden. Der Strahl wird in einem absorbierenden Material komplett gestoppt, das an ein transparentes Medium (Plexiglas) als 'Fenster' für die Diagnostik gekoppelt ist. Schockgeschwindigkeiten wurden detailliert mit einer Schlierendiagnostik vermessen, mit der zum ersten Mal auch multiple und reflektierte Druckwellen beobachtet werden konnten. Die gemessenen Geschwindigkeiten in Plexiglas erreichen Werte von bis zu 3.5 km/s und liegen somit deutlich über der Schallgeschwindigkeit des Materials (2.6 km/s). Die experimentellen Daten wurden mit Rechnungen eines zweidimensionalen hydrodynamischen Codes (BIG-2) verglichen, die eine gute Übereinstimmung ergaben. Während der Kompression steigt die Temperatur nur um circa 4 K. In weiteren Experimenten mit anderen Targetkonfigurationen und Ionenstrahlen wurden quantitative Messungen mit einem Interferometer durchgeführt. Der Druck wurde direkt durch geeichte piezoelektrische Sonden bestimmt. Die interferometrischen Messungen wurden mit Ergebnissen von einer weiteren Diagnostik verglichen, die Gradienten des Brechungsindex direkt durch die Ablenkung eines Laserstrahls bestimmt. Auch diese beiden Messmethoden zeigten eine sehr gute Übereinstimmung. Wichtige Informationen über die hydrodynamische Expansion des geheizten Materials konnte durch orts- und zeitaufgelöste Schattenfotographie gewonnen werden. Expansionsgeschwindigkeiten von einigen hundert m/s wurden gemessen. Neben metallischen Targets wurden auch kryogene Edelgaskristalle sowohl durch Schattenfotographie als auch durch zeitaufgelöste Spektroskopie im sichtbaren und im VUV-Spektralbereich untersucht.

Die hier beschriebenen Experimente liefern eine Vielzahl an Details über Materie, die durch multiple Schockwellen komprimiert wurde. Die Daten bilden eine solide Basis für das Verständnis der kalten Kompression mit Schwerionenstrahlen. Sie dienen ausserdem zum Testen von Simulations-Codes und von Zustandsgleichungstabellen (EOS). Die Entwicklung neuer Diagnostiken wird durch diese Daten unterstützt und Experimente zur Kompression von Materie bei höheren Stahlintensitäten und Energiedepositionen in zukünftigen Schwerionenstrahlen können leichter vorbereitet werden.

Abstract

High energy density in matter is of fundamental interest for various fields of science, including plasma physics, astrophysics, geophysics and applications such as possible future energy sources based on inertial confinement fusion. Intense, relativistic heavy ion beams are ideally suited to produce high energy density in matter.

The heavy ion synchrotron SIS-18 at the Gesellschaft für Schwerionenforschung (GSI) can supply intense ion beam bunches, of about 5×10^9 particles for U^{92+}, delivered in 550 ns long pulses. This leads to a specific energy deposition of about 1 kJ/g in solid matter which creates solid density plasmas at relatively low temperatures ($\sim$1 eV). The ion beam driven pressures of up to 100 kbar generate weak shock waves that compress solid matter to a density ratio of up to 1.1. The main subject of the work presented in this thesis is an experimental study of heavy ion generated shock waves in solid targets and investigations of the properties of the compressed material. In these experiments a multi-layered target was used, consisting of a solid metal (Al, Cu, Fe or Pb) followed by a transparent material (plexiglass) and a confiner plate made of Al. The thickness of the metal layer was chosen such that the entire beam was stopped in this layer and high pressure was generated in the beam deposition region. This high pressure launched a shock wave that travelled into the plexiglass layer which, due to its transparency, served as a diagnostic window. A number of different diagnostic methods were developed to measure the stress induced by the heavy ions in targets, used to achieve cold compression. During an experiment with a Kr ion beam, shock velocities were measured for the first time by one- and two-dimensional schlieren techniques, which allow a good visualization of the multiple- and reflected shock waves. For pressures of up to 15 kbar, shock velocities in plexiglass of about 3.5 km/s were determined, a value which is above the sound velocity of this material (2.6 km/s). The parameters measured for different metallic absorbents, i.e. Cu, Fe and Pb were in good agreement with theoretical values given by a 2D hydro-code. An increase of temperature in the plexiglass of only 4 K during the compression process was found. The same type of solid target in combination with other ion beams (U or Au) were investigated by imaging interferometric techniques and the pressures were directly measured by using calibrated piezo-electric gauges. The data resulting from the interferometric and the laser deflection determinations of refractive index gradients were compared and they showed a good agreement. Useful informations about the hydrodynamical expansion of the heated matter were obtained by backlighting shadowgraphic recordings, performed time- and space resolved. Velocities of several hundreds of m/s were determined. Besides metallic targets, rare-gas cryogenic crystals were also studied, both by shadowgraphy and time-resolved spectroscopy in visible and vacuum-ultraviolet (VUV) regions.

The experiments described hereby provide details about the material compressed by multiple-weak shock waves and can be useful in understanding the cold compression of matter scheme, in the heavy-ion beam driver approach. They also constitute a benchmark tool for simulation codes and equation-of-state (EOS) tables. Based on these observations, a further development of experimental methods can be achieved to investigate the compression of matter with higher intensities and deposition power delivered by future heavy ion beams.

Contents

Chapter 1

Introduction

Plasma is the most dominant form of matter throughout the known universe, providing extreme examples of high-energy density related phenomena. One of the most outstanding problems, the energy production in stars, triggered the quest for a future energy source about 50 years ago. Since its inception, the research in the direction of obtaining controlled thermonuclear fusion on Earth has contributed enormously to plasma physics development, both experimentally and theoretically. Different approaches came into view, splitting the fusion research in two branches: the magnetic confinement fusion (MCF) and the inertial confinement fusion (ICF). The principle of MCF is based on a magnetic field $\vec{B}$ confining across its directions charged particles, which move readily parallel to the magnetic field. Therefore the magnetic lines are bent around to close onto themselves, resulting in a toroidal system. However, a simple toroidal $\vec{B}$ field is not sufficient to balance the forces for plasma equilibrium, and a suitable poloidal component encircling the torus the short way is required as well. The plasma is created at high temperatures (> 10 keV), low densities (10^{14} cm $^{-3}$) and a long time to fulfill the Lawson criterion [Law67]:

$$n\tau = 10^{20} \quad s/m^3, \tag{1.1}$$

where n is the number of particles and τ is the energy confinement time. The stable magnetic configurations on which the current research concentrates are the tokamak [Pin89, Wes96] and the stellarator [Gri93]. In the former the poloidal magnetic field is provided by toroidal electric currents flowing in the plasma and external coils. The stellarators do not need externally driven plasma currents. The poloidal field is generated by the twisted magnetic geometry, in a configuration designed and optimized by 3D equilibrium and stability computations.

A challenging approach is the ICF scheme [Hog92], which proposes the compression of a capsule containing D-T fuel up to 1000 times solid state density in order to ignite fusion at the central region- the so-called hot spot. The hot, dense plasma expands and cools on an inertial time scale (the time determined by the inertia of the fuel mass). While the heated outer material must absorb an extreme power flux without preheating the central spot, the latter has to follow a cool adiabat to minimize the amount of compression energy required. A spherical symmetry has to be maintained to diminish conditions favoring the Rayleigh-Taylor instabilities. Therefore the 'indirect-drive scenario' has been conceived, which consists in the use of a high-Z material to convert the irradiating power from an array of high-peak-power lasers or from high-intensity ion beams into thermal x-rays. From the ion beams a power density of 10^4 TW/g or more inside the converter is required. Parameters needed to achieve a high energy gain in D-T targets are discussed

in detail, among other works, in [Bas92]. Although the aforementioned value is beyond the capabilities of the present accelerators, a great technological breakthrough in the possibilities of upgrading the ion beam intensities, energies and pulse length, as well as the superior advantage of high repetition rate, reliability and efficiency [Ban99] encouraged the ICF research also with ion beams.

During the intense studies of ion beam created plasmas, many physical issues regarding the behavior of matter in such special conditions emerged. A matter of interest is the collection of properties of strongly-coupled plasmas, which are characterized by a Coulomb-coupling parameter (ratio between the potential energy and the kinetic energy) [Ebe91, Ich82] $\Gamma \gg 1$. Such state of matter is prevalent for example in the cores of giant planets in our solar system and of newly discovered extra-solar planets, numbered to 61 so far. These planets are very likely Jupiter type of objects [Red01], called 'hot-Jupiters' due to the small distance to their sun. The interior of Jupiter and Saturn is exposed to pressures of 50 Mbar and temperatures of some thousand Kelvin, circumstances which lead to transitions of hydrogen, which is the preponderant element in the core, to a metallic state. The idea of creating metallic hydrogen rose [Wig35] and many theoretical studies showed that there are other advantages which can find industrial applications as well. Besides being the lightest known metal, its superconductive property at room temperature was predicted [Ash68].

Measurements of electric conductivity have shown that hydrogen undergoes a transition from a semiconducting to a diatomic metallic fluid with an electric conductivity of about 2000 $(\Omega cm)^{-1}$ [Wei96], at a pressure of 1.4 Mbar and 3000 K. The underlying idea is that fluids metallize when the mean free path of thermally excited electrons becomes comparable to the mean distance between the particles providing the electrons. In the case of solids, the transition from insulator to metal occurs if the distance between the particles in the grid becomes comparable to the dimension of the wave function so that the electrons delocalize. In these situations, the critical value of metallic conductivity given by the Mott criterion:

$$n_c^{1/3} a_B \sim 0.25, \tag{1.2}$$

where a_B is the effective Bohr radius, is surpassed. It is assumed, although not yet completely elucidated, that the molecules at these pressures dissociate. Computer simulations showed strong fluctuations of charge density, meaning that the particles, after a few oscillation periods, look for new binding partners [Due00].

The compression can be achieved by static methods, such as the compression of a diamond anvil cell press [Mao94], but they are limited to pressures of some hundred GPa. More attractive from the density and temperature point of view are the dynamic methods which rely on a fast energy release and lead to high-energy densities for short times. In most of the cases the compression is done by shock waves created in solids. There are numerous methods to create shock waves, from chemical explosives [McQ70], nuclear detonations [Mit91], electromagnetic guns [Haw81] to high power lasers [Loe94, DaS97], light ion beams [Bau96] and heavy ion beams [Tah01]. The determination of the propagation velocity of the shocks and the velocity of the matter after compression enables thus the equation-of-state (EOS) analysis of the matter at high compression, which are of great importance in both ICF and phase transition physics. The states which can be reached by shock waves are displayed in the diagrams of the Hugoniot curves, covering a wide range of parameters for single shock waves or multiple shock waves.

With heavy ion beams a quasi-isochorical heating of solid matter can be achieved. The uniformity of bulk heating and the high repetition rates which allow repeated and

reproducible measurements constitute undoubting advantages. Multiple shock waves can be generated and thus the density ratio can be enhanced at lower compression pressures than in the case of single shocks. The drawback of heavy ion application in shock compression is the present insufficient intensity of the beams and the duration of the pulses to reach the ranges in which both ICF and H-metallization can be obtained. However, the situation improves at a fast rate by successive upgrades of the accelerator performance so that intensity of the beams, as well as their pulse lengths can be optimized.

At the Gesellschaft für Schwerionenforschung (GSI) in Darmstadt, the construction of a larger synchrotron ring than the present one, leading to a magnification of the beam intensity by a factor of 1000 (up to 2×10^{12} particles per pulse for uranium ions), is under discussion [Gsi01]. This would lead to specific deposition powers of 10 TW/g, enabling studies of unexplored regimes of hot, very dense plasmas. There are also technological means (as described briefly in Chapter 3, 'GSI accelerator facility' section) for reducing the ion beam pulse length to 50 ns, which will bring about a high gain in the power deposition [Tah01b].

This work is part of the long-term project 'High-energy density in matter' of the Plasma Physics Group, which proposes several investigation points, among which is the EOS study of condensed matter in high compression conditions. This is correlated to the future investigation of the phase transition of solid hydrogen from an insulator- to a metallic state in the ion beam approach. Studies on the ion beam interaction with solid targets made of lead [Sto98] and cryogenic gas crystals [Fun99, Dor96] provided an insight into the physics of the process and characterization of the matter response. These works comprised measurements of pressures, velocities of heated matter expansion and beam energy conversion into radiation. They also optimized or developed diagnostic tools and target materials and an entire experience useful for the following measurements. The purpose of this work is to characterize the shock waves induced by heavy ion beams in solid matter and to evaluate the actual potential of a cold, indirect compression scheme by using heavy ion beams at the parameters given by the present accelerator machine. Several experimental techniques were applied for investigations during experiments employing different ion beams and target configurations. The results are presented and discussed in the following chapters.

Chapter 1 refers to some of the main specific effects of the ion beam in interaction with solid matter. An incursion in the fundamentals of the shock wave physics applied in the particular case of heavy ions as driver closes this theoretical part.

An overview of the experimental environment follows, with some technical details about the GSI accelerator facility, the high-temperature experimental area (HHT) and the conditions in which the measurements were performed, including the beam diagnostics.The last section of this chapter is dedicated to the crystal growing technique and the description of the cryo-device, since cryogenic crystals represent one type of targets used in the experiments.

Chapter 3 describes the experimental results obtained by applying different imaging and optical techniques such as backlighting shadowgraphy, schlieren, interferometry and laser deflection. After the section 4.2 about the schlieren measurements, a description of a 2D- hydrodynamic code which simulated the measurements, together with the outcome of the simulation, are presented. The pressures induced by the beams in the solid targets were measured using polyvinylidene fluoride (PVDF) pressure gauges and the interpretation of the electrical signals is given in the section 4.8 of this chapter. Spectroscopic investigations were performed together with other measurements for gathering

more information about the interaction of the ion beam with cryogenic crystals, a target of major interest for the future experiments. The determination of important parameters such as the temperature of the plasma created inside the crystal by the ion beam was not accomplished. However, there are new, interesting issues which have to be taken into consideration and therefore they were qualitatively discussed in the end of the chapter.

The work ends with an outlook which contains a concluding summary resulting from comparisons and analysis of all measured data and a revision of advantages and disadvantages of the scheme approached in the described experiments. There are also few comments about possible future optimizations, from the experimental point of view.

Chapter 2

Fundamentals of heavy ion beam interaction with matter

2.1 Specific energy deposition and stopping power in solid matter

Generation of hot, dense plasmas by heavy-ion beam heating of solid matter is a complex, dynamical process resulting from a fast energy deposition. A characterization of the matter state evolution can be obtained by building an equation-of-state (EOS) which relates the change of the internal energy of the matter to the other quantities defining a specific state, at a certain time. The EOS together with other theoretical and experimental considerations contribute to the modelling and understanding of the heating process in the particular case of heavy ion beams in interaction with solid matter. A simple illustration from the temperature point of view of the situation that takes place during the irradiation of the target is given in figure 2.1. As the ions penetrate into the target, a large number of

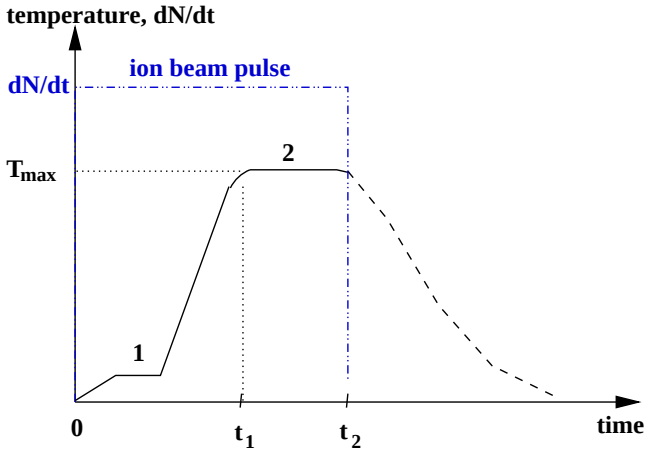

Figure 2.1: Temperature evolution in a target during the heating by a rectangular heavy ion beam pulse. The maximum temperature is reached at the time t_1, when cooling effects start. The time t_2 represents the end of the beam pulse. The plateau (1) is caused by losses of energy spent for overcoming the binding energy between the target atoms [Jac02]. The second plateau (2) appears due to the cooling losses, especially the hydrodynamic expansion of the heated matter.

Coulomb collisions with the target electrons occurs, leading to energy losses and finally, at the end of the range, to the stopping of the ions. In this way a large fraction of the kinetic energy of the projectiles is converted into internal energy of the target, after a given thermalization time. The key parameter for the matter heating caused by the energy loss is the specific deposition power P, i.e. the beam energy deposited per unit time and unit target mass. During the first phases of the heating (in figure 2.1, between 0 and t_1), as the temperature increases and there are no important loss processes occurring, the specific internal energy ϵ of the target increases roughly linearly in time, for a flat-top beam temporal profile (uniform particle distribution):

$$\epsilon \cong \int_0^{t_1} P(t)dt = P \cdot t_1. \tag{2.1}$$

The pressure increase will cause then the hydrodynamic motion of the heated volume with kinetic energy provided from conversion of the internal energy. The temperature rise slows and eventually stops when the plateau between t_1 and t_2 is reached, at T_{max}. The temperature saturation would be reached in any case, also due to other losses such as the electron heat conduction and thermal radiation, which become active as the temperature rise. Dominant in solid heating by heavy ion beam is the hydrodynamical motion. After the density of the material decreases due to the expansion of the heated matter, the cooling mechanisms become more and more important and thus the temperature drops, even though the heating continues. The highest energy density corresponding to the highest pressure is reached therefore around the time t_1. The specific internal energy, ϵ, during this entire process, follows the differential equation of energy balance, which is:

$$\frac{\partial \epsilon}{\partial t} = P_s - p\frac{\partial V}{\partial t} - \frac{\partial S_{el}}{\partial m} - \frac{\partial S_{rad}}{\partial m}. \tag{2.2}$$

In the right-hand side of the equation the first term represents the specific deposition power of the beam; $V = \rho^{-1}$ is the specific volume; ρ the mass density; $S_{el,rad}$ are the energy fluxes of electronic heat conduction and of thermal radiation, respectively; $\partial m = \rho \partial z$ is the mass increment of the Lagrangian mass coordinate. The second term expresses the most dominant loss term in the heating process by heavy ion beams, which is the hydrodynamic work. It is followed by the electronic heat conduction and thermal radiation cooling terms.

- ***Hydrodynamic cooling.*** During the bulk heating of the matter, the power dissipated through hydrodynamic work dominates the losses when the density in the target is sufficiently high ($\sim 10^{20}$ g/cm^3) and the temperature low (T < 10 eV), as the case of targets irradiated by SIS beams at GSI. This term scales with ρc_T^3, where c_T is the thermal sound speed, which is well approximated by:

  $$c_T \cong \epsilon^{1/2} = (P \cdot t)^{1/2} \tag{2.3}$$

  In the case of an isochoric heating this term has no contribution to losses and the entire deposited specific energy is converted into internal energy serving the increase of temperature. This process occurs during a characteristic heating time t_H (t_1 in figure 2.1) which in [Arn88] is calculated for a cylindrical target with a radius r_0 as:

  $$t_H = \left(\frac{9r_0^2}{4P}\right)^{1/3} \tag{2.4}$$

If $t_H > t_b$, where t_b is the ion beam pulse duration, the effects of the matter expansion over the temperature are considerably diminished. It was proved by recent experiments [Var01] that the situation is not completely in favor of a fully efficient heating of the target. In consequence, very short beam pulses are required to increase the specific deposition power and to prevent large losses due to the hydrodynamical motion of the heated matter.

- ***Radiative cooling.*** The radiative cooling governs the losses at lower target densities or higher temperatures. The electromagnetic radiation is emitted by the entire volume if the target is optically thin ($\tau \ll 1$) or from the surface layers in the optically thick case. The limiting temperature scales with the beam power as $T \sim P^{\alpha}$, where α can reach a maximum value of 2 in extreme cases, for optically thin plasmas with Bremsstrahlung only [Arn88]. In the optical thick case, the radiation loss depends strongly on the temperature and the product of density and radius (width) of the target. It was empirically estimated that a fraction of 1/1000 of the deposited energy is emitted in the visible range [Dor96], while in the VUV range a much higher conversion ratio ($> 20\%$) has been observed [Fun99]. The time resolved spectroscopic measurements described in the Chapter 4 of this work, performed using cryogenic crystals, show recordings in the VUV range of a sufficiently intense radiation emitted during the entire pulse length of the beam. Although accurate quantitative measurements are not done, the experimental data lead to the conclusion that the radiative cooling cannot be neglected. Further spectroscopic measurements will establish values for the conversion ratios in visible, VUV and possible X-ray ranges.

- ***Heat conduction cooling.*** The general heat conduction equation:

$$\frac{\partial T}{\partial t} = \frac{\kappa}{\rho \cdot c} \cdot \Delta T \tag{2.5}$$

shows that this loss term in the heating process becomes important in the presence of large temperature gradients. Here κ is the heat conductivity coefficient, ρ the mass density, T the temperature and c the heat capacity of the matter. While the dependence on the temperature is strong, there is no correlation to the density, a fact which can be noticed in the electronic heat flux equation:

$$S_{el} \cong 10W/(cm^2 \cdot (eV)^{7/2}/cm) \cdot T^{5/2} \nabla T. \tag{2.6}$$

The heat conduction cooling is a significant process mainly in the situations when the hydrodynamic and radiative losses decrease. It plays a major role in the laser-produced plasmas where, contrary to the ion-beam heated plasmas, large temperature gradients are generated. In the case of ion beam plasmas the temperatures usually do not exceed 10 eV. Due to the quasi-uniform energy deposition up to the Bragg peak, the gradients are not as sharp as in the laser heating process.

Initially, P_s is balanced by $\partial\epsilon/\partial t$, while in the plateau region it is balanced by one of the cooling terms, namely the most rapid and dominant one. At this point, the specific deposition power and the hydrodynamic term are coupled together. The local deposition power depends on the energy loss along the ion range in the target which is determined by the density distribution along the ion path. When the hydrodynamic motion begins,

the density distribution changes drastically with it. It should be mentioned that the rate of the density change is given by the local speed of sound c_s, which is a function of the temperature and therefore of the specific internal energy ϵ. In other words, the change of ion range inside the target due to a density variation during the heating time changes the distribution of the specific deposition power and all the quantities of state which depend on it. Higher temperatures can be attained by an increase in the specific deposition power, which therefore becomes a key parameter in the heating process:

$$P_s = \frac{d\Phi_b}{dR} = j_b \frac{dE_s}{dR} = \frac{1}{\rho}\frac{dE_s}{dz} \cdot \frac{1}{A} \cdot \frac{dN}{dt}, \tag{2.7}$$

with $\Phi_b = j_b E_s$ the beam intensity, j_b the current density of the beam particles, E_s the energy deposited by a particle, A area of the beam cross section, N the number of particles and $dR = \rho dz$ the range increment. The energy loss dE_s/dz term depends further on the ion species of the beam, the target atomic composition and the state of the target. The equation shows that a high specific deposition power can be achieved by an increased energy loss, a large number of particles and a small focal spot of the beam in the target.

- ***Focusing of the beam.*** The last condition mentioned above for achieving higher deposition power is fulfilled by using a plasma lens device for a strong focusing of the beam (details about plasma lens in section 3.3 of Chapter 3). Flexible adjustments of the lens allow for the target to be located in the focal plane. The device works as an ideal optical lens [Bog91] for a parallel incident beam, which means that the width $r_{f_{x,y}}$ of the current beam density $I_{x,y} = (1/A) \cdot dN/dt$ in the focal plane depends on the focusing angle and on the beam emittance. The focusing angle can be calculated using:

$$\alpha_{x,y} = \frac{\epsilon_{x,y}}{r_{x,y}} \tag{2.8}$$

  where x, y are the coordinate axis in the plane transverse to the beam axis and $\epsilon_{x,y}$ the emittances of the beam in the horizontal and vertical directions, representing a measure of the effective area of the particle distribution in the phase space. Due to the azimuthal symmetry of the lens focusing properties α_x is equal to α_y, while ϵ_x might differ from ϵ_y. Therefore the beam cross section is generally an ellipse with an area A and half axis $2r_x$ and $2r_y$ in the x-y plane, as functions of coordinate z along the beam axis. The variations of $r_{x,y}$ with z are important for an error-free calculation of the specific energy deposition by using 2.7. In fact the beam is not sharply defined as $r_{x,y}$ would suggest, but it rather has a Gaussian profile in the transverse direction, with the standard deviations σ_x and σ_y. The effective area is then described by the root-mean square emittance ϵ_{RMS}, comprising around 86% of the whole particles in the beam [Sto98, Fun99]. The transversal beam size as a function of position along the beam axis is:

$$\sigma_i(z) = \sqrt{\sigma_{i,e}^2 + 2 \cdot \sigma_{i,e} \cdot \frac{d\sigma_{i,e}}{dz} \cdot (z - z_e) + \left(\frac{\epsilon_i^2}{16\sigma_{i,e}^2} + \left(\frac{d\sigma_{i,e}}{dz} \right)^2 \right) \cdot (z - z_e)^2} \tag{2.9}$$

  In this equation, i = x,y, $r_{x,y}$ were replaced by $\sigma_{x,y} = 2r_{x,y}$, and the quantities with the index 'e' represent the parameters at the exit of the plasma lens. The relation can be obtained from derivation of a differential equation describing the beam envelope drift in a field-free space. Inside a solid target, the transverse beam

size may be affected by straggling effects, which eventually should be taken into account.

The solid heating by heavy ion beams is, in most of the experiments, performed in cold matter and thus the heating power scales with the cold ranges. All of the experiments described in this work used the TRIM code (TRansport of Ions in Matter) [Zie96] in order to calculate the stopping ranges. In heated material the stopping power tends to increase particularly at the end of the range, forming regions of much higher temperature due to sharp Bragg peaks. The fast ion stopping was profoundly studied [Ahl80, Pet91]. In cold matter it is caused mainly by multiple Coulomb collisions with the bound target electrons and it can be calculated by using the Bethe-Bloch formula [Arn88]:

$$-\frac{dE_s}{dz} = \frac{4\pi e^4 Z_{eff}^2}{m_e v_p^2} \cdot N_t \cdot L_{bound}, \tag{2.10}$$

with the stopping number per target atom

$$L_{bound} = Z_t ln[(2m_e c^2 \beta^2 \gamma^2 / I) - \beta^2] \tag{2.11}$$

where N_t is the ion number density of the target matter, $\beta = v_p/c$, v_p the particle velocity, I the average ionization potential, Z_{eff} the average charge state in the target and $\gamma = 1/\sqrt{1-\beta^2}$. For the relativistic case ($E \geq 10 AMeV$), the formula contains a term that adds corrections due to density effects and shell corrections which must be considered.

In the case of completely ionized and dilute (weakly coupled) matter, where the collision are due also to the free-electron Coulomb collisions, the stopping number is:

$$L_{plasma} = G\left(\frac{v_p}{v_{th}}\right) \cdot Z_t[ln(2m_e c^2 \beta^2 \gamma^2 / \hbar\omega_p) - \beta^2 \tag{2.12}$$

where $G\left(\frac{v_p}{v_{th}}\right)$ is the plasma function which depends on the ratio between projectile velocity v_p and thermal electron velocity v_{th}, Z_t becomes the number of plasma electrons per target ion and $\hbar\omega_p$ is the plasmon energy.

Beside electron collisions, there are possible effects in the energy loss also caused by nuclear collisions, but usually they do not play a significant role in the heating with fast ions. They become comparable with the electronic collisions only for an energy range from 10 to 100 AGeV, producing energetic particles ejected in the forward direction and with energies which usually will not be thermalized.

2.2 Thermalization effects

As mentioned at the end of the previous section, the main mechanisms in the thermalization process are the collisions between beam ions and electrons in the target material. The energy transferred by the ions is described by:

$$E = \frac{p^2}{2m_e} = \frac{1}{2m_e}\left(\frac{2Ze^2}{v_p}\right)^2 \cdot \frac{1}{b^2} \tag{2.13}$$

where $p = \frac{2Ze^2}{v_p b}$ is the momentum transferred to a free electron at a distance b from the straight projectile trajectory, v_p the projectile velocity, m_e the electron mass and Z the charge of the projectile. The energy transferred to a target ion of mass m_i is negligible, since it is smaller by $\frac{m_e}{m_i} \ll 1$. The number of electrons per unit length with a transferred energy E in the interval dE is:

$$dN = n_e \cdot 2\pi b db = 2\pi (Ze^2)^2 \frac{n_e}{m_e v_p^2} \cdot \frac{dE}{E^2} \tag{2.14}$$

Integrating the above equation over all energies, $dE/dz = \int E dN(E)$ the stopping power formula in its non-relativistic limit is obtained.

The assumption of an energy deposition thermalized locally and instantaneously can be checked by estimating the electron mean free path and energy relaxation time. The electron mean free path for electron-electron collision is:

$$l_{ee} = \frac{1}{n_e \sigma}, \tag{2.15}$$

with $\sigma \gtrsim \pi(\frac{e^2}{E})^2$ the Coulomb cross section of an electron-electron collision, for an energy E of the projectile electron. The electron-electron collision time is then given by

$$\tau_{ee} = \frac{l_{ee}}{v_{ee}} \tag{2.16}$$

and the electron-ion relaxation time is:

$$\tau_{ie} = \left(\frac{m_i}{m_e}\right) \tau_{ee}. \tag{2.17}$$

A simple calculation for a beam energy of 300 AMeV leads to an electron energy of approximately 700 eV and a relaxation time in the nanosecond range. Related to the beam pulse, usually some hundred of ns, the thermalization can be considered as an instantaneous process.

2.3 Spatial distribution of deposited energy

One of the main quantities for the ion beam heating in solid targets is the energy loss and therefore many experimental studies were performed within the Plasma Physics Group at GSI [Hof90, Jac90, Gol98]. The work comprised investigations of energy loss at ion beam energies of at most 6 AMeV in externally created plasmas, such as discharges [Wet96] or laser ablation plasmas [Rot97]. Only recently a series of time resolved energy loss measurements were performed at the High Temperature experimental area (HHT) employing high intensity beams from the synchrotron ring (SIS) of energies of 190 AMeV and 300 AMeV [Var01]. Novel in these investigations was, besides the technique and the dynamical method used, the outcome which showed a continuous change in the energy loss of the ion beam due to the hydrodynamic motion of the heated material and therefore to the change in the density distribution along the target, sufficiently high to reconsider the assumption of an isochoric heating of the ion beam.

For energies above 10 AMeV the energy loss is described with good precision by the relativistic Bethe-Bloch formula (equation 2.10). Since it increases with decreasing projectile velocity, the energy loss rises as the ions penetrate deeper into the target. In the Bragg peak the highest energy deposition is reached just before the beam is completely stopped. In this energy range, changes of the charge state play an important role. The energy loss can be calculated from an effective, average charge state Z_{eff}, which follows from semi-empirical approximations. Such an example is the energy loss table from [Zie96] used in the computer program TRIM. All the energy loss calculations for the experiments presented in this work were carried out using it.

For an accurate calculation of the energy loss inside the target the resulting spatial distribution of the beam caused by several effects have to be considered. Together with the momentum spread dp/p, which for the SIS beams is 0.2% [Spi94] and the angles under which the ions enter the target, the straggling effects have to be estimated and eventually taken into account.

The small-angle Coulomb collisions with target electrons produce statistical fluctuations in the energy loss and direction of the projectiles during the stopping process. A mathematical description of the mean-square angular spread in projectile trajectories after a path length z in a homogeneous target medium is given by [Seg65]:

$$< \Phi^2 >= z \cdot (m_e/m_p) \cdot (Z_t/E_p) \cdot (-dE_s/dz) \tag{2.18}$$

where m_e is the electron mass, m_p the projectile mass, Z_t the nuclear charge of the target material, E_p the projectile energy and (dE_s/dz) the average value of the stopping power. The angular spread is given in radians^2. As an effect of the angle straggling the transverse beam intensity distribution is affected and depends on the range in the target. For sufficiently thick targets, a large scattering angle distribution is unlikely and a Gaussian distribution can be assumed. Other analytical forms of angular spread calculations can be found in [Lyn91].

During the slowing down process of the beam, a statistical spread in the energy for a given charge state of the projectile will occur, with $< E^2 >\neq E_0$ where E_0 is the most probable energy. The broadening of the Bragg peak due to a distribution of the ion stopping range is also attributed to this effect. For heavy ions ($M \geq 100$) the energy straggling is relatively small. The relative energy fluctuations in this case are given by

[Seg65]:

$$\Delta E/E \cong \left[\frac{2m_e}{m_p \ln(b_{max}/b_{min})}\right]^{1/2} \tag{2.19}$$

where $b_{min,max}$ are the minimum and, respectively, maximum impact parameters in the Coulomb collisions between the projectiles and the target electrons. These fluctuations are usually not needed to be considered, unless processes at the very end of the range are examined.

A relation between the width of the statistical distribution of the energy loss around the mean value σ_E and the thickness of the target is Gaussian for thick targets and can be calculated by using the Bohr formula [Ahl80]:

$$\sigma_E^2 = \frac{e^4}{4\pi\epsilon_0} Z_p^2 \cdot Z_t \cdot N \cdot d \cdot f(\beta) \tag{2.20}$$

where N is the particle density in the target, d the target thickness, $\beta = v/c$ and f(β) is a function which decreases with velocity. It follows then that the straggling effect increases with the penetration depth.

An example of spatial distribution of deposited energy by ion beams in solid targets is given in figure 2.2.

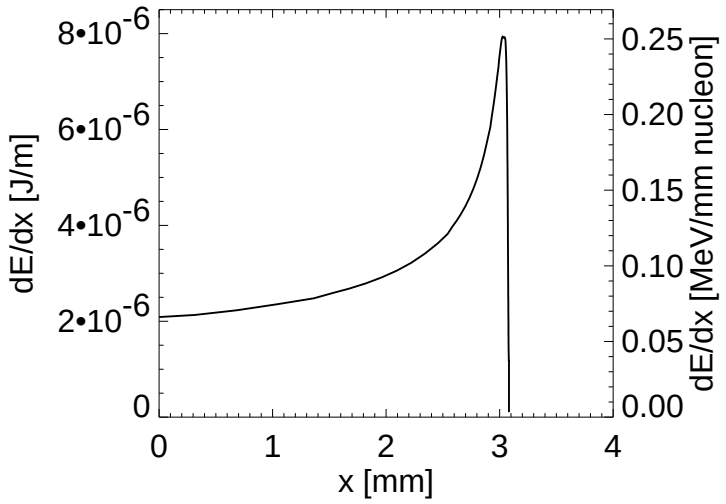

Figure 2.2: Typical curve showing the energy deposited by a Au ion beam with a particle energy of 300 AMeV in a Pb target, as a function of x, where x represents the mean path of an ion along the target length in the beam direction.

2.4 Heavy ion induced shock waves in condensed matter

The present work deals with the compression of solid matter by heavy ion induced shock waves, concentrated mainly on investigations of a specific regime of densities that can be obtained with the present beam parameters, at low temperatures. To bring the probe body to such matter states, a cold compression, implying the separation of the probe from the direct heating of the ion beam, is one solution. The generated shock wave propagates from an absorbent- the material in which the beam is stopped, to the probe where the material compression is then investigated by different experimental techniques. The scheme, as any other experiment with shock wave compression, is very demanding from both experimental and theoretical modeling points of view. A comprehensive understanding of the shock wave behavior and the solid matter response to shock compression is therefore required. The physics of shock waves is presently a vast, complicated science discipline in itself, and only some of the basic principles and equations with closer relevance to the experiments are presented in this section. The entire theoretical description is based on the works of Zel'dovich and Raizer [Zel67], Asay and Shahinpoor [Asa93] and the previous experimental work of Stoewe [Sto98].

Due to loading stresses in matter such as a rapid high increase in pressure, a singularity of particle velocity and pressure as solution of basic equations of hydrodynamics can occur. The propagation of this discontinuity between perturbed and unperturbed matter represents a shock wave. Large compressions, decompressions, shear deformations can accompany a shock wave crossing a solid body; also they cause heating and a rise of the local temperature may occur due to both compression and dissipation. In many cases, depending on the range of impact pressures, a two-wave structure may arise such that the first wave, the so-called elastic precursor, travels with the speed of sound and the second, called a plastic shock wave, travels at a lower speed. An increasing compression can lead to a rise of the propagation velocity of the hydrodynamic disturbance and therefore a steeping of the wave results. The shape of the wave profile, as well as its rise time, depends strongly on the nature and properties of the impact. For example, in the case of the ion beams they depend on the beam pulse duration, which determines the temporal increase of the pressure. For strong shocks the rise time to full amplitude is usually on the order of few nanoseconds or even less, and the sequence of events which follows evolves over a time period of a few microseconds. These events are a result of the shock heating and compression of solids which generally covers a wide range of temperatures and densities. For instance the temperature may reach few eV at compression as high as four times the normal solid density for very strong single shock waves [Tah00]. Compressive stresses of few tens of GPa can be attained, and these values exceed the yield strength of metals, forcing the material into a fluidlike state.

The shock-wave loading of solids can be accomplished by different means: projectile impacts, guns or explosives. Depending on the impact conditions, the resulting shock can differ in strength, which is numerically characterized as the pressure ratio across the shock front, or,often, as the ratio between the shock velocity and the sound velocity. The shock propagation velocity is one of the main parameters which describes the shock. It typically differs by few times from the particle velocity, which refers to the velocity of a given element in the material acquired as a result of the shock wave passing over the element. Both velocities will be used later to define the relations between thermodynamic

quantities specific to the matter on either side of the shock front.

The behavior of condensed matter with respect to a compression is better understood when starting from the atomic level situation. The response of the matter to a compression or decompression is mainly based on the strong interactions between the atoms and molecules through forces with dual character: the attraction exerted between particles separated by sufficiently large distances and the repelling as a result of interpenetration of electronic shells of the atoms when the particles are brought closely together. In the absence of external pressures, equilibrium is reached when attractive and repelling forces mutually compensate, a situation corresponding to a minimum interaction potential energy. To separate atoms by large distances it is necessary to overcome the binding forces by supplying energy equal to the binding energy (which for metals is of several eV/atom). On the contrary case of compression, the energy supplied has to be large enough to overcome the repulsive forces between atoms which increase rapidly with decreasing distance. For reference, few estimations in terms of pressures can be found in Zel'dovich: to compress a metal, for instance by 10%, a pressure of around 10 GPa is required, while for a compression factor of 2, around 100 GPa are needed.

In conditions of such strong compressions of a condensed medium, enormous internal pressures are generated due to the repulsive forces between atoms, a fact which constitute a main property of solids and liquids and which determines the features of the condensed matter response to shock wave compression. Two types of pressures can be distinguished: a thermal pressure caused by the heating of the material by shock waves; this is associated with the thermal motion of atoms and electrons and increases with the strength of the shock. The second is the elastic (or 'cold') pressure which is determined only by the repulsive forces between atoms and it manifests when the thermal energy of the compressed material is not too high, namely in the case of weak shock waves ($P \leq$ 10 GPa). The entire internal energy acquired by the medium from the wave is directed towards overcoming the repulsion due to compression and it is concentrated in the form of potential elastic energy ϵ_c. The small disturbances propagate with a speed which is not temperature dependent, but determined only by the elastic compressibility of the medium (in contrast with gases). Such a situation is met in the compression by heavy ion induced shocks, at present parameters. There is an yield of weak shock waves which are generally characterized by velocities just slightly above the speed of sound, imparting to the material behind the shock front a velocity in the order of a tenth of the wave velocity; the material is compressed by only a few percent (maximum 10%) and pressures do not exceed 10 GPa. The dominant internal pressure generated by the wave compression is the elastic pressure, related to the potential energy by: $p_c = -\frac{d\epsilon_c}{dV}$, which means that the increase in energy is equal to the work compression, and can be regarded as the equation for the isentrope of cold compression. That is because the change of the quantities of state occurs isentropically, just like in the case of acoustical waves (from which they differ little).

Regardless of the aggregate state of the medium, the mass, momentum and energy are conserved across the shock discontinuity and therefore the conservation equation can be generally applied. For mass and momentum the following form can be written:

$$\frac{V_0}{V} = \frac{U}{U-u} \tag{2.21}$$

$$p = \frac{Uu}{V_0} \tag{2.22}$$

with $V_0 = 1/\rho_0$ the initial specific volume, $V = 1/\rho$ the final specific volume, p the pressure in the final state, U the shock velocity and u the particle velocity. Eliminating u, it follows that:

$$p = \frac{U^2}{V_0}\left(1 - \frac{V}{V_0}\right). \tag{2.23}$$

The initial pressure (atmospheric pressure) p_0 was assumed here much smaller than the pressure induced by the wave, therefore $p_0 = 0$. Combining the conservation equations to eliminate velocities, the Rankine-Hugoniot equation results describing the internal energy jump (in front and behind the front) in terms of pressure and specific volume:

$$\epsilon - \epsilon_0 = \frac{1}{2}p(V_0 - V) \tag{2.24}$$

For cold compression, a Hugoniot curve $p_c(V)$ or $\epsilon_c(V)$ can be built and it is this curve that shows all the states which can be reached by the matter behind a compressive shock front. Figure 2.3 shows an example of a Hugoniot curve, calculated for Al by using the SESAME EOS data [Sch01, SES83].

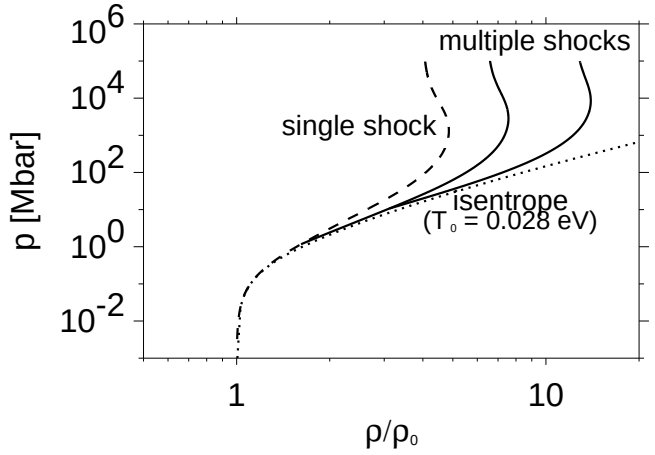

Figure 2.3: Hugoniot curves showing simple (dashed line) and multiple shocks (solid lines) in aluminum, plotted as pressure p versus compression ratio ρ/ρ_0 [Sch01]. For the isentrope (dotted line) the initial temperature T_0 is given.

The above equations are often called 'jump conditions' because the initial values jump to the final values as an idealized shock wave passes by. They are valid only if initial and final states achieved through the shock transition are states of mechanical equilibrium. They are however applied with sufficiently high accuracy also to the unsteady waves for which the state behind the shock front is changing with time, due to either a decompression wave or to certain properties of the medium, such as viscoelasticity or chemical reactions. For the jump condition to be a useful approximation, important is that these changes are slow relative to the rate of change at the shock front.

In order to predict the behavior of a specific material under shock loading, the jump conditions are not sufficient. The equation which relates the pressure to the density, representing also a property of the material itself is the thermodynamic equation of state, which in its more general expression, when it includes time-dependent and non-equilibrium behavior, is called the constitutive equation. For the weak shock wave case Zel'dovich

gives an equation of state used frequently in the isentropic flow region in the following empirical form:

$$p = A(S)\left[\left(\frac{V_0}{V}\right)^n - 1\right] \tag{2.25}$$

where the exponent n is assumed to be constant and the coefficient A depends on the entropy, in fact taken also as a constant. A and n are related by the equation of the speed of sound at standard conditions:

$$c_0^2 = -V_0^2\left(\frac{\partial p}{\partial V}\right) = V_0 \cdot A \cdot n \tag{2.26}$$

According to [She59], for metals n = 4 and A can be calculated from the above equation. The internal energy as a function of V, by using $TdS = d\epsilon + pdV = 0$ can be calculated as:

$$\epsilon(V) - \epsilon_0 = -\int_{V_0}^{V} pdV = AV_0\left\{\frac{1}{n-1}\left[\left(\frac{V_0}{V}\right)^{n-1} - 1\right] - \left[1 - \frac{V}{V_0}\right]\right\} \tag{2.27}$$

The above considerations refer to the case of a plane shock propagating through a condensed medium. In the bulk ion beam heating, target volumes are irradiated quasi-uniformly up to the Bragg peak and this situation resembles much a cylindrical symmetry. The Bragg peak zone is a pointlike source from which spherical weak shock waves in forward direction are generated. Only at large distances r the waves become plane, but the pressure amplitude attenuates as well. The density change can be written as a combination of two functions of distance:

$$\rho = \frac{f_1(r - c_0 t)}{r} + \frac{f_2(r + ct)}{r} \tag{2.28}$$

with c_0 the speed of sound. Another substantial difference from plane shock waves is that for the spherical (or cylindrical) case the condition: $\int pdt = 0$ is fulfilled, since the compression wave is followed by a rarefaction wave.

Aspects regarding behavior of shock waves at interfaces between different materials should be mentioned at this point as well, since they were taken into consideration for the experiments and target design. The targets are composed of layers made of materials with different acoustic impedances ($Z = c_0 \cdot \rho_0$). The absorbents in which the beam is stopped are metals, with higher impedances Z_1 than the following plexiglass sample layer, with Z_2. When a wave transits from a higher to a lower acoustic impedance material, the pressures in the incident and in the reflected waves are not in phase. The reflected wave is a rarefaction wave, while the transmitted one is always a compression wave, with a pressure amplitude (p_t) determined from the incident wave pressure (p_i) by using [Pai76]:

$$\frac{p_t}{p_i} = \frac{2Z_2}{Z_1 + Z_2} \tag{2.29}$$

and, similarly for the reflected wave:

$$\frac{p_r}{p_i} = \frac{Z_2 - Z_1}{Z_1 + Z_2}. \tag{2.30}$$

More details regarding the target design and motivation for the chosen configuration are given in the beginning of the chapter 4, section 4.2.

Chapter 3

Experimental set-up

In this chapter a description of the experimental area is presented, where all the measurements were performed. The first section gives an overview of the GSI accelerator facility, its structure (UNILAC and SIS-18) and current parameters of the heavy ion beams produced by it. Some more technical details about the HHT beamline follow in the second section. The environmental conditions for the experiments are commented in the description about the plasma lens as a fine focusing device, the target chamber at HHT and the beam diagnostics in which useful informations about the ion beams are gathered. The chapter ends with some remarks about the cryogenic system employed for production of crystals, needed in understanding the growing process of the crystals, described hereby as well.

3.1 GSI accelerator facility: UNILAC and SIS-18

By producing beams of ions from protons to uranium ions over a wide range of energies and intensities, the GSI accelerator facility answers to the requirements of many experiments and, implicitly, to the related theoretical studies in various research fields, from accelerator and nuclear physics to biology and medicine. A layout of the GSI accelerator complex is shown in figure 3.1.

The ions are generated by using different ion sources [Wol95], such as Penning, MEVVA (Metal Vapour Vacuum Arc), MUCIS (Multi Cusp Ion Source) and then injected into the approximately 100 m long UNILAC (Universal Linear Accelerator). Its first part had formerly a Wideröe structure, which was replaced in the year 2000 by a high current injector (HSI) for gaining higher beam intensities. A gas stripper placed after the HSI increases the charge state of the ions for further acceleration stages. The desired charge state is selected by a charge state separator. At the same location is the high charge injector (HLI) consisting of an electron-cyclotron resonance source (ECR) and the subsequent RFQ and IH acceleration structure; HLI can be used as an alternative injector mainly for the UNILAC experiments. Energies of up to 11.4 AMeV can be attained further in the Alvarez section, which is followed, in the last part of the linac, by singular accelerator resonators where the beam can be either decelerated or accelerated up to an energy of 20 AMeV.

The beam is injected through a 150 m long transfer channel into the heavy ion synchrotron (SIS) in the high energy area, operating since 1990, where also the experimental storage ring (ESR) is situated. The SIS ring has a circumference of 216 m, a maximum bending power of 18 Tm and contains 24 dipoles at 1.8 T, 12 quadrupole triplets and

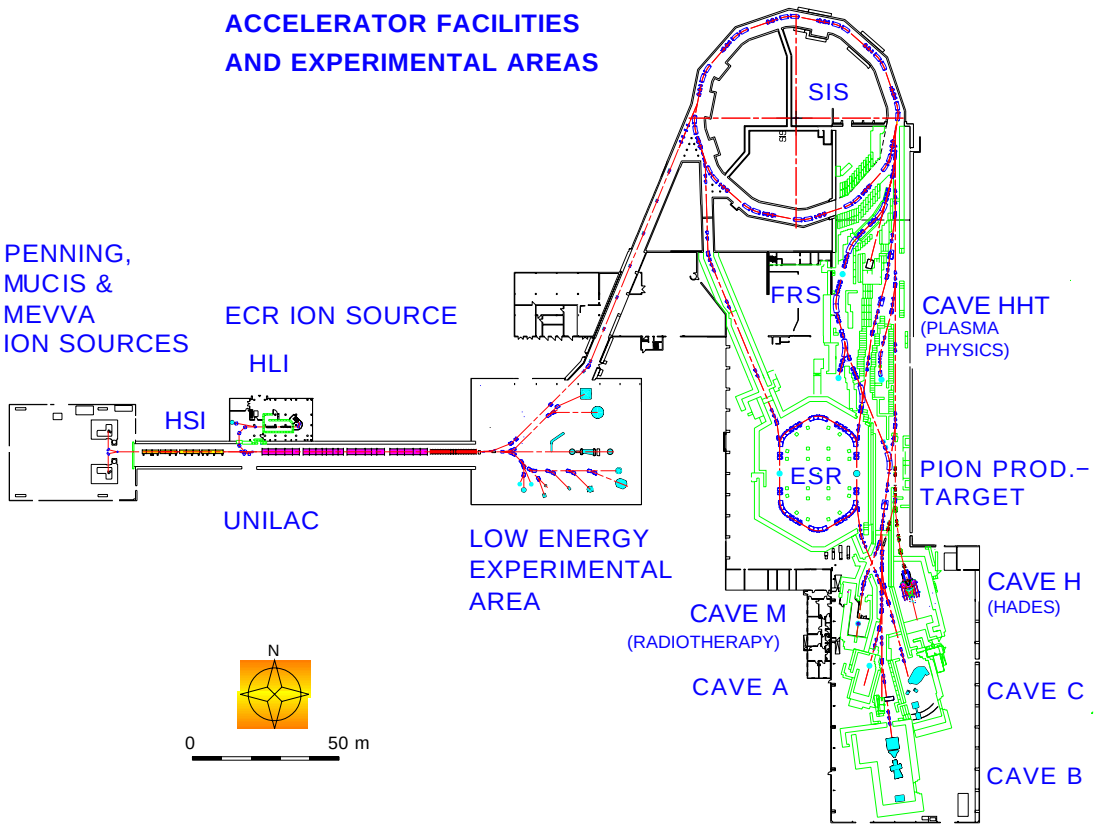

Figure 3.1: An overview of the GSI accelerator facility: the linac (UNILAC) and the heavy ion synchrotron (SIS). Some of the experimental areas are also denoted on the drawing.

12 sextupole lenses for guidance. The acceleration occurs in 2 RF cavities with a peak voltage of 16 kV at a frequency spanning from 0.8 to 5.6 MHz. The beam, reaching maximum particle energies of up to 1 AGeV (for uranium) is then transported through different beamlines in high vacuum conditions (10^{-10} Torr) to several experimental areas.

The plasma physics experiments call for high energy depositions, and efficient energy transfer to the target is vital in order to obtain dense plasma matter. These requirements imply high intensity heavy ion beams to be delivered in short bunches. A great effort within the accelerator physics department was done to improve the beam intensity and to obtain shorter pulses by bunch compression techniques. Solutions like the multiple multiturn injection [Mst99] with transversal electron cooling [Msc99] already led to an intensity increase by a factor of 10 (see figure 3.2) while keeping the beam emittance low. Further optimizations aim to increase the intensity of even the heaviest ions such as uranium up to the space charge limit. Also by an adiabatic bunch compression scheme implying debunching followed by rebunching in the first harmonic single beam bunches of a minimum pulse length of 550 ns are currently obtained without significant particle losses. By a fast bunch compression method the beam will be further optimized in the near future to reach even smaller values (around 50 ns or even less) [Spi99, Lun99].

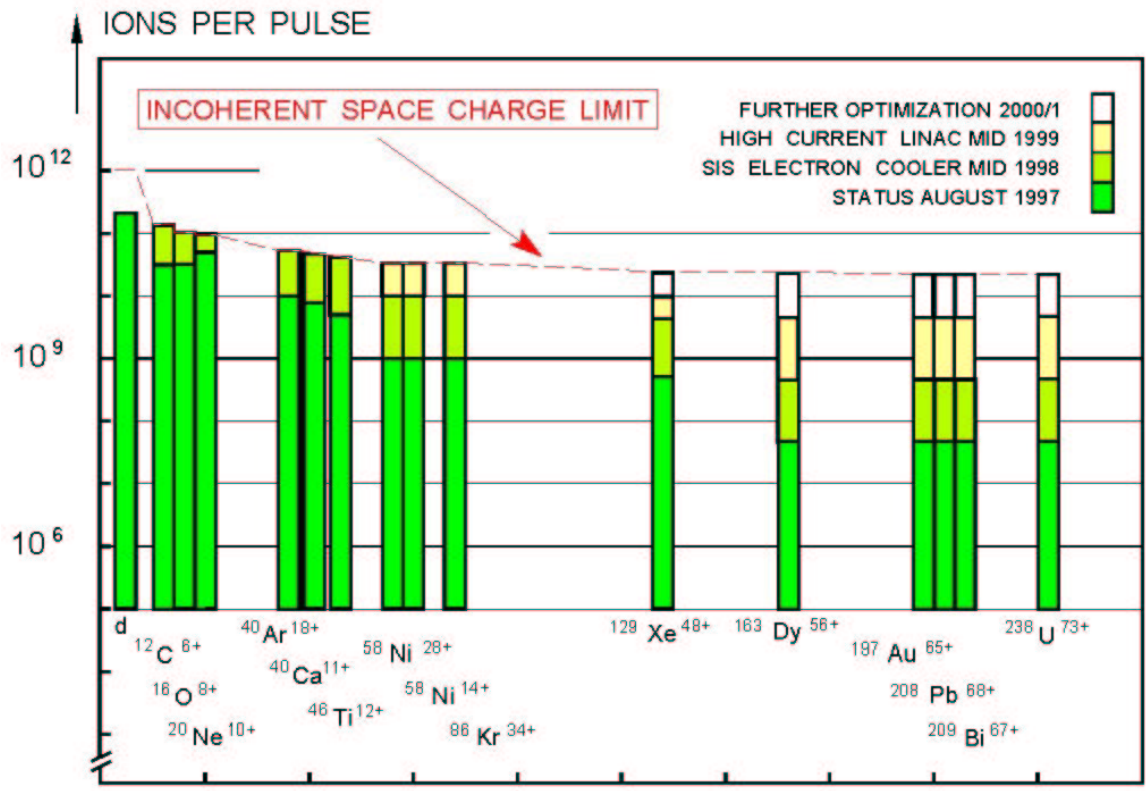

Figure 3.2: Development of heavy ion beam intensities for different ion species in the attempt to reach, even for the heaviest ions, the space charge limit.

3.2 HHT experimental area

In the framework of the research on dense plasmas, the interaction of intense heavy ion beams with matter is investigated at the high-temperature experimental area (HHT). The HHT cave location is marked on the GSI accelerator sketch in figure 3.1. The beam extracted from the SIS ring is transported through a 74 m long transfer line up to the interaction point with the target. From the entrance into the cave (OP) up to the interaction point (IP) the transport line is reserved to HHT only and is schematically shown in figure 3.3.

The HHT beamline consists of two dipole magnets (MS) with bending angles of 7.5° and 15°, two quadrupole duplets (QD) and one quadrupole triplet (QT). The two cur-

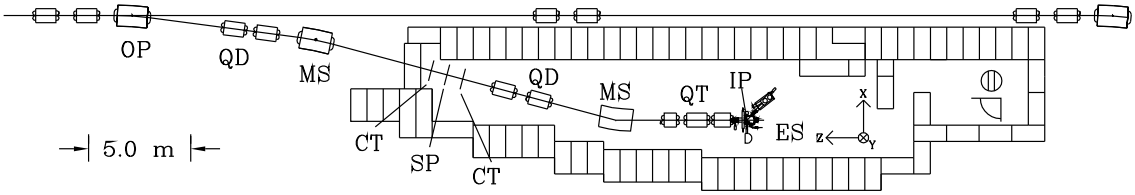

Figure 3.3: HHT beamline structure from the entrance point in the cave (OP) up to the interaction point with the target (IP). Elements used for the beam diagnostics such as two current transformers (CT) and a stripper foil (SP) used for increasing the beam charge state are included in the scheme.

rent transformers (CT) used for beam diagnostics (time profile, beam intensity, beam transmission) and a stripper foil (SP) are also permanent elements of the beamline. The stripper foil, which optionally can be removed from the beamline, is used in the case of a too high magnetic rigidity of the beam delivered by the SIS, which in the HHT beamline cannot exceed the maximum acceptable value of 10 Tm. The magnetic rigidity of the beam can be simply calculated by using the relation:

$$R = \frac{p}{e \cdot Z_p} = \rho \cdot B \tag{3.1}$$

where p is the momentum of the ions, e the elementary charge, Z_p the total charge state and B the magnetic field necessary to bend the beam around the radius ρ.

Formerly, the last dipole together with the last five quadrupoles in the HHT beamline were used as a final focusing system, before the plasma lens went into operation in 1995. Maximum focusing angles achieved in this way were 14 mrad vertically and 52 mrad horizontally [Spi94]. Better focusing angle performances and beam transmission were obtained with the plasma lens and therefore it became a standard focusing device and intrinsic part of the beamline, although not directly connected to it. The last quadrupoles presently serve to achieve parallel beams in both horizontal and vertical directions. For practical reasons concerning the high vacuum required in the beam pipes as well as the electrical insulation of the line from the high current discharges in the plasma lens, the beamline ends 50 centimeters away from the lens with a 20 μm thick kapton foil which does not cause beam losses or scattering. During the lens discharge, the ground potential of the plasma lens can increase relatively to the beamline by several hundred volts and therefore the lens is galvanically decoupled from the line.

3.3 Plasma lens

Foremost for an efficient matter volume heating by heavy ion beams is the transversal dimension of the beam in the plane of the interaction point. Requirements of small focus sizes and minimum particle losses are satisfied by the plasma lens which, after the development period at the University of Erlangen (Germany) and two years of tests at GSI, became a standard final focusing device on the HHT beamline.

A scheme of the plasma lens is presented in figure 3.4.

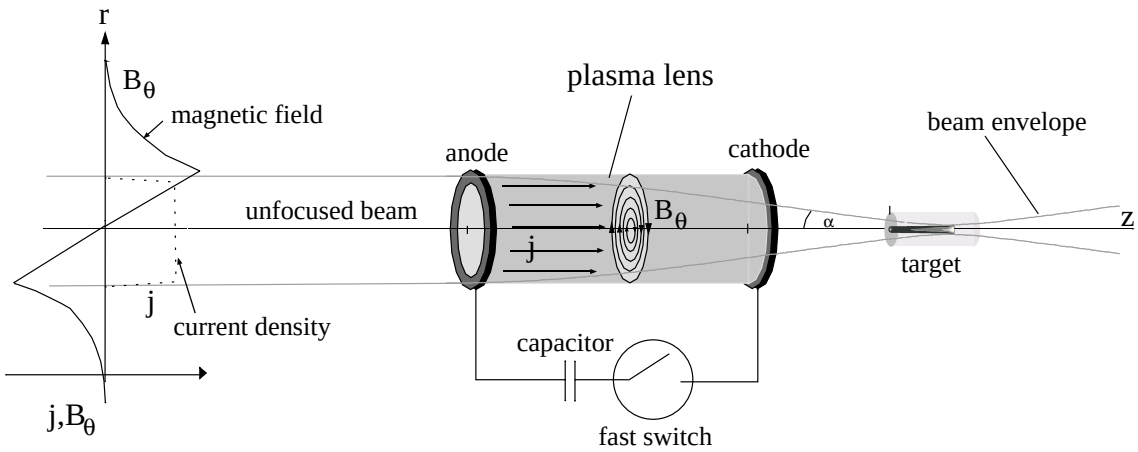

Figure 3.4: Plasma lens discharge tube and an illustration of its focusing working principle.

After leaving the beamline, the ion beam enters the plasma lens through a 20 μm thick kapton window, which is protected by a 50 μm titanium foil from the discharge plasma. At the exit of the lens a conical, 1 mm thick graphite window followed by another 20 μm thick kapton foil separates the discharge tube from the interior of the target chamber. The plasma lens is a z-pinch discharge produced in a 90 mm long Al_2O_3 tube with an inner diameter of 20 mm. The working gas is Ar at pressures between 1-10 mbar. The two hollow electrodes are connected to six pulse generators using pseudo-spark switches [Fra92]. The total energy delivered by the capacitors of the pulse generators is 10 kJ for a charging voltage of 10 kV. In order to improve the reproducibility of the discharge, four electrodes producing surface flashovers are used as a preionization shortly before the main discharge . The discharge is triggered by the pseudospark switches and different Rogowski coils measure the temporal evolution of the current for each pulse generator and for the total current. The total current has a maximum value of about 300 kA for a charging voltage of 12kV and a pulse of a half period of 9 μs.

The focusing principle of the plasma lens is based on the azimuthal magnetic field produced in the z-pinch discharge by the axial current flowing inside the cylindrical tube. If the current density is homogeneous, the magnetic field B inside the plasma increases linearly with the radial distance from the axis r:

$$B(r) = \frac{\mu_0 I r}{2\pi R^2}, \tag{3.2}$$

where μ_0 is the magnetic permeability, I the total discharge current and R the radius of the current density distribution. In this case the lens acts on an entering beam as an ideal ion optical lens [Bog91]. It follows then that the focal spot size is determined only by the

beam emittance ϵ and the focusing angle α:

$$r_{x,y} \approx \frac{\epsilon_{x,y}}{\alpha_{x,y}}, \tag{3.3}$$

whereby x and y are the coordinate axes transverse to the beam axis. Due to the axial symmetry of the plasma lens focusing properties, α_x is equal to α_y. The SIS beam emittances in both horizontal and vertical planes are not equal and thus the beam cross section after the lens is an ellipse with its area depending on the position along the beam axis.

Due to the high focusing strength of the lens, the focal plane is situated at a distance of 30-70 mm away from the end of the discharge tube. Finally, the distance between the exit window of the lens which is inside the target chamber and the focal plane can be adjusted in the range of 15-40 mm. The focusing strength is related directly to the magnetic field gradient which is determined by the total discharge current. In consequence, the focal spot position and size can be adjusted by changing the discharge voltage and the delay between the ion beam pulse and the first halfwave of the main discharge current.

An important issue in the focusing process is the time interval in which the current density is practically homogeneous, so that the plasma lens functions as an ideal lens. Intensive studies and experiments done during the tests [Ste93, Tau93, Sto94, Neu95, Ste96, Gei97] established that this interval lies around the time of the discharge current maximum. The duration of the first halfwave of the current is approximately 9 μs. It follows that the period when the plasma lens acts as an ideal lens is long enough relative to the ion beam pulse, so that the entire ion beam bunch can be focused in the same way, in both transverse directions.

3.4 Target chamber

The target chamber is the last component of the measurement line at HHT. It is directly mounted on the plasma lens, but electrically insulated to reduce the electromagnetic noise induced by the discharge. The exit window of the plasma lens enters approximately 5 cm inside the chamber in order to enlarge the field of view over the interaction point through the two 15 cm diameter side windows (figure 3.5). Other two ports symmetrically posi-

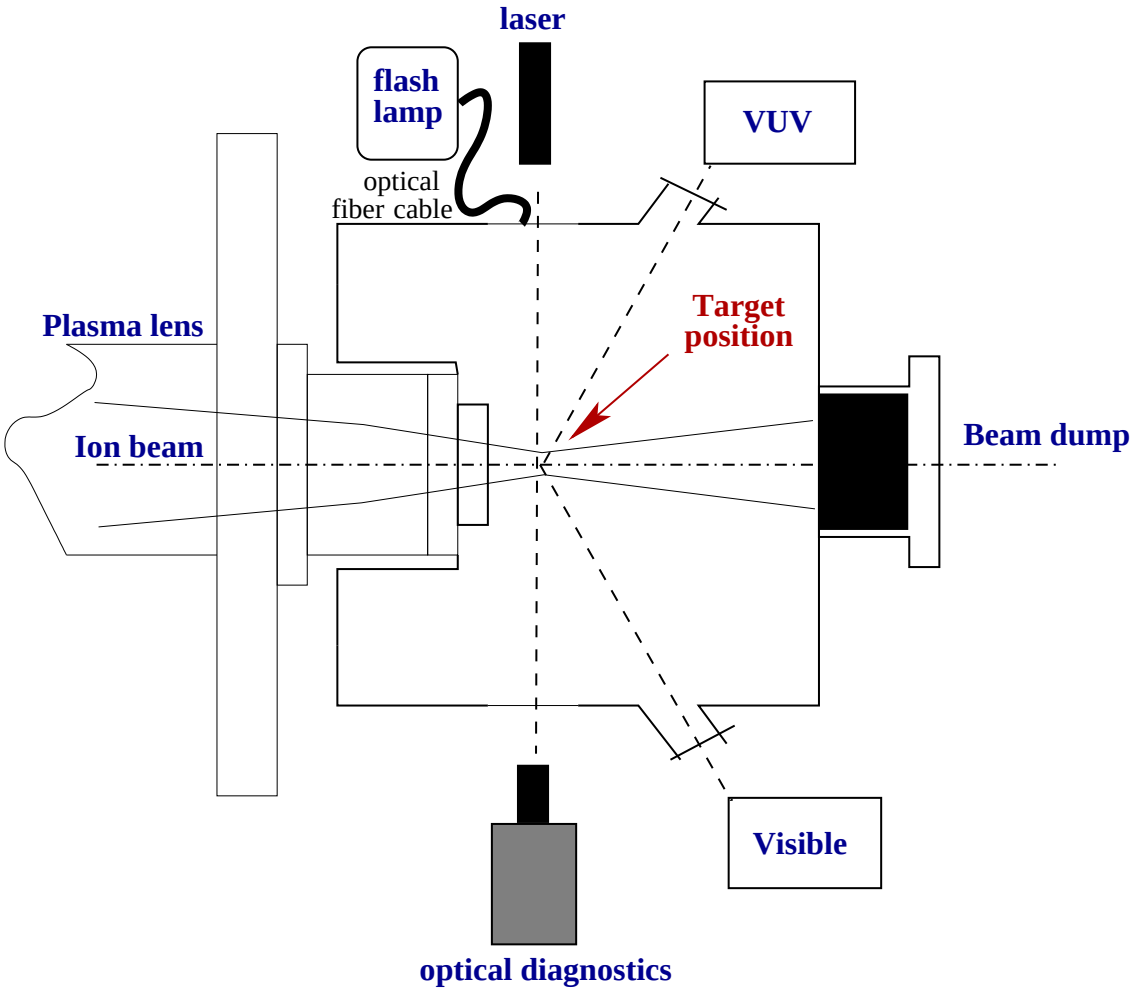

Figure 3.5: The target chamber at HHT. The dashed lines indicate the axis of the diagnostics employed for investigations, such as the time-resolved spectroscopic measurements in visible and VUV ranges, on the 45° ports. The side windows from where the laser and the flash lamp light are guided onto the target were used for the schlieren, interferometry, laser deflection and backlighting shadowgraphy.

tioned at 45° on the sides, with aperture diameters of 50 mm are available for experimental investigations. In the back side a dense graphite block is permanently mounted during the experiments serving as beam dump. There are several flanges of different sizes used for a turbo-molecular pump which evacuates the chamber, as well as for the electrical cables or gas pipes for producing crystals. All the exits, windows and flanges are vacuum tight and after chamber evacuation the pressure in the target chamber can reach values as low as 10^{-6} mbar.

The target chamber has side-removable, quadratic walls, made of stainless steel and

its relatively small dimensions (70×40×40 cm^3) permit to draw the diagnostics near to the examined interaction point. Two types of targets are currently under study: metallic

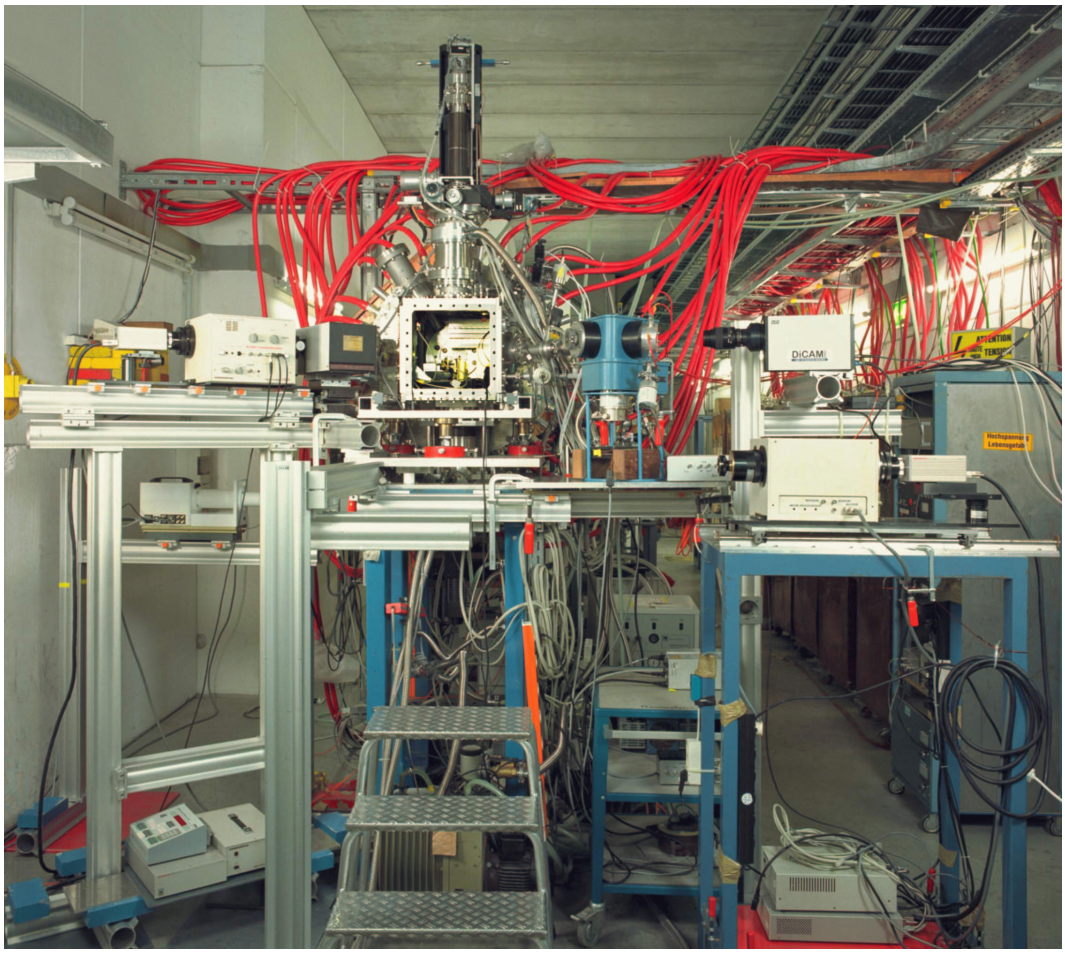

Figure 3.6: The HHT cave, with the target chamber in the middle, mounted at the height of the beamline. The plasma lens is behind and only its high power cables from the capacitor bank can be seen. some of the devices used for diagnostics are set on the sides (streak camera in the right corner and the spectrometers and both lateral sides of the target chamber).

targets (plates, blocks, cylinders, wires) and cryogenic rare gas crystals. The former targets are designed in advance and stored inside the chamber prior to the measurements. At earlier times, a wheel with few stories on which the targets were mounted was used. The target wheel could be moved in all directions by a step motor manipulator. Presently this is replaced by a robot (already mentioned in the 'Beam diagnostics' section) and the targets are stored in shelves mounted on one of the interior walls of the target chamber. The robot seizes the targets one by one and moves them with micrometric precision at the ion beam focus location where holds them during the shot. The cryo-crystals are grown on line. In this scope two parts of the cryogenic system device, namely the cooling head and the growing chamber, are mounted on the target chamber. The cooling head, on which the crystals are grown, is made of stainless steel and it is introduced from below in the target chamber. It has a manipulator on its own, fixed on a high precision vacuum pass (OMNIAX TRANSLATOR, Fa. VACUUM GENERATORS). This allows the manipulator to be translated in all three spatial directions and also rotated by a step

motor which is computer remotable. The maximum range for the movements in the plane parallel to the beam axis is ±10 mm and 400 mm in the vertical direction [Fun99]. This system allows the positioning and orientation of the crystals in the beam as desired. The growing chamber has a remotable, independent manipulator as well, to which is affixed through a thin, metallic pipe. The gas for growing crystals is filled in through an external system of gas tubes and valves and flows finally through the same thin pipe inside the crystal growing chamber.

When the cryo-system is at work, the robot is parked in the back of the chamber until the turn of shots in metallic targets comes. At this point the cooling head is lowered and the growing chamber risen as high as possible so that the robot can move freely on its rails in front of the target shelves and of the plasma lens exit window. All the manipulating systems were planned in a flexible way such that there are no interferences between different devices. Also, an extent for the chamber was constructed and mounted to enlarge the space for those situations in which both the robot and the cryo-system are in use.

Due to the relatively high radiation level in the experimental area during the beam times, all devices and diagnostics are remote-controlled from a separate HHT control room, located 100 m away. Therefore, a data read-out through long coaxial or optical fiber cables is used.

3.5 Beam diagnostics

A set of parameters essential for the experiments at HHT has to be determined prior to any measurements. From the point of view of the energy deposition in the target, the main parameters which can be measured, or in some cases even optimized, are:

- transverse focal spot size and its position in the target chamber;
- beam transmission, number of particles and particle distribution in the bunch;
- time profile of the beam bunch.

The last two quantities are extracted from the voltage signals recorded on storage oscilloscopes from the current transformers which are permanently mounted on the HHT beamline (figure 3.3). The number of particles in the bunch can be inferred from an integrating current transformer (ICT) signal, in principle with an error of less than 2%. The time structure of the beam pulse is measured by a fast current transformer (FCT) situated before the last quadrupole in the beamline. Due to its fast rise time of less than 1 ns [Ber91] and to the high sampling rate of the oscilloscope (0.25 ns) the method guarantees a very good precision. A second FCT, situated before the entrance window of the plasma lens is used for comparison with the signal given by the first FCT. In this way the ion beam transmission on this part of the transport line is evaluated. Further on, the beam transmission should not be affected during the transport through the plasma lens if the alignment on the plasma lens aperture is correct and the beam size not too large. These informations are provided by measurements done by a scintillator which can be moved in or out of the beam, just before the plasma lens entrance. The scintillator has a size of 30×30×0.2 mm and it is mounted at 45° relative to the beam axis. The light emitted is measured by a CCD camera (FlashCam PCO) with an exposure time between 1 μs and 1 ms.

An array of 3 identical scintillators, with an active area of 8×8 mm^2 each is placed inside the target chamber on the beam axis by a computer controlled manipulator (robot). The scintillators are orientated at 45° with respect to the beam axis and they are used in the search of the beam focal spot location and its size. The cerium-doped quartz material of the scintillators was selected due to its high thermal resistance required in the case of such intense beams. Another advantage is the linear relation between the scintillation light and the beam intensity [Lau93]. The observations are done with a fast shutter camera (DiCam PRO PCO) situated at 90° relatively to the beam direction. Limitations in the spatial resolution are caused by the scintillator thickness and by the 45° orientation of the array. Since a careful inspection of the focal spot size and position is of great importance for the experiments, a second measuring method is employed for comparisons. It consists in monitoring a bright trace that the ion beam leaves while passing through the target chamber filled with gas due to self-emission processes. Over the entire spatial range permitted by the field of view of a fast camera set for observations, the beam envelope, divergence and focal size can be visualized with a good spatial resolution. By appropriate spatial calibrations also the focus location can be precisely detected. The intensity of emitted light does not necessarily scale with the energy deposited by the beam in the excitation process, therefore no attempt of this kind was made. The method can certainly be further studied and developed. The background gas is usually air, at atmospheric pressure. A set of measurements was done in N_2 as well, but there were no significant differences relative to the measurements in air. The accuracy increases in fact

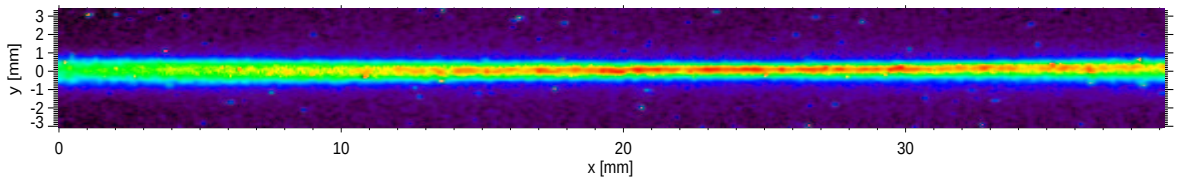

Figure 3.7: Trace of a $^{238}U^{73+}$ (200 MeV/u) in the target chamber filled with air at 1 bar pressure. The picture was taken with a fast shutter camera with a resolution of 1024×1024 pixels and an exposure time of 1 μs covering the entire beam pulse duration.

with the ion beam intensity. Figure 3.7 illustrates an example of a U beam trace in air at atmospheric pressure and the plot of its envelope over 40 mm is shown in figure 3.8(a). From the Gauss fit of the spatial profile a focal spot of 0.7 mm (FWHM) in the vertical axis was determined located at 24 mm away from the plasma lens exit window (figure 3.8(b)). For the visualization of the focal spot in both directions, horizontal and vertical,

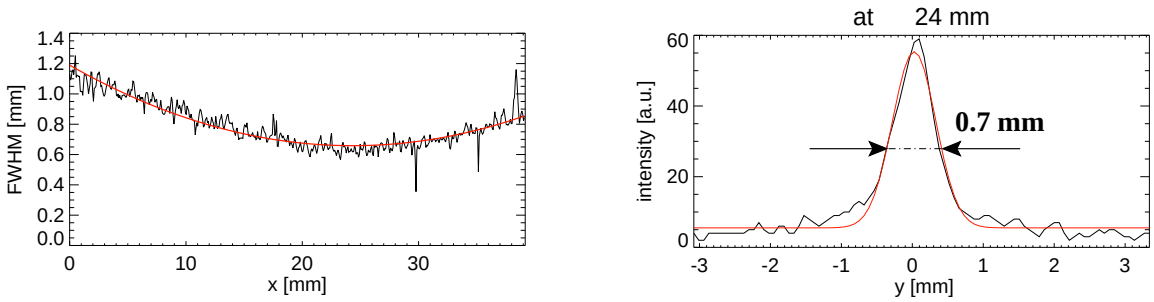

(a) (b)

Figure 3.8: (a) Envelope of the U beam over a range of 40 mm, in the target chamber; (b) Gauss fit of the spatial profile in the focus. The beam size is measured on the vertical axis.

a long mirror which is 45° inclined relative to the beam track can be used to scan the envelope. The image contains then simultaneously a side- and a top view of the beam, so that the best aspect ratio can be found and the location marked as optimum target position. The coordinates are given with a micrometric precision of by the controller of the manipulator and used to adjust the target such that the Bragg peak and the focus coincide.

3.6 Cryogenic system: set-up and crystal growing process

The cryogenic system operation is based on a closed cycle between an adiabatic He compressor (UCH 445-LEYBOLD) and a cooling head (UCC 1105-LEYBOLD). The cooling head consists of two copper parts fixed one to another (figure 3.9) which are cooled in a two step process [McM60]. The first phase takes the lower part to a temperature of around 45 K with a power of 45 W. Second phase lowers the temperature further, being able to reach values of 5.31 K at 0 W and 9.26 K at 7 W power consumption [Fun99]. It is important that the cooling head operates in conditions of vacuum better than 10^{-3} mbar to avoid convection heat transfer to the environment. At low temperatures, the radiation shielding surrounding the second stage of the cooling head, as well as the sample holder on top act as cryolitic pumping surfaces reducing the pressure in the vacuum chamber to 10^{-7} mbar. The shielding is made of Ni-doped copper with a wall thickness of 0.5 mm and has the role to stop any heat-radiation transfer to the holder. A better thermal contact is achieved by applying layers of indium between the first stage and the shielding, as well as between the first stage and the holder.

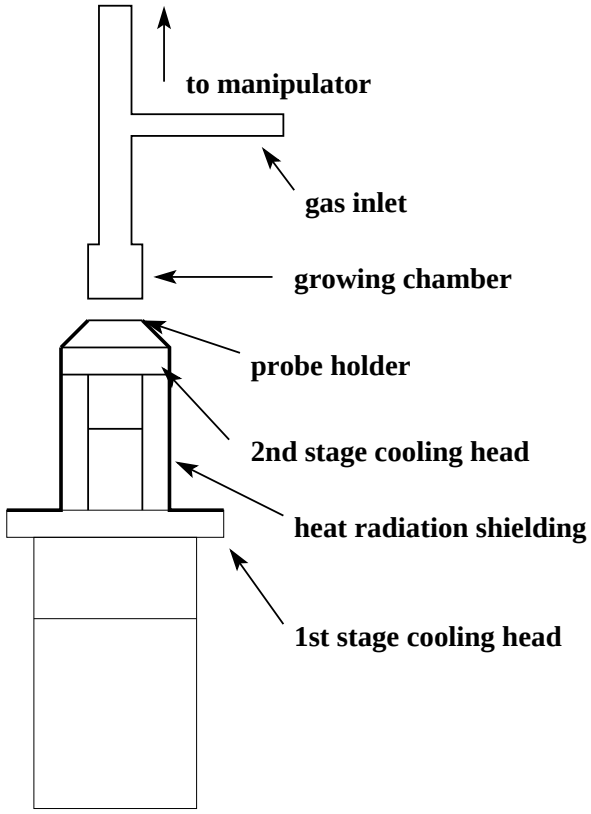

Figure 3.9: The cooling head with its 2 stages and the growing chamber.

The probe holder has to meet two important requirements, namely a high thermal conductivity coefficient and a good, tight contact with the growing chamber. The first condition is solved by the oxygen-free copper material from which the holder is made, while the second by using another 0.3 mm thick, milled and then carefully smoothed layer of indium on the surface of the holder. In this way a firm sealing is assured when the growing chamber lowers, before the gas is filled in. This sealing method is necessary especially

in the case of light molecule gases, such as H_2, where the sublimation temperature is lower than the temperature of the growing chamber during growing. Heavy-molecule gases instead freeze rapidly when escaping through eventual small gaps and the chamber is closed in this way. The crystals are produced in a quadratically shaped chamber with outer dimensions of 10×10 mm and 1 mm thickness. It is made from stainless steel for the same reason of preventing heat conduction to the environment. A thin pipe of the same material, with the inner diameter equal to 5 mm connects the growing chamber to the manipulator and serves also as gas inlet (figure 3.9).

The main parameters to be controlled during the growing are the temperature of the cooling head and the gas pressure inside the crystal chamber. The temperature is measured by a ceramic oxihibrid temperature-dependent resistors, with a highly increased sensitivity at low temperatures and resistance against ionizing radiation. A gas inlet was designed for the continuous pressure monitoring during the crystal formation. The gas flow is controlled and regulated using a Baratron flow control valve and pressure sensors which can be operated from the HHT control room.

The entire set-up and the growing process, described in the following, were thoroughly developed and documented and a complete description of this work can be found in [Fun99]. The growing process starts when the cooling head temperatures reaches 6.5 K,

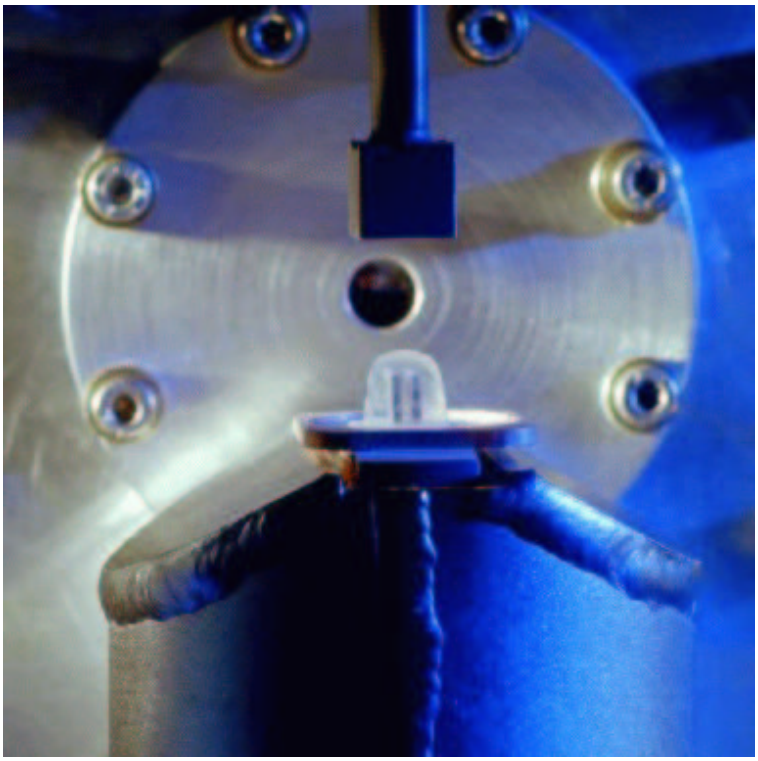

Figure 3.10: Picture of a Ne cryogenic crystal with two Pb plates embedded, the so-called composed target. The crystal has a width of 8 mm and the plates are 2 mm thick each.

while the radiation shield is at 30 K. The gas is introduced into the growing chamber at room temperature, causing an increase of 1 K of the temperature when it gets in contact with the probe holder. The temperature drops rapidly again, since the released crystallization heat cannot be removed fast enough through a crystal, which is characterized by poor conductive properties. The crystal grows until the heat transport is too weak to keep the crystal surface below the sublimation temperature. The process lasts from 5 to

15 minutes, depending on the gas type. At this point an equilibrium between condensation and sublimation is reached. The condensation degree is given by the decrease of the pressure in the growing chamber while the gas inlet valve is closed. This procedure provides informations about the completion of the growing process which cannot be checked optically. After the crystal is grown, the remaining gas is evacuated and the chamber is lifted. The pumping prevents formation of snow-like coating on the crystal upper surfaces which destroys its transparency. Previous measurements showed that, from the point of view of optical quality, best results are obtained for crystals created at pressures below the triple point of the respective gas [Dor96].

The lowest temperature at which the cooling head can keep the crystals is generally around 6.5 K, except for hydrogen in which case this temperature is too high and the crystal evaporates. If kept in vacuum, the crystals can last for hours. The most long-standing are the heavy-gas crystals, such as Xe and Kr crystals, and the least lasting are the H crystals, where the evaporation is a matter of some minutes.

Recently, uniform crystals with metallic plates embedded, the so-called compound targets, were successfully obtained. As explained above, the growing process requires a good thermal conductivity between the cooling system and the cryogenic target. A gradient temperature develops always from the surface of the cooling head up to the top side of the crystal, so that the growing process stops when the top cryogenic layer reaches the sublimation temperature. This can become an obstruction in the growing process of compound targets. To ensure a good thermal contact between the metallic plates of the target and the cooling head, the target has to be mounted on a support made of the same material as the cooling head, which is copper. On both upper and lower sides of the support smooth layers of indium have to be placed. The lower indium layer plays the role of improving the thermal contact, while the upper one has to seal firmly the growing chamber on the support. If the metallic plates inside the compound target reach temperatures close or under the temperature of the growing cryogenic layer, the crystal will grow uniformly around the metallic surfaces providing interfaces without gaseous bubbles. Figure 3.10 shows a picture of such a crystal-metal compound target. This type of target is of special interest for the two-confiner cold compression study. In this scheme, the ion beam is stopped in the front metallic plate from where the generated shock waves emerge in the crystal layer. The compressed material is kept confined between the two metallic plates, whereas the free sides permit optical access for observations.

Chapter 4

Experimental results and numerical simulations

In this chapter the experimental diagnostics set to investigate the matter response to the action of the ion beams are described. These are backlighting shadowgraphy, schlieren, interferometry, laser deflection, pressure gauges and time-resolved spectroscopy in visible and vacuum-ultraviolet regions. The chapter also contains a theoretical simulation description and the result of these calculations performed for one of the beamtimes, with Kr ions in multilayered targets. A common target design for all the experiments is explained at the beginning of the schlieren measurements part. The table below gives, in chronological order, an overview about the parameters of the beams employed in the experiments performed during two years at HHT experimental area. The symbol (*) in first column indicates those experiments which were selected for presentation in this work.

time	*ions*	$E[AMeV]$	$N/pulse$	$\Delta t[\mu s]$	diagnostics
nov. 99	$^{40}Ar^{11+}$	300	2×10^{10}	0.7	b. shadow.
mar. 00	$^{238}U^{73+}$	200	$\sim 10^{9}$	0.7	b. shadow.; schlieren
may 00*	$^{83}Kr^{36+}$	300	$\sim 2 \times 10^{10}$	0.7	b. shadow.; schlieren
aug. 00*	$^{197}Au^{65+}$	300	1.75×10^{9}	0.6	b. shadow.; schlieren
oct. 00*	$^{16}O^{8+}$	200	$\sim 5 \times 10^{10}$	1.25	spectrosc. VUV
dec. 00*	$^{40}Ar^{11+}$	300	$\sim 5.5 \times 10^{10}$	0.7	spectrosc. visible
jul. 01	$^{197}Au^{65+}$	300	$\sim 2 \times 10^{9}$	0.6	M-Z interf.;press. gauge
aug. 01*	$^{238}U^{73+}$	300	$\sim .1.5 \times 10^{9}$	0.6	M interf.;defl.;press.gauge

Table 4.1: Beamtimes and diagnostics employed for ion beam-matter interaction investigation. The abbreviations and symbols stand for: E= energy per nucleon; N= number of particles per pulse; Δt= pulse duration; diag.= diagnostics; b. shadow= backlighting shadowgraphy; spectrosc.= spectroscopy; M-Z/ M interf.= Mach-Zehnder/ Michelson interferometry;pres.gauge= pressure gauge measurements; defl = direct laser deflection measurements.

4.1 Backlighting shadowgraphy

4.1.1 Principle of the method

Investigation of free-surface expansion of a target heated by heavy ion beams was one of the first steps done in experiments concerning characterization of heavy ion beam interaction with solid matter. Qualitative information about the matter behavior together with quantitative evaluations of the velocity of the matter dynamics can be obtained by employing a time resolved backlighting-shadowgraphy technique.

A backlighting-shadowgraph system acts as a contour projector for objects obscuring light from a source situated behind with respect to the detector. The detection occurs at the location of the focused image, compensating the light deflection caused by refractive disturbances. In this way, an outline of the examined region is formed as a response to the density isolines encountered by the luminous flux. For varying densities a more detailed intensity fluctuation caused by different levels of light absorption is provided. In practice, the advantage of the shadowgraph systems is the experimental simplicity combined with a comprehensive perception of the examined process.

On the other hand, quantitative measurements of densities causing the light absorptions are difficult and imprecise. Nevertheless, in the present case the method is well suited for hydrodynamical measurement of the expanding matter, with a satisfactory accuracy, by backlighting technique.

In this purpose a Xe flash lamp with 250 J input energy was used as source. It emits light on a continuum spectrum in a 10 μs pulse of high intensity, followed by a 50 μs low intensity tail. The light was guided perpendicular to the ion beam direction and parallel to the free surface to be investigated. The shadow of the moving surface was projected onto a fast multiframing camera (Hadland ULTRA 68) capable of recording 8 frames simultaneously, with exposure times from 10 ns to 1 ms. From the eight frames taken at different times not only the velocity of the expansion was determined, but also details of the process dependencies on the ion beam energy deposition were inferred, as it will be discussed in the following.

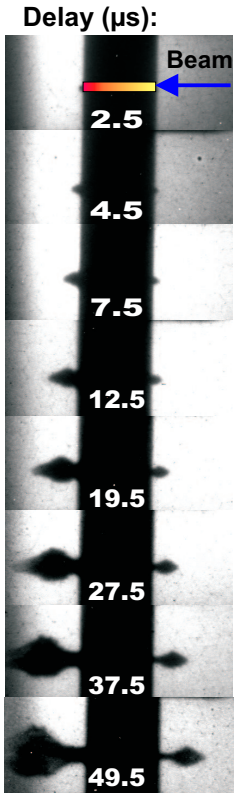

Figure 4.1: Backlighting shadowgram of a 6 mm long Pb plate heated by U beam.

4.1.2 Results

The hydrodynamic response of matter to volume heating by heavy ion beams was intensively studied in previous experiments [Sto98, Fun99] and the process became better understood. Nevertheless, the velocity of ejected material moving outwards from a free surface of the heated material of the target is a characteristic of each ion beam-target combination and constitutes a benchmark for the hydrodynamic codes used for simulations. In addition to this, the experiments were designed to evaluate the effects of different target materials having geometries with or without the stopping range included. The metallic targets, such as Pb plates, behaved as expected, while for the cryogenic rare gas crystals

the situation was different.

Figure 4.1 depicts a Pb target, 6 mm long, heated by a $^{83}Kr^{36+}$ beam with 300 AMeV particle energy, 2×10^{10} particles contained in a pulse of 700 ns duration. The stopping range is 6 mm in this case. The hydrodynamic process starts around 2.5 μs and lasts for long times (above 50 μs). Clearly it is visible the difference between the matter expansion motions in the two directions: from the side where the beam enters the jet of matter moves with lower velocity than the jet on the rear side, at the location of maximum energy deposition. Figure 4.2(a) shows the displacement of the matter front, on the beam axis, at different times. The curves were plotted using the data recorded with the framing camera from shots performed in two identical lead targets, in both directions. The agreement between the two shots shows a good reproducibility. Therefore only one fitting curve was plotted and it was found that the velocity in the first stages of expansion, up to around 15 μs, reaches a value of 220 m/s at the rear side of the target (Bragg peak); after this time, the velocity decreases slowly reaching, after 30 μs a two times lower speed than at the beginning. For the matter jet at the front side of the target, where the energy deposition is much lower, the velocity is also lower, around 70 m/s, but more constant in time.

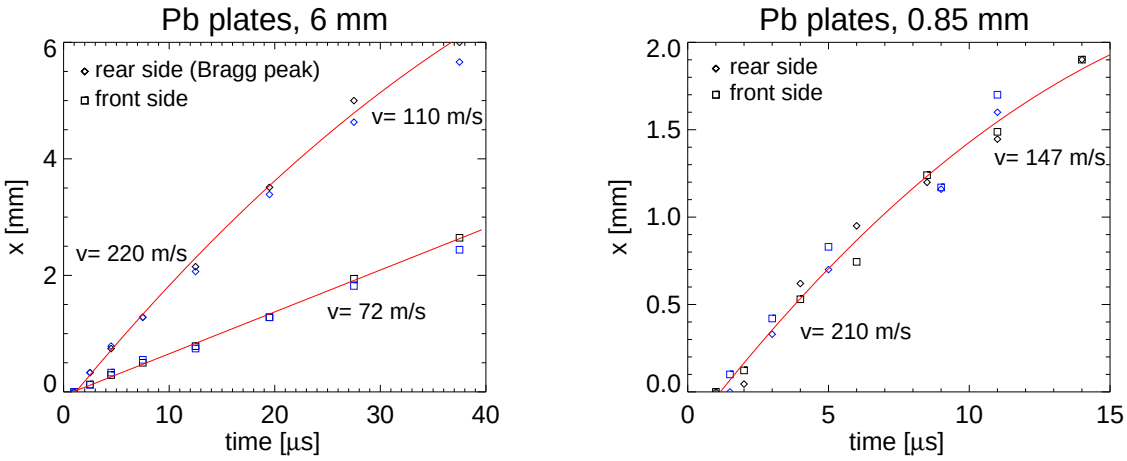

(a) (b)

Figure 4.2: (a) Plot of expanding matter in both directions, for two distinct, identical Pb plates of 6 mm length, heated by a Kr beam; (b) expanding matter for 0.85 mm Pb plates, heated uniformly by an U ion beam.

The response of a Pb plate thinner than the stopping range is of a different manner. The energy deposition of the ion beam is uniform along the target and the matter expands with very similar velocities from both free surfaces of the target. Experimental data measured for 0.85 mm Pb targets, heated by a $^{238}U^{73+}$ beam with 300 AMeV and 1×10^{9} particles in a pulse of 1 μs duration are plotted in 4.2(b). The curve shows that the velocity reduces also in this case, from 210 m/s to 147 m/s, around 10 μs after the beam pulse.

For cryogenic rare gas crystals, which are the second type of targets considered for comparisons, the hydrodynamic process does not show such a critical dependence on the presence of the Bragg peak inside the target. The jets of expanding matter from both

front- and rear surfaces of the target behave as there would be an uniform energy deposition in either case, when the beam is stopped in the target and when the beam propagates further. An exemplification is given in figure 4.3(a) and 4.4(a), where shadowgrams of a Xe crystal under the action of Kr ions and a Ne crystal heated by U ions with the parameters mentioned above are shown.

Higher expansion velocities than in the metallic targets case were measured for crystals, a maximum of 470 m/s for Ne and 350 m/s for Xe crystal. After 20 μs the motion is slower, an effect which is more pronounced for Ne. An illustration of these measurements is presented in figure 4.3(b) and 4.4(b).

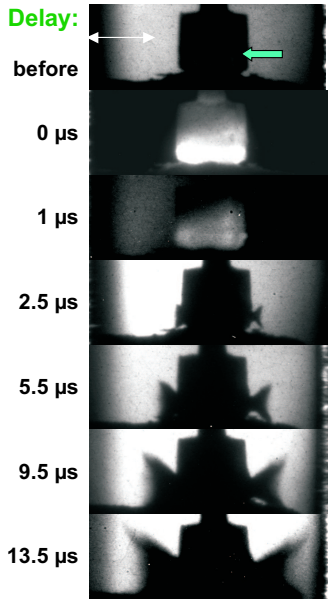

(a)

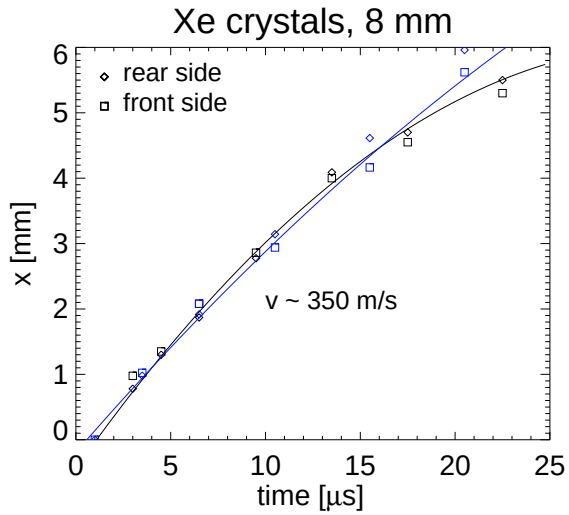

(b)

Figure 4.3: (a) A Xe crystal in which the ion beam (Kr, 300 AMeV) is not stopped; second frame (without flash lamp) shows the light emission of Xe; (b) expansion of the matter in vacuum in both directions, from the free surfaces of two Xe crystals, plotted in different colors.

During the interaction with the ion beam, the density of the target decreases considerably and a spatial shift of the Bragg peak occurs. At crystals, these shifts draw the Bragg peak region outside of the crystal and the matter heating is finally almost uniform. An indirect proof of such effect was given by the observation of symmetrical expansion of the matter from the free surfaces. According to the simulations performed for the target presented in 4.4 using BIG2 code (see chapter 4, section 4.3) the density of the Ne crystal drops to a third of the initial one after 100 ns. In the case of metallic targets the initial density during heating undergoes a decrease at lower rates. In the case of the Pb plates the Bragg peak remained inside the target and, as a consequence, more pronounced

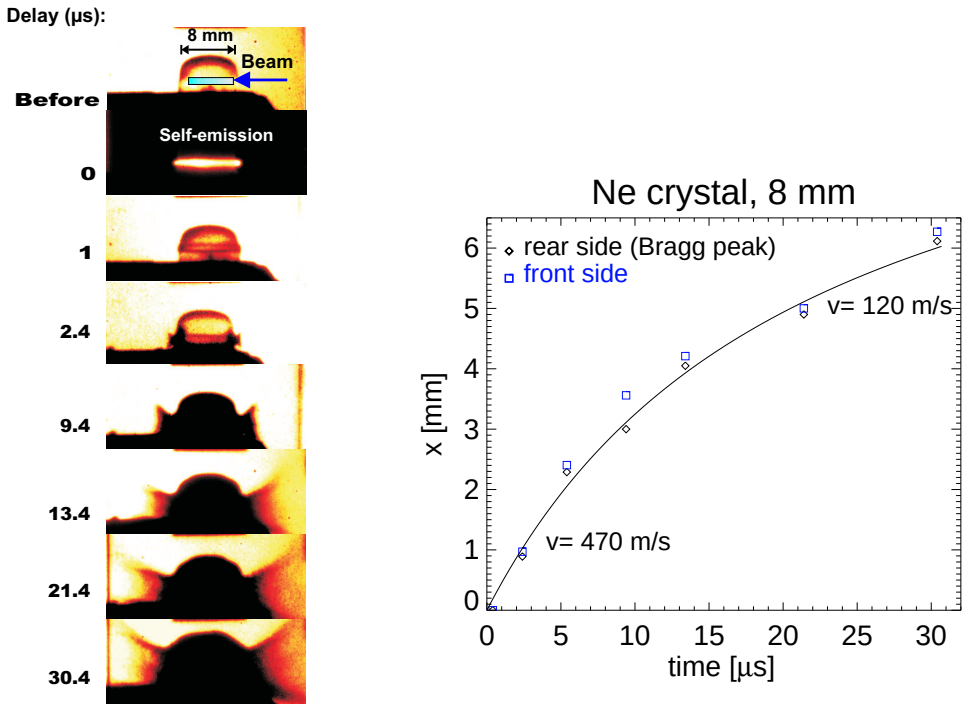

(a) (b)

Figure 4.4: (a) Backlighting shadowgraphy picture of a Ne crystal heated by a U beam. The Bragg peak lies inside, as it can be noticed from the second frame (no flash lamp), where the self-emission was recorded; (b) expansion of the matter in vacuum from the rear and front side of a Ne crystal (U beam).

dynamics were observed in the Bragg region.

4.2 Schlieren investigation of shock waves

4.2.1 Fundamentals

Phenomena related to the stress waves induced by the heavy ion beam in matter were investigated by means of several optical probing procedures. Using a transparent medium as sample, a dark-field imaging schlieren technique could be employed. The method is commonly used for quantitative analysis of cylindrical or spherical index of refraction distributions [Nol86], suitable for the present case which was described in section 3.5. The schlieren images experimentally obtained provide important information on the dynamics, geometry and structure of the shock waves traversing the target. Useful estimations of density gradients are obtained with support from theoretical simulations.

The schlieren method works on the principle of bending of light rays under certain angles due to density gradients transverse to the light propagation direction, translated into detection of spatial variation of the refractive index. The detection takes place at the location of the focused image of the refractive disturbance. The dark-field schlieren introduces subsidiary elements into the optical system, that transform the structurized angular distributions of the deflected rays into intensity distributions [Dec85], as it will be described in section 5.1.2.

A very useful relation in any schlieren measurement is the derivation of angular deflection which connects the deflection angles with the density gradients in the refractive disturbance region. This relation can be obtained with the aid of the scheme illustrated in figure 4.5 [Jah71]. A wavefront propagating along the y axis arrives at the same time

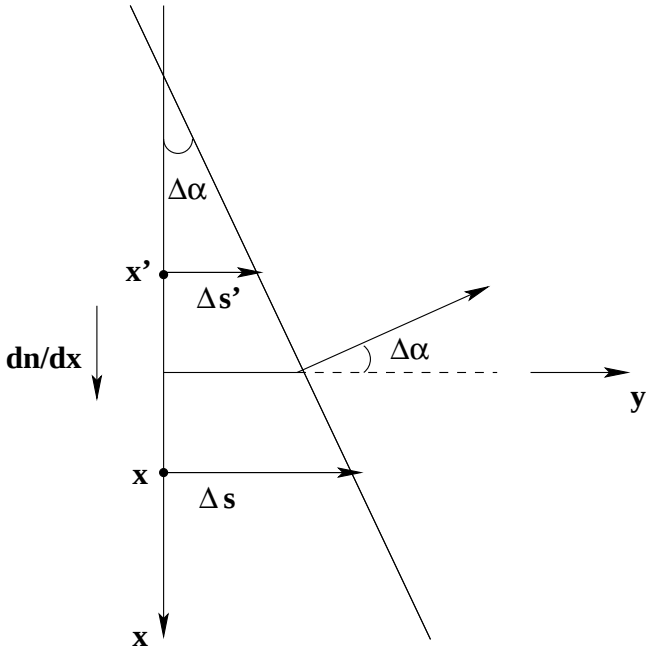

Figure 4.5: Angular deflection of a wavefront due to a refractive index gradient.

at x and x', which delimitates the region containing the gradient. After a time interval Δt, the wave parts incident at x and x' travel distances Δs and Δs' proportional to their velocities:

$$\Delta s = \frac{c \cdot \Delta t}{n} \quad , \quad \Delta s' = \frac{c \cdot \Delta t}{n'} \tag{4.1}$$

with:

$$n' = n \quad + \quad \frac{\partial n}{\partial x} \cdot \Delta x \quad \text{and} \quad \Delta x = x \quad - \quad x'. \tag{4.2}$$

Since: $\Delta s' \quad = \quad \Delta s(n/n')$, it follows that:

$$\Delta s - \Delta s' \quad = \quad \frac{\Delta s}{n} \cdot \frac{\partial n}{\partial x} \cdot \Delta x. \tag{4.3}$$

The advancing wavefront is now represented by the line joining the new positions after Δt and its normal deviates from the y axis by an angle $\Delta\alpha$. The difference Δs - Δs' can be expressed in terms of angles by projecting the advancing wavefront on the x axis, namely $\Delta s = x\Delta\alpha$ and $\Delta s' = x'\Delta\alpha$ and $\Delta s - \Delta s' = \Delta\alpha\Delta x$. Combining with the equation (4.3) the derivation of the angular deflection is obtained:

$$\Delta\alpha = \frac{1}{n} \cdot \frac{\partial n}{\partial x} \cdot \Delta s. \tag{4.4}$$

Generalized for a limiting process to $d\alpha = \frac{1}{n} \cdot \frac{\partial n}{\partial x} \cdot ds$ in the case of non-constant density gradients and small deflections from the y axis, the above equation leads to the relation for the deflection angle in radians:

$$\alpha_x \quad = \int_0^{y_1} \frac{1}{n} \, \frac{\partial n}{\partial x} \quad dy. \tag{4.5}$$

For a plasma system, the refractive index is given by [Lov]:

$$n_p \quad = \quad (1 - \frac{n_e}{n_c})^{1/2} \tag{4.6}$$

where n_e is the electron density and n_c the cutoff density: $n_c = 4\pi^2 c^2 \epsilon_0 m_e/(e^2\lambda^2)$. Using equation (4.5), a relation between the deflection angle and the electron density can be established:

$$\alpha \quad = \quad -\frac{\lambda}{2\pi} \frac{e^2}{m_e c^2} \int \frac{dn_e}{dx} \quad dy \tag{4.7}$$

where m_e the electron mass and λ is the probing light wavelength. For solids, a clear, analytical relation between the refractive index and density has not been found. However, in these experiments the optical observations were done in plexiglass, which is considered a visco-elastic fluid. Therefore, in a sufficiently good approximation the Clausius-Mosotti (Lorentz-Lorenz) relation [Emr] for fluids could be used, in the following form:

$$\frac{n^2 - 1}{n^2 + 2} \quad = \quad K(\lambda) \cdot \rho \tag{4.8}$$

where K(λ) is a constant depending on the wavelength and material and ρ is the mass density of the material.

Figure 4.6 shows the situation of weak shock waves induced by the heavy ion beam in a target. A spherical shock, expanding in time up to the boundaries of the target is propagating in the beam direction, represented by the x axis. A laser ray crossing transversely the region of non-constant density gradients created by the shock wave will be deviated from its path under an angle which can be defined with the aid of equation 4.5. Only the

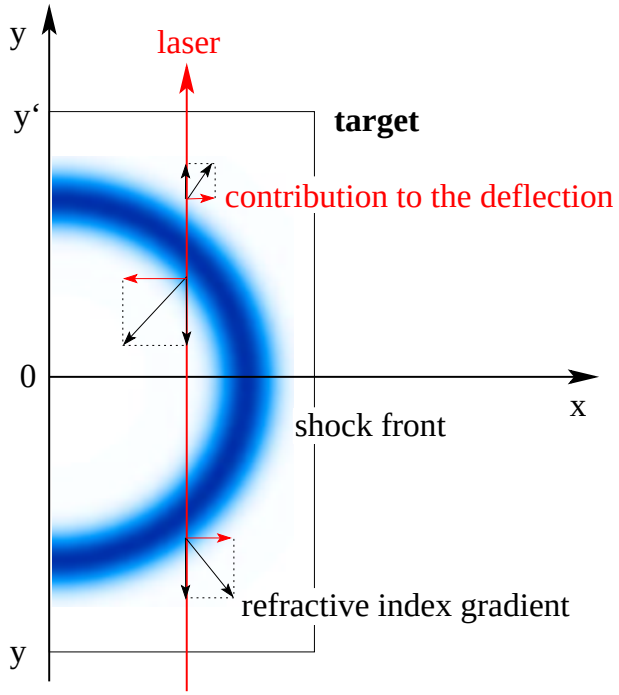

Figure 4.6: Laser ray path through a region of refractive index gradients induced by a spherical shock.

perpendicular gradients to the laser path within the target limits y and y' will contribute to the deflection of the ray.

With measured deflection angles as it will be presented in the following sections of this chapter, the calculation of the densities reached by the stressed material was difficult due to the nonlinearities in the gradient distribution introduced by the spherical shape of the shock wave, integrated over the entire thickness of the target traversed by the laser beam. Therefore the applied procedure was to compare the angular deflections measured experimentally with the calculated ones by using the density gradients resulting from theoretical simulations and introducing them in the Clausius -Mosotti relation 4.8. A discussion of this matter follows in the theoretical part of this chapter.

4.2.2 Schlieren set-up

The optical system used for measuring, in the dark-field manner, the deflection angles caused by the stress waves in the plexiglass section of the target is shown in figure 4.7. As light source a cw He-Ne laser, at 632.8 nm wavelength and 5 mW power was used. The laser beam was collimated by the first lens, L1, which in combination with a second lens, L2 and a 20 μm pinhole forms a telescope in order to expand the laser beam at least to the dimension of the target. A refractive index gradient, represented by an arrow in the target, deviates the ray passing through the gradient along the dotted path, instead of the solid line path which would be followed in the absence of any disturbance. In either case, the ray passes through the same location in the detection plane, where the lens L3 images the disturbance. In the focal plane of the lens L3 every incident direction α has a unique distance from the optical axis equal to $f \cdot \alpha$, where f is the focal length of the lens L3. All undeviated rays will intersect the optical axis in the focal spot of L3, while the deviated ray will pass above it. If a beam stop is placed at the location of the focal spot of this last

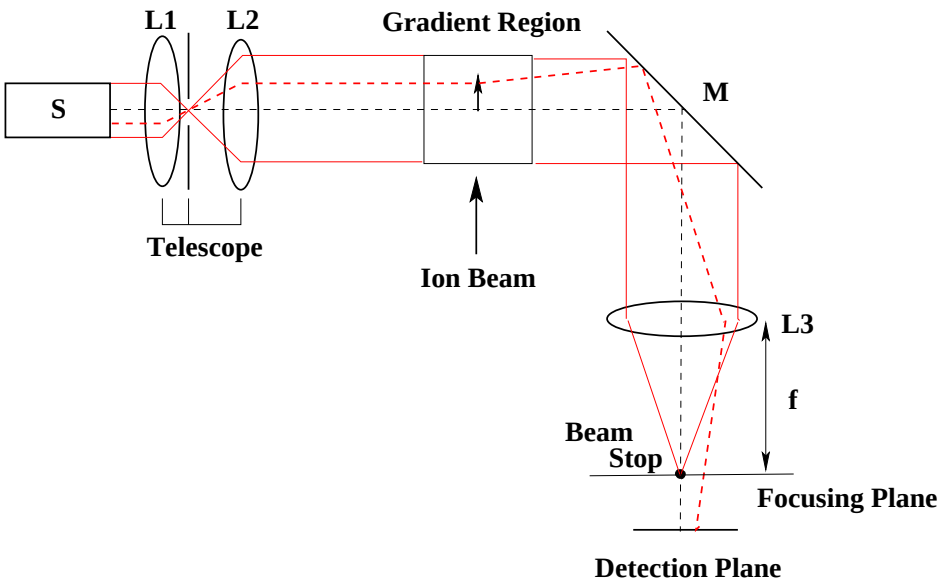

Figure 4.7: Schlieren set-up for measuring the angular deflections of a laser beam by density gradients induced in a plexiglass target.

lens, in the absence of any perturbations all the light from the source will be prevented from reaching the detection plane, whereas in the presence of the refractive disturbance the deviated rays only will pass the obstructer and will contribute to the image of the disturbance in the detection plane. In practice, since the source has a finite extent, a background of intermediate illumination in the detection plane will be always present, with brightening caused by the deflected and unobstructed rays or darkening if the bent rays are obscured by a part of the beam stop. Deflections in all directions, suitable for 2D schlieren visualizations, can be detected if the beam stop is round and placed in such a way that none from the deviations is blocked. For a knife-edge obstructer only a component of the gradient perpendicular to the knife-edge orientation can be recorded, the image intensity being not affected by the displacements along the knife-edge (see fig.4.8). Two types of beam stops were used during the measurements: round beam stops

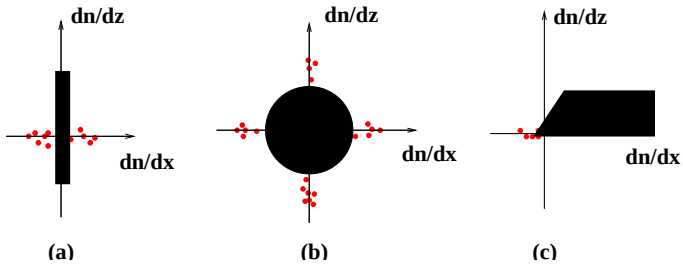

Figure 4.8: Types of beam stops used in schlieren systems. The spots around represent the deflected rays which pass the beam stop in a direction respective to the refractive index gradient sign. (a) cylindrical wire, allowing rays deflected by both positive and negative gradients, for 1D schlieren measurements; (b) round beam stop, which can be passed by rays deflected in all directions; (c) the classical knife-edge.

and cylindrical wires with diameters varying between 0.8 mm and 1.6 mm. In both cases, they were placed in the focal spot of a lens (L3) with a focal length $f = 1$ m or 0.5 m which blocks a laser beam focal spot of 0.2 mm. The laser beam was expanded by the

telescope to 30 mm, covering the entire region of interest in the target. In the detection plane a streak camera (HAMAMATSU C2830) providing a time resolution of 150 ns and a 2D fast-shutter camera (PCO-DiCAM PRO) were placed simultaneously by using a 50% transmission mirror. Each camera was focused onto the target to gain space resolution and to compensate intensity variations of the laser light due to the deflected rays.

Information about the sensitivity of the schlieren system and the laser focal spot size can be obtained by an off-line *in situ* calibration of the set-up. In order to simulate the laser rays deflection the beam stop is moved in small steps away from the laser focal spot, perpendicularly to the laser beam and along both the increasing and decreasing gradient directions. The starting point is when the laser is completely blocked by the beam stop, a case for which in the detection plane an illumination background is still present due to the finite extent of the source. For each new position of the beam stop of a known displacement d, intensity levels of the recorded pictures are measured and plotted versus corresponding deflection angles $\alpha = d/f$. Figure 4.9 shows the curve obtained as

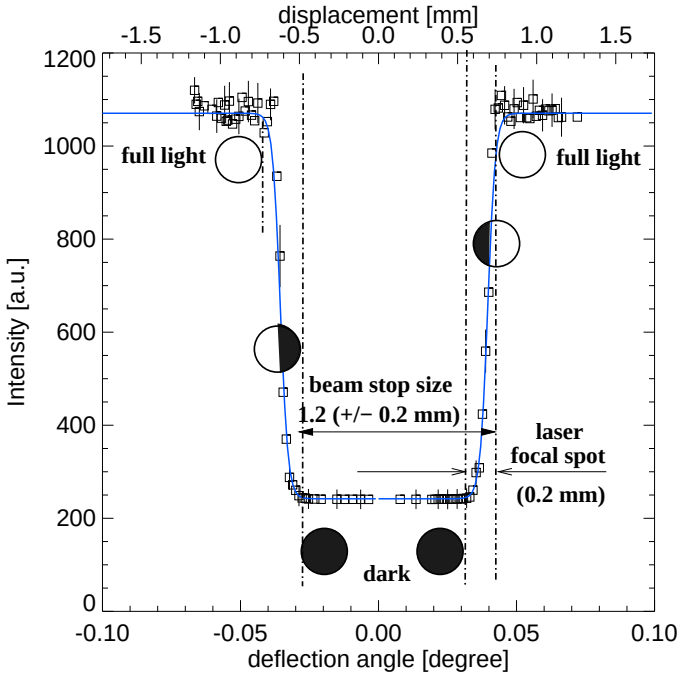

Figure 4.9: Deflected light curve simulated by moving a 1 mm beam stop away from the laser focus, transversely to the laser beam direction. The origin indicates the initial position of the beam stop, as it was during the experiments.

described above, fitted with a Boltzmann distribution function. From this curve a laser focal spot of 0.2 mm diameter was found, as well as a minimum deflection angle of 0.6 mrad to which the system is still sensitive. The intermediate points between minimum and maximum angles are not to be taken into account, since the amount of deflected light would depend also on the spatial distribution of the refractive index gradient.

4.2.3 Target design and beam parameters

The target configuration was adapted to the requirements of the experiment:

- in order to obtain cold compression, the heating of the test medium by heavy ion beam has to be avoided; this was achieved with a metallic block at the front side of the target where the beam was stopped completely after depositing its energy;

- for the transmission of the laser light in schlieren measurements a transparent material is required; a plexiglass block with parallel faces was therefore used as 'window' for the optical observations;

- a cold confiner at the back end of the target can prevent the expansion of the material subjected to the compression and rarefaction waves action; this was an aluminum layer of a few millimeters thickness, chosen on the principle of shock wave reflection at boundaries between two different materials: if the shock wave travels from a material to another one with higher acoustic impedance, the reflection will be a shock wave as well; for the opposite case, when the acoustic impedance of the second material is lower, the reflection will be a rarefaction wave (see figure 4.10). The transmitted wave is always a shock [Zel67].

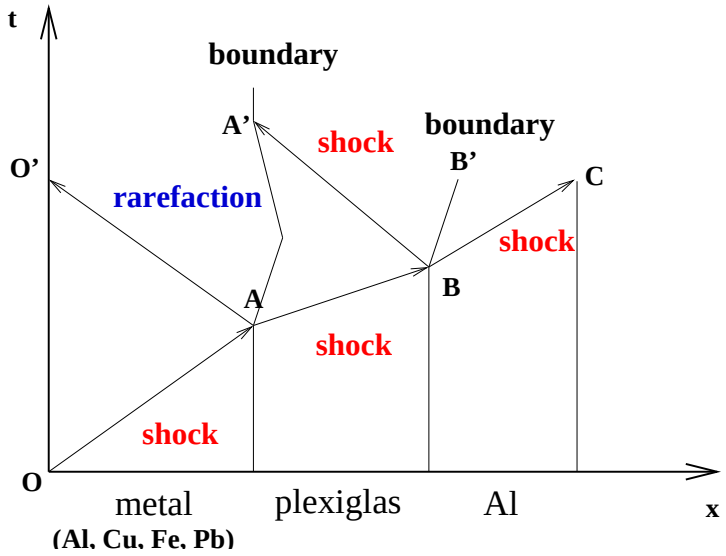

Figure 4.10: Scheme of shock waves crossing boundaries between two different materials.

The schlieren technique was used as a diagnostic tool in two experiments employing different ion beams, with the parameters tabulated in the table 4.2.

ions	energy $[MeV/u]$	N $[particles/pulse]$	pulse duration $[ns]$
$^{83}Kr^{36+}$	300	$2 \cdot 10^{10}$	700
$^{197}Au^{65+}$	300	$1.75 \cdot 10^{9}$	700

Table 4.2: Parameters of the heavy ion beams employed in schlieren measurements.

For all metals used as absorbents (Al, Cu, Fe and Pb) and ion species employed in the experiments, the stopping ranges were calculated using the TRIM code [Zie96]. According to numerical simulations, the heavy ion beam can heat material to a few thousand Kelvin and thus the stopping data provided by TRIM for cold matter still can be used. To the

calculated ranges few millimeters were added to prevent the penetration of the plexiglass layer by the ion beam due to the Bragg shift effect already discussed in the section about the backlighting shadowgraphy. Figure 4.11 illustrates two types of multilayered targets used in the three mentioned experiments.

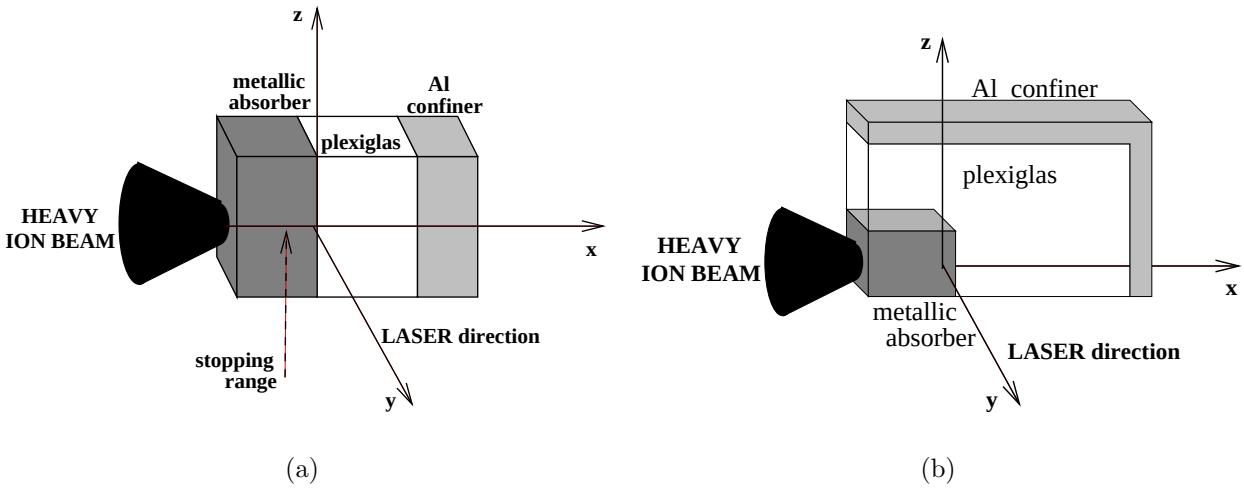

Figure 4.11: a)Target configuration for the 1D schlieren experiments with Kr ions. The plexiglass range was of 7 mm and the absorber materials were Al, Cu, Fe and Pb. Wires of different diameters were used as beam stops. (b) Target configuration for the 2D schlieren experiment with Au ions. The plexiglass range was of 15 mm and the same absorber materials like in case (a) were used and a round beam stop. In both cases, the plexiglass was completely illuminated by the laser beam, which propagates along y axis.

4.2.4 Results

This chapter presents the results obtained by applying the dark-field schlieren technique in three different experiments employing Kr and Au beams. The parameters for each beam are given in table 4.2. In all three cases, the first layer of the target in which the beam is stopped was made of Al, Cu, Fe and Pb in order to evaluate the dependence of the shock strength on the absorber material.

For the Kr beam experiment the target configuration was the one shown in figure 4.11(a). One particularity of these targets was the distance between the stopping point in the absorbent and the interface with the plexiglass layer. The reason for the additional distances was to avoid the penetration of the plexiglass by the ion beam which is a critical issue in obtaining cold compression. The penetration could occur due to the change of the ion beam stopping range during the heating process which was observed both theoretically and empirically. Information about the target dimensions and properties of the materials used are given in table 4.3. A streak camera and a 2D fast shutter camera (PCO DICAM PRO) were used for detection,and both were aligned on the beam axis and focused on the target for gaining space resolution. The slit of the streak camera determined a time resolution of 200 ns. Several cylindrical wires, with diameters between 0.8 and 1.6 mm, were placed perpendicularly to the expected deflections in order to determine maximum deflection angles. The 1.6 mm beam stop was still passed by the deflected light leading to the conclusion that, for all types of targets the angular displacements are larger than 0.8

material	$\rho\ [g/cm^3]$	$c_s[km/s]$	$r_{stopping}\ [mm]$	$r\ [mm]$	$T_{melting}[^\circ C]$
Al	2.70	5.20	16.30	18.00	660
Cu	8.96	3.95	5.79	6.50	1083
Fe	7.87	5.00	6.29	7.00	1535
Pb	11.35	1.91	6.07	7.00	327.5
plexiglass	1.19	2.6*	− − −	7.00	− − −

Table 4.3: Properties of the materials used in the layered targets.

mrad according to the relation $d = f \cdot \alpha$, where d is the displacement, f is the focal length of the last focusing lens and α is the angular displacement in radians. The recorded streak pictures displayed the changes in time of the plexiglass density caused by the shock waves crossing the plexiglass layer, on the ion beam axis. For all targets, a multiple shock wave structure was present for long time. The first wave appeared in plexiglass very soon after the beam was stopped in the absorbent and in some pictures it is visible its reverberation on the boundary with the Al confiner.

According to TRIM calculations the calculated stopping range in the target with a Pb absorbent - shown as a dotted line in figure 4.13, was situated about 1 mm away from the absorber-plexiglass boundary. The origin of time represents the moment when the 700 ns beam pulse arrives in the lead absorbent. According to the schlieren streak picture 4.13 (a), the first shock wave can be observed around 600 ns after the beam is stopped in the Bragg peak region and it propagates in the plexiglass with an averaged velocity of 3 km/s. A changing slope was noticed in the picture, corresponding to a decrease in velocity from 3.28 km/s to 1.87 km/s. Around 900 ns later, before the reflection of the first shock on the boundary with the next Al layer occurs, a second shock wave propagating with a slightly higher velocity of 3.15 km/s arrives in the plexiglass. Figure (b) shows the same target at another shot. The first shock arrives at the same moment as in figure (a), but its average velocity is higher, 3.3 km/s. This can be explained by an increase in the ion beam pulse intensity. A second shock arrives around 1.5 μs later propagating with a similar velocity. The increased brightness of the second shock signalizes a larger density gradient present in the material at this moment compared to the situation at the arrival of the first shock. Together with the reverberating waves propagating during the recorded 6.5 μs , deformations of the boundaries were observed, as the plexiglass, which is a very elastic material, was compressed or relaxed under the action of the incoming shocks. This is the reason for which some of the bright stripes in the picture seem to exceed with up to 0.5 mm the limits of the plexiglass block, represented by the two dashed lines. The pressure in the plexiglass, risen due to the shock wave compression of the material, was not directly measured in this experiment. Estimations of the pressure values were done by using empirical data from literature [Bao84], obtained for the same velocity ranges as in this case. Figure 4.12 shows the dependence of the pressure on the shock velocity through plexiglass. For the target discussed above a pressure of 0.40 GPa was found. The same general features were observed for the other composed targets, with small differences in the time history of the multiple shock waves and their propagation velocities in plexiglass. For different materials, the specific energy deposition of the ion beam differs, leading to particularities in the hydrodynamics of each absorbent. Slightly lower time intervals between the shock waves arriving in the plexiglass layer were found in the case of iron and aluminum than for the copper and lead targets. In the Cu absorbent the Bragg peak

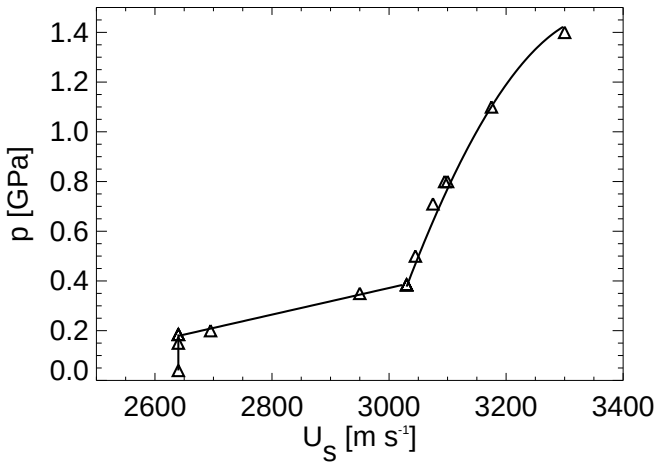

Figure 4.12: Pressure versus shock velocity, measured by [Bao84] in plexiglass. The shock velocities were measured by applying a schlieren technique and the corresponding pressures by using carbon pressure gauges.

was situated 0.7 mm away from the interface with the plexiglass, as calculated with the TRIM code. The first wave is observed around 300 ns after the beam is stopped and had an average velocity of 2.88 km/s. The second wave, with an average propagation velocity of 2.95 km/s arrives 1.4 μs later. In the case of the Fe target the first shock wave was observed in the plexiglass earlier and between the multiple waves a more constant time interval of around 1 μs was measured. The Bragg peak was situated 0.7 mm away from the interface and the average velocity measured was 3.20 km/s for the first shock and 3 km/s for the second shock. A higher velocity, around 3.5 km/s was measured for the Al target. The delay of the first shock was of 800 ns and the Bragg peak was located 1.7 mm away from the interface. The corresponding pressure found was above 1.4 GPa, as the graphic 4.12 shows.

The measured parameters and the delays of the first shocks in plexiglass for each absorbent are tabulated below (table 4.4), followed by examples of streak experimental pictures obtained with the described schlieren set-up.

absorbent	$\bar{v}[km/s]$	$P[GPa]$	$t[\mu s]$
Al	3.50	> 1.40	0.80
Cu	2.88	0.30	0.30
Fe	3.20	1.19	0.00
Pb	3.00	0.37	0.30

Table 4.4: Measured velocities and the corresponding pressures, together with the delays for the first shock arrival in plexiglass for each absorber material .

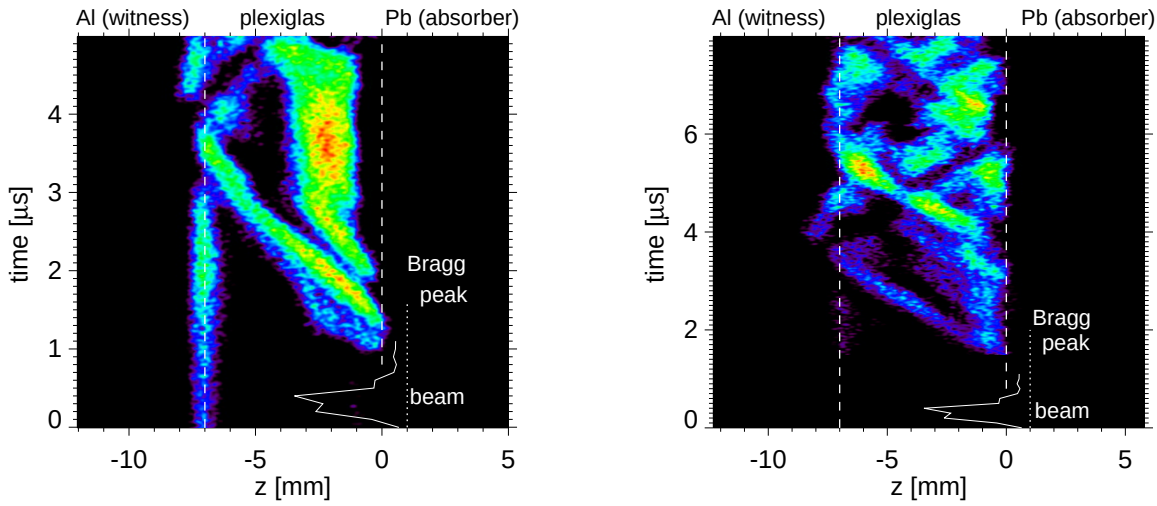

(a) (b)

Figure 4.13: Multiple pressure waves induced by a Kr ion beam in a Pb-plexiglass-Al target. The calculated stopping range was 0.9 mm away from the interface with the plexiglass layer. The beam comes from the right-hand side of the target and it is stopped in the Bragg peak region (dotted line). a) first shot; b) same target, second shot.

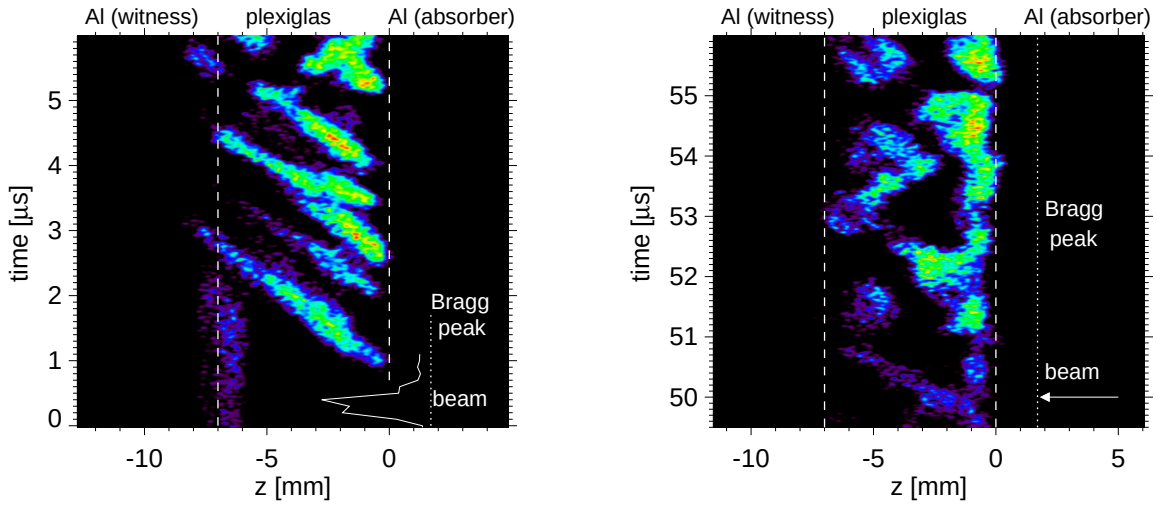

(a) (b)

Figure 4.14: Schlieren pictures of the weak shock waves induced by a Kr ion beam in an Al-plexiglass-Al target. a) first shot, immediately after the beam pulse; b) same target, second shot, around $50\mu s$ later. The Bragg peak was situated 1.7 mm away from the absorbent-plexiglass boundary.

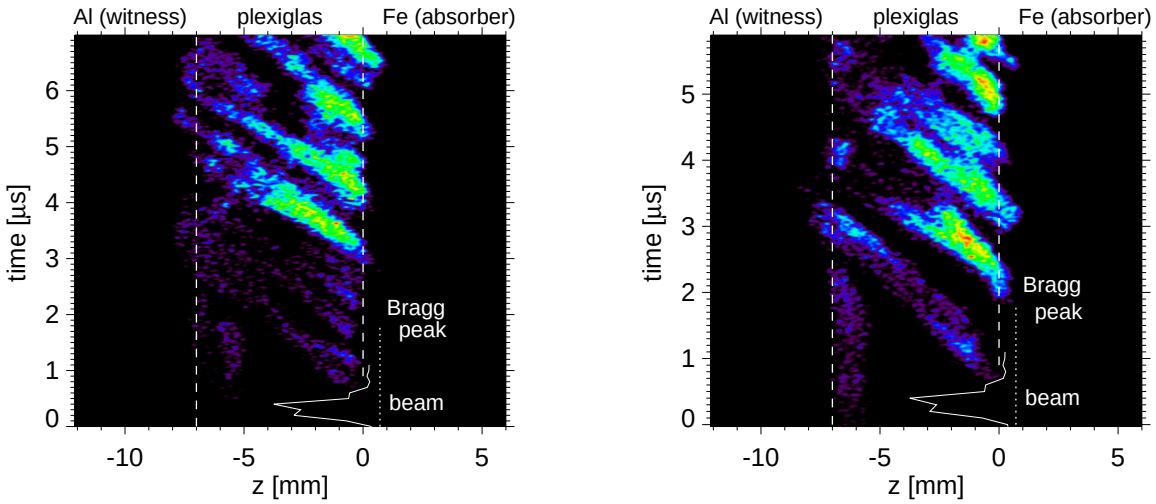

(a) (b)

Figure 4.15: Kr ion beam in a Fe-plexiglass-Al target. a) first shot; b) same target, second shot. The Bragg peak region was 0.7 mm away from the interface.

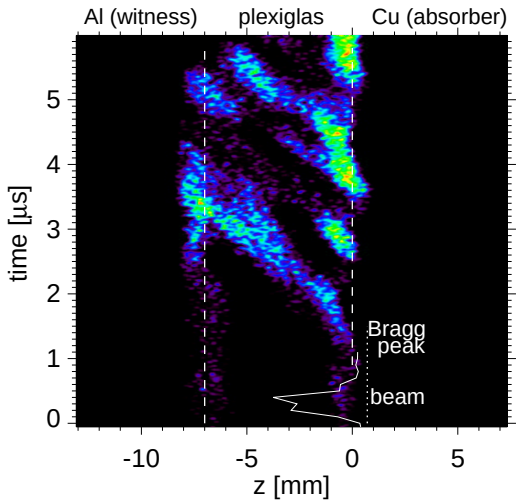

Figure 4.16: Kr ion beam in a Cu-plexiglass-Al target. The ion beam is stopped in the Bragg peak region, around 0.7 mm away from the interface between absorbent and plexiglass.

For the measurements of the hydrodynamical response of the matter heated by a Au beam (table 4.2), the target configuration shown in figure 4.11(b) was used. The absorber materials were the same as in the previously described experiment, followed by a plexiglass block of 15 mm length. The ranges of the absorbents are tabulated below (table 4.5). A larger plexiglass block than in the Kr beam experiment, surrounding the

material	$\rho\ [g/cm^3]$	$c_s[km/s]$	$r_{stopping}\ [mm]$	$r\ [mm]$	$T_{melting}[^\circ C]$
Al	2.70	5.20	8.44	10.50	660
Cu	8.96	3.95	3.00	5.00	1083
Fe	7.87	5.00	3.26	5.00	1535
Pb	11.35	1.91	3.15	5.00	327.5
plexiglass	1.19	2.6*	– – –	15.00	– – –
Al(confiner)	– – –	– – –	– – –	3.00	– – –

Table 4.5: Properties of the materials used in the layered targets with the stopping ranges and the final lengths.

absorbent was used to obtain more clear 2D images of the shock front expanding in time. An advanced framing camera (Ultra8 DRS) recording 8 frames simultaneously with a minimum exposure of 150 ns was focused onto the target together with the streak camera. The time resolution of the streak camera was in this experiment of 100 ns, for a streak time of 10 μs. A round beam stop of 1 mm diameter was placed in the focus of a 0.5 m lens to block the undeviated laser light and an interference filter for red light was used in front of the cameras to avoid the detection of undesired light, i.e. the light emitted by the target or the light from the flash lamp used for the backlighting shadowgraphy. The same shock structure displaying multiple waves was recorded in this experiment as well. A comparison of the velocity values for all four metallic absorbents is given in figure 4.17,

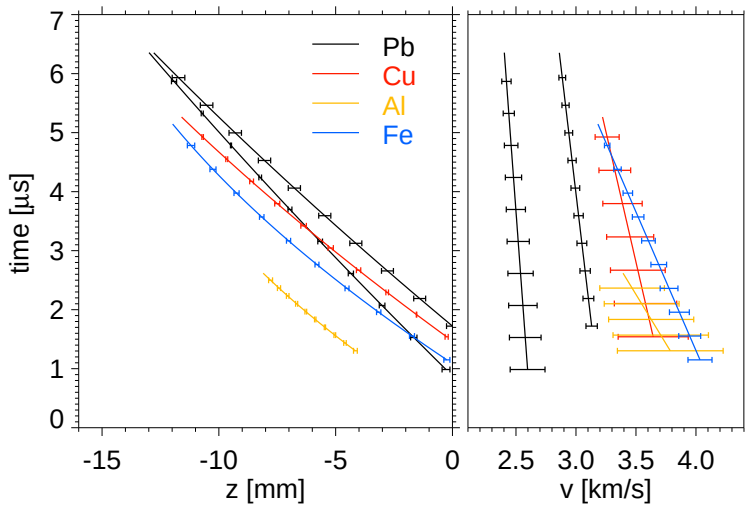

Figure 4.17: Comparison of shock wave propagation velocities in the plexiglass layer of targets with different absorbents: Al, Cu, Fe and Pb, in the experiment with Au ion beam.

where the temporal shock propagation in plexiglass is plotted. The graph shows that the

velocity of the first shock decreases in time, more pronounced for Al and Fe than for Cu and Pb. The secondary waves velocities could not be measured with high accuracy, due to their low level of intensity, as it can be noticed from the experimental pictures (figures 4.18, 4.19, 4.20). The pressures were estimated based on the empirical data measured for

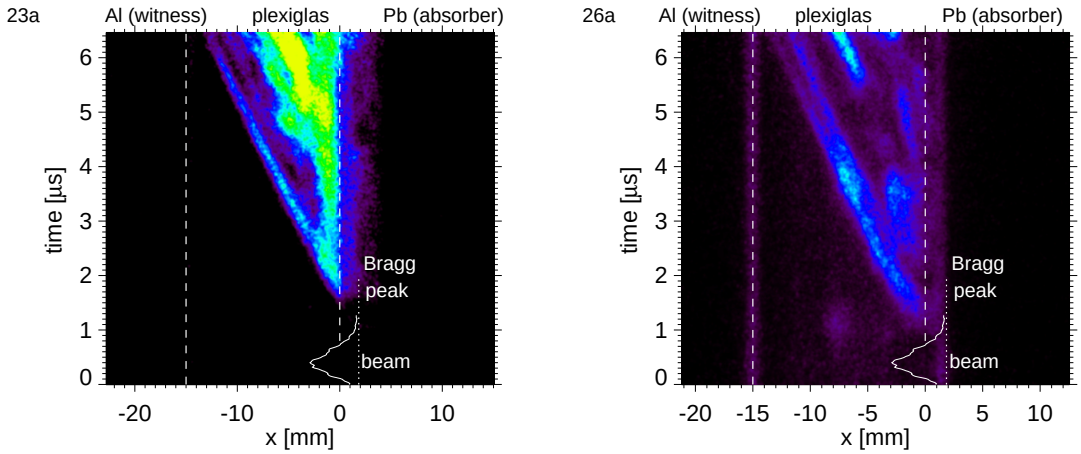

(a) (b)

Figure 4.18: Schlieren pictures of induced shock waves in two different Pb-plexiglass-Al targets: a) focused beam; (b) unfocused beam; the first two bright stripes belong to the same shock denoting the positive slope of the gradient and the negative one. The temporal ion beam profile is plotted on the picture together with the location of the calculated stopping range (dotted line).

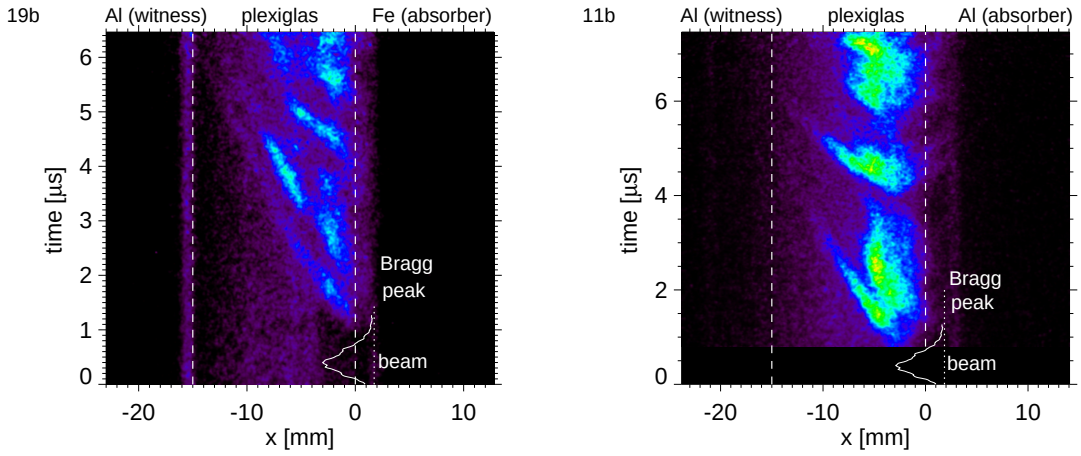

(a) (b)

Figure 4.19: Schlieren pictures of induced shock waves in: a) Fe-plexiglass-Al target; b) Al-plexiglass-Al target.

this shock velocity range from [Bao84], figure 4.12. The highest velocities were measured for the targets with Fe and Al absorbents corresponding to pressures higher than 1.4 GPa.

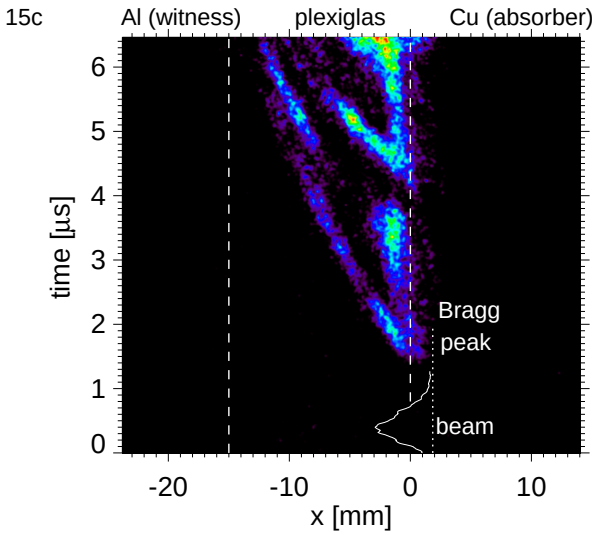

Figure 4.20: Schlieren pictures of induced shock waves in a Cu-plexiglass-Al target.

For the Pb-plexiglass-Al target two different results were found for two distinct targets, at first shots: 1.18 GPa and 0.19 GPa. The difference is explained in this case by a variation in the ion beam intensity, since in one of the shots the beam was not focused. In the case of the other materials the results were consistent for a constant ion beam intensity. The velocity values of the first shock wave measured for all four types of targets are given below (4.6). From the 2D images obtained with the framing camera, general

absorbent	$v_{max}[km/s]$	$P[GPa]$	$t[\mu s]$
Al	3.80	> 1.40	0.05
Cu	3.50	> 1.40	0.80
Fe	4.00	> 1.40	0.30
Pb (focused beam)	3.20	1.19	0.70
Pb(unfocused beam)	2.67	0.19	0.30

Table 4.6: Measured velocities, pressures and delays for the first shock arrival in plexiglass for each absorber material. The differences in the shock arrival is due to different distances to the Bragg peak and its eventual shift.

informations about the shape and temporal expansion of the shock front crossing the plexiglass were gathered, helping in understanding the dynamics of the shocks displayed by the streaked schlieren pictures. Figure 4.21 is an exemplification of a 2D schlieren picture, recorded during a shot in a target composed from a Pb absorbent surrounded on all sides by the plexiglass layer, so that the expansion of the shock can be observed in both longitudinal and transversal directions. The beam enters the target from the left and is stopped inside the lead block. The time for each frame in μs is given below each image, representing the delay after the beam was stopped in the absorbent. The spherical front of the wave propagating in plexiglass 140 ns after the beam was stopped in the Pb absorbent is visualized. From the frames at later times the multiple shock fronts can be spatially resolved. It also results that the waves propagating in the longitudinal direction are stronger than those in the transverse direction. They develop earlier due to

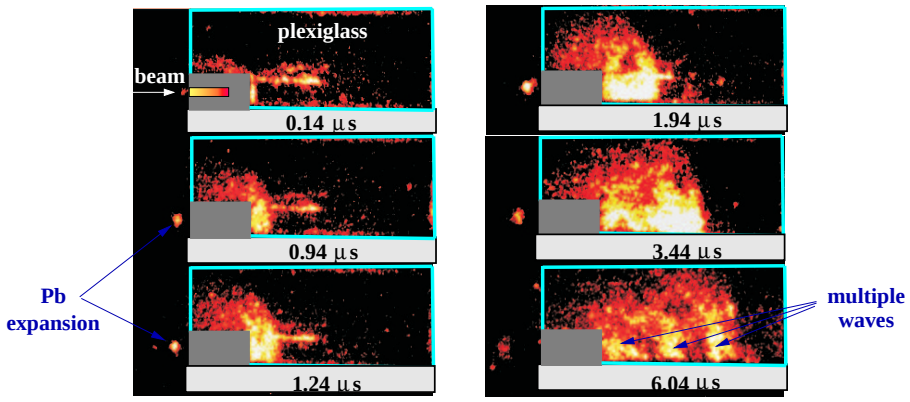

Figure 4.21: 2D schlieren picture of a Pb-plexiglass target irradiated by a gold ion beam.

a smaller distance from the Bragg region to the interface with the plexiglass. In front of the lead block, there are bright spots signalizing the jets of expanding matter. Since at these times the matter is dense, the laser light is blocked and penetrates only through the rarefied edges. Measuring the spot displacement, it results an approximated velocity of the expanding matter of 150 km/s, which is lower than the shock velocity, around 3.125 km/s. This value is almost as high as the velocity measured from the schlieren streak images, for the same material and shot.

4.3 Numerical simulations and theoretical analysis of the schlieren experiment

Since the schlieren method works only for a transparent medium no information about the state of matter in the absorbent could be extracted experimentally. Therefore a theoretical simulation was required, on one hand to compare the measured results with the calculated data, and on the other hand to get information about the target section directly heated by the ion beam. An important outcome of the simulation is the ion beam energy deposition and the verification of the EOS.

The simulations were carried out using a one-temperature, 2D hydrodynamic code, BIG2 [For96] which is based on a Godunov-type numerical method. It uses a rectangular, curvilinear grid and can treat problems of complex target geometries. The electron thermal conductivity is included, although under the physical conditions encountered in the experiment the thermal conductivity does not play an important role. Also the beam energy deposited is included by taking into account the beam geometry. The code was developed in Chernogolovka (at the Institute of Chemical Physics RAS-Chernogolovka, Russia) and later modified at GSI.

Theoretical calculations were performed for the interaction of the Kr ion beam with multilayered targets composed of three absorber materials (Cu, Fe and Pb) followed by the plexiglass layer and the Al confiner. The experimental conditions, regarding the target geometry, the beam geometry, focal spot size and parameters were carefully introduced as input parameters. A semi-empirical, wide range EOS from Chernogolovka [Lom94] was used, and also the SESAME EOS data tables. A good agreement was found by using the former, therefore the results presented here and tabulated in Table 4.7 refer only to those calculations.

$absorber$	$v_{plexi}[km/s]$	$P_{plexi}[GPa]$	$T_{metal}[K]$	$P_{metal}[GPa]$
Cu	2.80	0.21	3468	3.5
Fe	2.70	0.15	2900	3.0
Pb	2.87	0.45	7380	7.1

Table 4.7: The calculated parameters for three layered targets, using the BIG2 code.

Figure 4.22 illustrates the evolution of a pressure front as simulated by BIG2, starting with the time when the shock enters the plexiglass layer, around 0.5 μs. The origin of time was considered to be the time when the first ions enter the absorber layer, while in the experimental pictures the peak of the beam in the absorbent set the time 0. The x axis represents the beam axis and the y axis is the radial position. The beam enters the target from the right-hand side, as indicated by the arrow in the first frame. The pictures map the densities induced only in the plexiglass layer and Al confiner, although the Cu absorbent was also added for a more clear understanding. In the third picture at 1.8 μs, the presence of a second compression wave is observed, and from the density scale it can be deduced that the two waves are comparable. At later times, when the first wave reaches the top free surface of the plexiglass layer, a rarefaction occurs and the second waves attenuates. Proceeding in time, as the rarefaction crosses the material, simultaneously with a reflection on the boundary with the Al confiner and an incoming compression wave (see the last frame, at 4.6 μs, right-hand side of the picture), the interpretation becomes more and more difficult. The density distribution of the compressed matter is

not uniform, except for a small region on the beam axis x visible in the last frame, where the matter undergoes a high compression, possible caused by the wave collision. At this point the code stops, so further information is not provided. However, for understanding of the main processes it is believed that this are the times of highest interest.

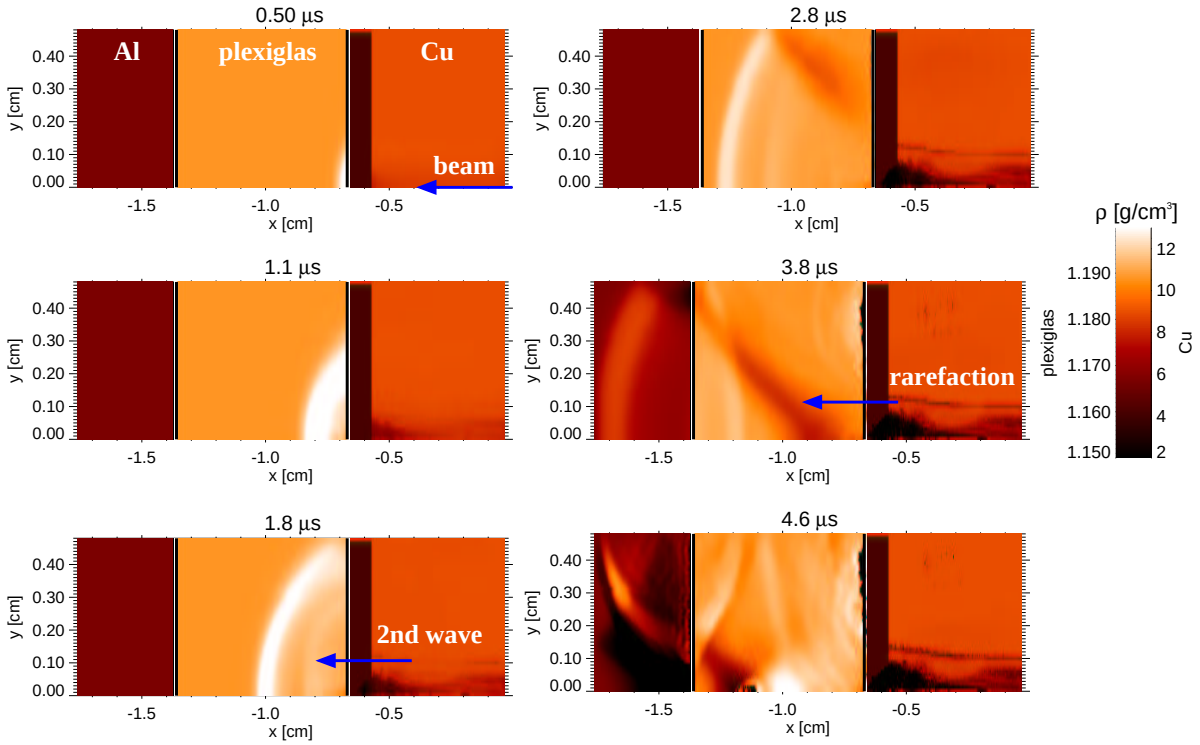

Figure 4.22: Sequence of 2D frames at different times, extracted from the BIG2 simulations, showing the evolution of a pressure wave in plexiglass. The Kr ion beam was stopped in a Cu absorbent. On the right-hand side of the picture a density level scale is attached.

The temporal profiles of the density in the plexiglass calculated by BIG2 are shown in the figures 4.23, 4.24, and 4.25 at some selected times, for targets with three different absorber materials. They inform about the maximum density values, attained when the waves enter the plexiglass layer and give the spatial structure of the stress in the probe. Due to the viscoelasticity of the material, their peaks attenuate in time up to the initial density of the plexiglass (1.19 g/cm^3). The negative density curves are explained by the rarefactions which accompany the compressive front of a spherical shock. At the very last time a reflection on the boundary with the next layer turns back. The maximum density of the compressed material, as demonstrated by these profiles, are achieved in the target containing a Pb absorbent in front of the plexiglass section.

To outline the concordance between the experimental data and the theoretical calculations, the density curves were further used in the reconstruction of the schlieren picture as recorded by the streak camera (figure 4.26). Yet another reason was that an absolute derivation of the plexiglass density profiles from the intensity distribution measured by schlieren diagnostics proved to be extremely difficult. The 'way-back' approach starts from known (calculated) densities and returns the deflection angles and thus the intensity distribution which then is plotted and results in an image resembling the schlieren experimental picture. In this process the ray equation 4.5 and the Clausius-Mosotti relation

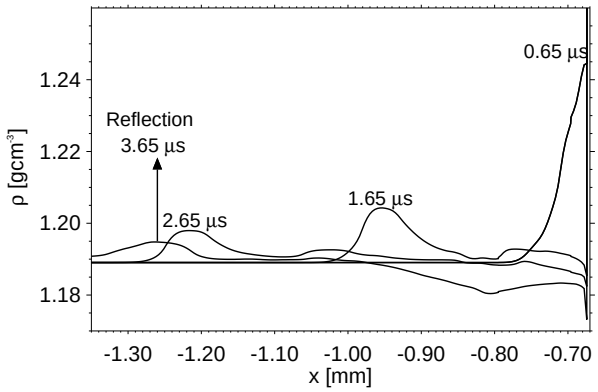

Figure 4.23: Spatial density profiles at different times, in plexiglass, calculated for a Cu-plexiglass-Al target.

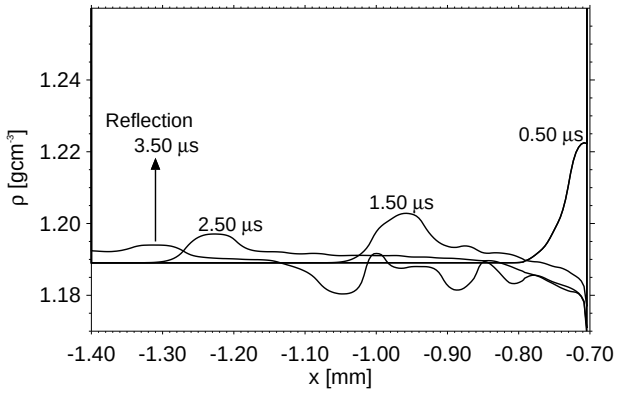

Figure 4.24: Spatial density profiles at different times, in plexiglass, calculated for a Fe-plexiglass-Al target.

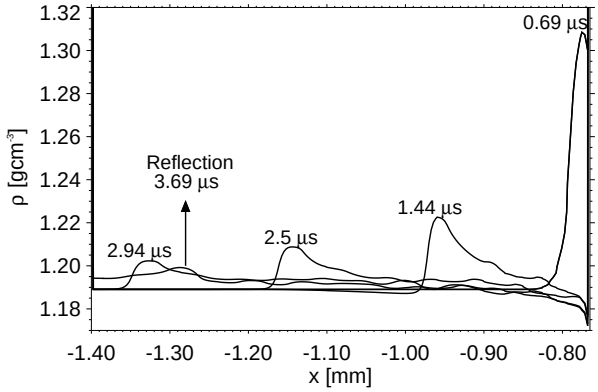

Figure 4.25: Spatial density profiles at different times, in plexiglass, calculated for a Pb-plexiglass-Al target.

4.8 were used. In this case the equation was solved numerically by integrating along the line of sight of a ray, for all rays illuminating the entire plexiglass block. As a simplification, it was assumed that within the plexiglass the displacement of the ray due to the

deflection effect of the refractive gradients is so small that the path can be approximated by a straight line. This assumption is justified, since an overall deflection of 10 mrad (which represent in fact a large deflection) would displace the laser rays in a 10 mm wide plexiglass only by 100 μm, a range along which the change of refractive index gradient is insignificant. For the integration, the density distribution in the Lagrangian grid from the code was transformed into a Cartesian coordinate system. The gradient perpendicular to the laser ray was calculated numerically by a 3-point, Lagrangian interpolation method [Pre92]. Solving numerically the integral, the deflection angles were finally obtained for the [x,z] position of the ray. The simulated schlieren picture renders an increased sensitivity to the presence of a second wave emerging from the absorbent-plexiglass boundary. The reflection is visible as well as the transmitted way in the Al confiner. The times of the wave arrival in plexiglass are slightly shifted in comparison with the experimental ones, due to a different consideration of the time origin (of around 0.35 μs). The angle values on which the simulated picture construction was based were in the order of 10 mrad, higher than the schlieren set-up lower sensitivity. The good agreement in the case

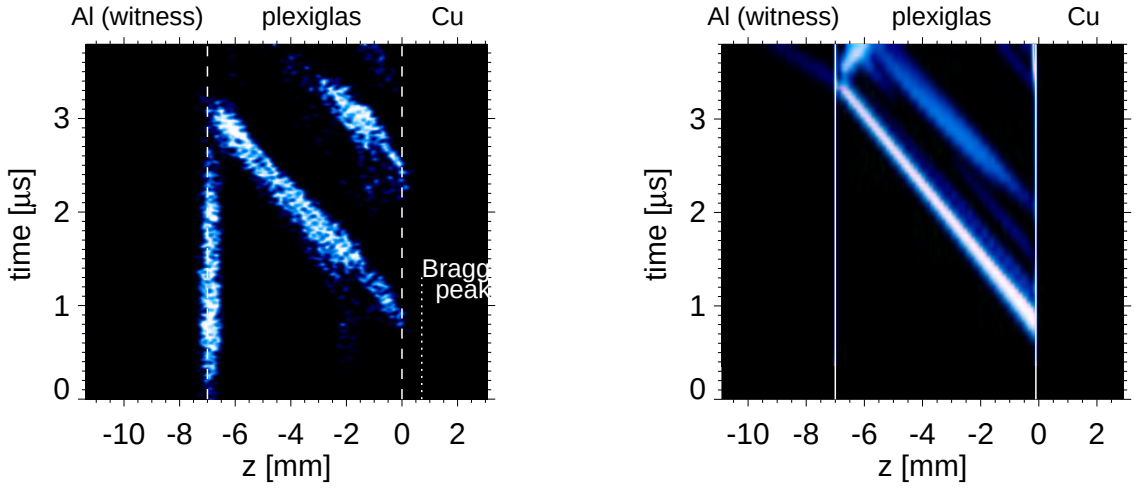

(a) (b)

Figure 4.26: Experimental and simulated schlieren pictures of a Cu-plexiglass-Al target displaying two pressure waves emerging from the Cu layer interface with the plexiglass. The experimental recording was obtained by a streak camera with a time resolution of 200 ns.

of Cu-plexiglass-AL target can be noticed not only from the similarity between the two pictures shown in figure 4.26, but also by comparing the experimentally obtained and the calculated parameters of the matter in plexiglass from the table 4.4 (schlieren section) and 4.7 respectively. For the target with a Pb absorbent the shock velocity and pressure values measured experimentally are close to those calculated. Only in the third simulation, for Fe-plexiglass-Al target there is disagreement, since the velocity measured experimentally is higher than the calculated one. The dimensions and design of the targets discussed here are described in the previous section about the schlieren measurements.

4.4 Imaging interferometry

4.4.1 Fundamentals

Although schlieren is a method which renders a good visual inspection in the refractive behavior of the compressible field of the target, more appropriate quantitative evaluations by means of densitometry are provided by an interferometric technique. A refractive disturbance in the shock wave 'flow' field affects the optical phase of a light beam probing this field, without other changes in its intensity or amplitude. If a two-beam interferometer is used, the phase difference between a transmitted ray through the test field and its unperturbed conjugate ray originating from the same incident parallel beam is measured. The two conjugate rays with a spatial separation d between them will coincide after passing through the test field; if the optical coherence condition is fulfilled, they will interfere and produce a certain interference pattern. A distortion of this well-defined fringe pattern is caused by any difference in optical path length Δl between the two rays traversing the field under investigation in a plane z = const., at positions $x + d/2$ and $x - d/2$:

$$\Delta l = \int_{y_1'}^{y_2'} n(x + d/2, y, z)dy - \int_{y_1''}^{y_2''} n(x - d/2, y, z)dy \tag{4.9}$$

Bright interference fringes appear in the recording plane, where $\Delta l/\lambda = 0, \pm 1, \pm 2, ...$ With the aid of Clausius-Mosotti formula (equation 4.8), the observed fringe pattern is then related to the density variations. Sensitive to the absolute changes of density are the interferometers from the reference beam class, in which the separation d between the conjugate rays is considerably large, so that one of the rays travels outside the phase object and remains permanently unperturbed. Among these systems, the Mach-Zehnder type is well known and generally used to detect small changes of the index of refraction. In the case of a density change caused by a spherical shock wave propagating along x axis in the test field, such an interferometer would detect a fringe shift corresponding to

$$\Delta l/\lambda = \frac{1}{\lambda} \cdot \int_{y_1'}^{y2'} [n(x, y, z) - n_0]dy \tag{4.10}$$

where n is the refractive index of the shock flow facility, y is the axis along which the test light beam propagates and n_0 is the reference refractive index of the unperturbed plexiglass. For a two-dimensional density field with a constant width of $\Delta y = \int_{y_1'}^{y2'} dy$ and after applying Clausius-Mosotti formula 4.8, the fringe shift becomes:

$$\Delta l/\lambda = \frac{1}{\lambda} \cdot \Delta y \cdot \left[\left(\frac{2K\rho(x, z) + 1}{1 - K\rho(x, y)} \right)^{1/2} - \left(\frac{2K\rho_0(x, z) + 1}{1 - K\rho_0(x, y)} \right)^{1/2} \right] \tag{4.11}$$

with the constant K previously defined in the section 4.2.

4.4.2 Beam parameters and interferometry set-up

The heavy ion beams employed in the two interferometric measurements were:

- a $^{197}Au^{65+}$ beam, with 300 AMeV particle energy and an average number of particles of 2×10^9 particles in a 600 ns pulse;
- a $^{238}U^{73+}$ beam, with 300 AMeV particle energy, one bunch of maximum 1×10^9 particles and 600 ns pulse duration.

In both cases, the targets were configured as in the previous experiments (see figure 4.11(a)). The optical measurements were done in plexiglass, which was surrounded by the same materials as before. The ranges were adjusted to stop the beam completely in the absorbents and to avoid the penetration of the plexiglass. For the experiment with Au ion beam a Michelson interferometer was set as a first attempt of quantitative density measurements, but the accuracy of the fringe distortions was not satisfactory, so that in the next experiment it was replaced by a Mach-Zehnder interferometer. The difference between the two devices is that in the Michelson configuration the light beam probes the test object twice, so that an increased sensitivity is expected. Its simplicity is also an advantage over the Mach-Zehnder device, which requires high quality optics and very stable mechanical frames. Its optical and mechanical tolerances is of the order of a wavelength or below. Schematical layouts of the two interferometers are shown in figure 4.27. A He-Ne laser at 632.8 nm wavelength and of 10 mW power was used as

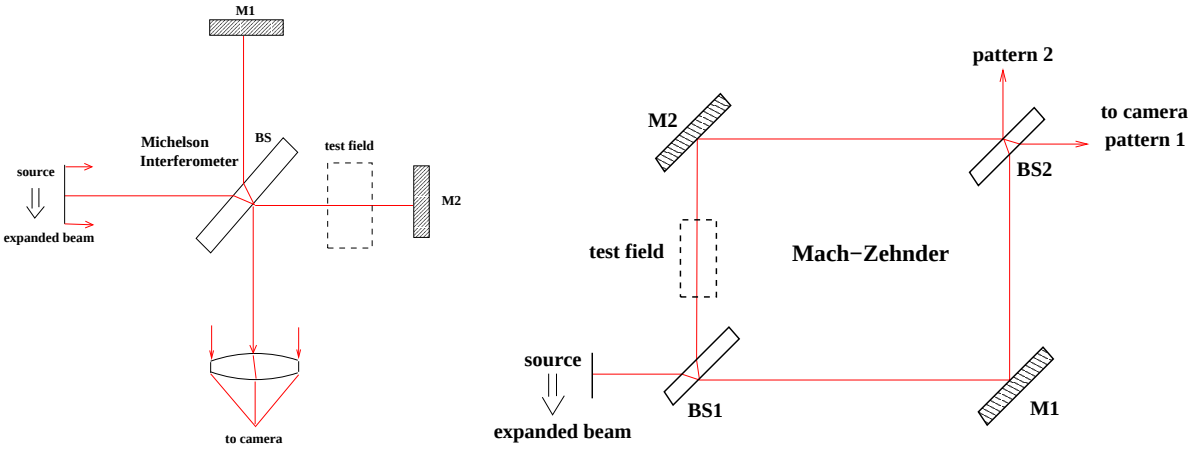

Figure 4.27: a) Michelson interferometer scheme: an expanded parallel beam is splitted by the beam splitter BS; the test beam probes the test field twice; (b) Mach-Zehnder interferometer, with its two mirrors and two beam splitters; the test beam and the reference beam are widely separated one from another. (M is a symbol for mirrors and BS for beam splitter.)

light source in both cases. The laser beam was expanded up to a parallel beam of 30 mm diameter by a telescope. All the optical components used were chosen to have a surface accuracy of $\lambda/10$. Since the laser coherence length is of several meters, the restrictions over the experimental arrangement are not so drastic and a difference of meters in the optical path lengths of the two laser beams is tolerated. However, they were arranged to be equal. In the finite fringe width alignment and uniform test field, the fringe pattern exhibits a system of parallel, equidistant fringes. This can be produced only by inserting a transparent wedge into the path of one of the laser beams or, equivalently, by tilting

one of the mirrors in the set-up. The orientation and number of the fringes in the field of view are determined by the tilting angle. The fringes were oriented along the shock wave propagation direction and their width was changed several times during the experiments until an optimum was reached.

4.4.3 Results

Two-dimensional interferograms, obtained with a Mach-Zehnder device, were recorded by a multiframing camera (ULTRA 68, DRS Headland) which was focused onto the target. An example is shown in figure 4.28. The time resolution was of around 150 ns. The first frame is always showing the null fringe pattern in the absence of any perturbation, serving as reference for the fringe shift evaluation. Measurements of the shock wave propagation velocity in plexiglass were done for targets with Al, Cu, Fe and Pb absorbents, with an accuracy which was limited by the contrast of the interferograms and the thickness of the shock. In some of the cases, the transparency of the material was reduced drastically by the shock passage and further quantitative measurements were difficult. Limited accuracy in the velocity evaluation was determined by the precision of defining the positions of the shock front in plexiglass at different times, for the aforementioned targets. The fringe shift was calculated by a computational program, which was tracing the shifted fringe from the returned centers of Gauss fit curves along the selected fringe and was then relating the shift to the null fringes. In most of the pictures the shock waves were observed arriving in the plexiglass at early times after the beam (the ion beam current peak in the target was considered the absolute origin of time). Likewise the schlieren and deflection diagnostics, the interferometry enabled the visualization of several waves following one another with delays of up to 1 μs or less. Of special interest was the shape of the shock front, which was displayed in the interferograms by the alignment of the fringe shift along the axis perpendicular to the shock direction (indicated in figure 4.28(2)-(4)). In all pictures, at times up to 2 μs the shock front exhibits a large curvature radius, fact which allows the simplification of the density calculation exposed in the introduction of this chapter by introducing the approximation of a plane shock wave front. This approximation is even stronger encouraged in the plexiglass, along the laser path, since the plexiglass thickness was 3 mm. Measurements with pressure gauges which are presented in section 4.6.2 showed that over a range of 3 mm in both longitudinal and transverse directions the changes in pressure are uniformly distributed.

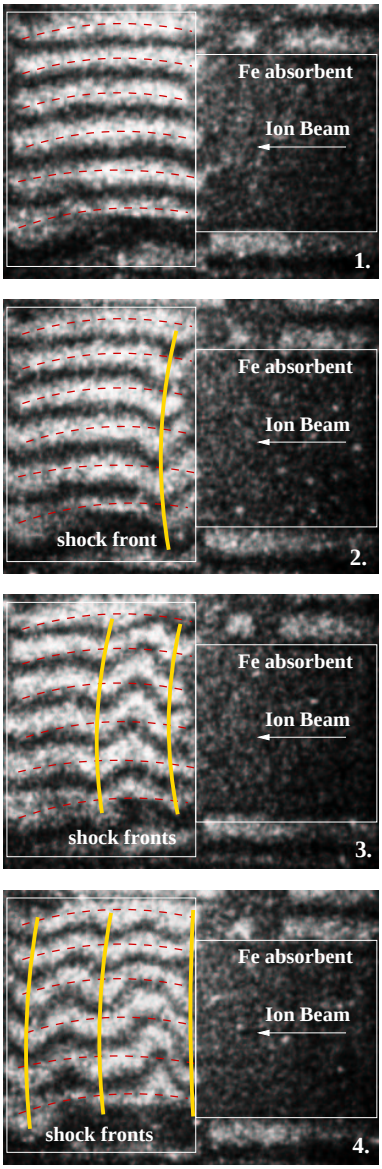

Figure 4.28: (1) Null fringe pattern, $delay = 0\mu s$; (2) $delay = 0.3\mu s$; (3) $delay = 0.7\mu s$; (4) $delay = 1.5\mu s$. All frames have an exposure time of 150 ns.

Figure 4.29 is an example of density profiles in space, measured from frames with

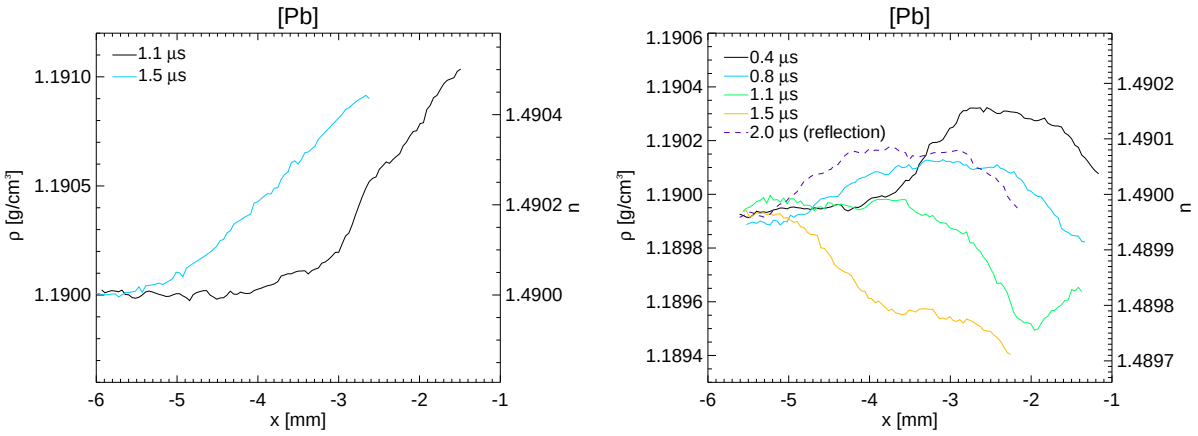

(a) (b)

Figure 4.29: Spatial profiles of density at different times, for two different shots, (a) and (b), in a Pb-plexiglass-Al target. The beam pulse for both shots contained 9×10^8 particles in one bunch.

different delays, for targets containing lead absorbents. The shots (a) and (b) were executed successively in the same target, at different positions, and the ion beam had similar intensities. It can be noticed that for the second shot the compression is much lower. A closer analysis of the target after the shot and the previous experience about the behavior of lead in interaction with the ion beam showed that the material melts and it rarefies especially in the Bragg peak region. The material becomes hollow over a range much larger than the beam diameter and a second shot can be hardly spatially separated from the first. The stress wave generated from the expansion of the left material undergoes therefore a lack of 'strength' which is visible in the very weak compression attained.

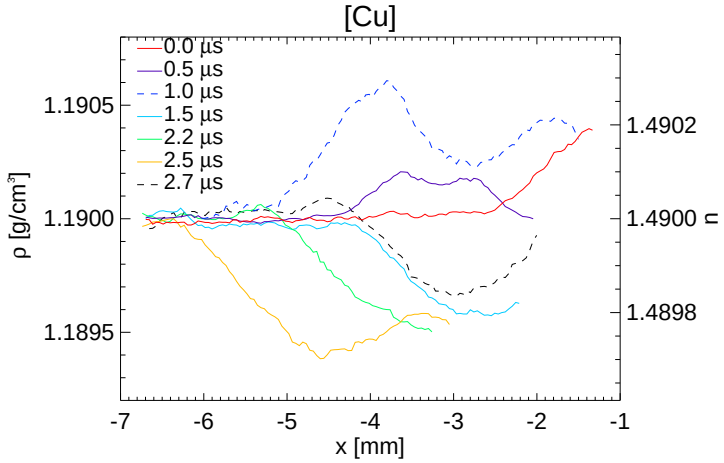

Figure 4.30: Spatial profiles of density at different times, for a shot in a Cu-plexiglass-Al target. The dashed line shows a second wave at 1 μs time after ion beam peak.

The distorted pattern in the interferograms display generally fringe shifts around 1 or smaller. Only in the plexiglass section of a target with lead absorbent the maximum fringe shift reached the value of 2.5. At later times (after 2 μs) the stressed material loses

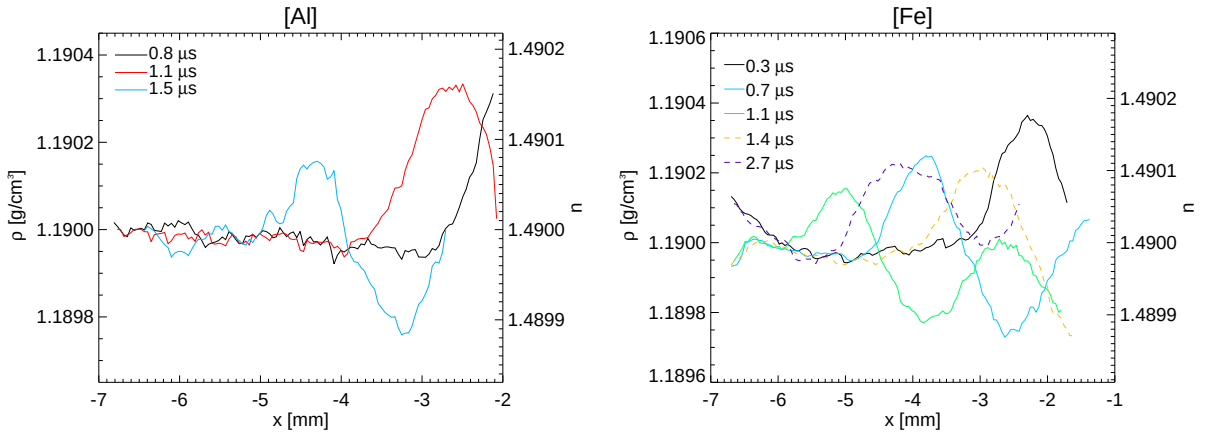

(a) (b)

Figure 4.31: Spatial profiles of density at different times, for a shot in (a) Al-plexiglass-Al and (b) Fe-plexiglass-Al. The dashed lines in (b) represent a second wave observed at 1.4 μs and a reflection at 2.7 μs.

its transparency and the fringe shift measurement fails. This effect can be associated either to a fringe shift exceeding the detection limit determined by the exposure time of the camera or to a damage of the loaded material which becomes dispersive. In both cases the compression ratio would be higher than that observed at earlier times. The shape of the wave profiles and the velocities measured up to these times point towards an acoustical nature of the wave. The spatial profiles are quite wide while the propagation velocities are almost equal to the speed of sound in plexiglass within the error range, which was of $\pm$ 0.2 km/s. The increase in density assumed at later times could be then achieved only due to a pressure enhancement caused by the effects of reverberations on boundaries with the cold confiner and the heated Bragg peak region, and not due to the characteristic strength of a single wave. The wave profiles at different times in the above figures (4.29-4.31) show the presence of a second stress wave or a reflection around 2 μs or less, depending on the target and on the limits of the examined region of plexiglass. They were plotted in the graphics as dotted lines. Also the density maxima achieved can be observed in the same figures.

The measured parameters in all four types of target, such as fringe shift and propagation velocity of the stress wave are summarized in the table 4.8 together with the number of ions in the pulse of the respective shot.

The velocities were obtained from the interferograms by determining the location of the wave front in frames with different delays and same exposures. They proved to be in a good agreement with the values resulting from the comparison between interferometric and laser deflection measurements, as it will be underlined once more in the next section (4.6). In comparison with the schlieren measurements performed during the experiments with Kr and Au ion beams, the pressure waves in this experiment were weaker, with characteristics of acoustic waves demonstrated by the broad density profiles, low pressures and velocities close to the speed of sound. An explanation of this fact is the low power deposition of the U ion beam in the absorbents due to a low number of particles in the pulse.

material	N [$particles/pulse$]	max.shift	v [km/s]
Al	8×10^8	0.8	2.90
Cu	7×10^8	0.8	2.60
Fe	8.4×10^8	0.8	2.85
Pb	6.4×10^8	2.5	2.60

Table 4.8: Interferometric results for all targets, different shots with an U ion beam. The error for the velocity is of ± 0.2 km/s. For the Pb-plexiglass-Al target, the velocity corresponding to the maximum fringe shift could not be measured. In this case the fractional fringe shift for the 2.6 km/s velocity was of 0.8.

4.5 Deflection angle measurements

4.5.1 Principle and set-up

Absolute measurements of the angles under which the probing laser light is deflected by the perturbations in the target can be performed in a simple way. The following part of the work will be dedicated to the description of the method and the results obtained.

As it was already stated in the section 4.2 about the schlieren method, a refractive index gradient induced in the studied material will cause deflection of the probing light under a certain angle which can be related to the density gradients by using equations 4.5 and 4.8. These deflections can be recorded time resolved directly by a streak camera, showing the evolution of the refractive index gradient in time, at one location in the plexiglass. The optical device used for measurements, shown in figure 4.32, consisted of a gated diode laser (635 nm), as light source, sent perpendicularly on a transparent material (plexiglass) and a streak camera placed at a large distance (3.85 m). The laser beam was not expanded for this measurement. The laser spot size inside the plexiglass block was around 0.5 mm which is small compared with the profile of the observed shocks. This assures a good space resolution and prevents from converging and diverging effects caused by wide density gradients, so that the entire laser spot is deflected only in the direction corresponding to the gradient sign. On the streak camera, due to the laser divergence of 0.7 mrad, the laser spot size was of 3 mm, sufficiently small compared with the spatial deflections. Unlike the schlieren device, where the deflections have to be compensated in order to image precisely the target, in the deflection device no lens is used and the laser is aligned directly onto the streak camera slit. The streak camera was operated with a sweep time of 5 μs with a time resolution of 50 ns determined by the camera slit width. For time calibration purposes the laser was pulsed, with a pulse length of 3.8 μs and the delay between the ion beam peak current and the laser pulse was measured on an oscilloscope with a precision better than 100 ns. If the total length from the target to the

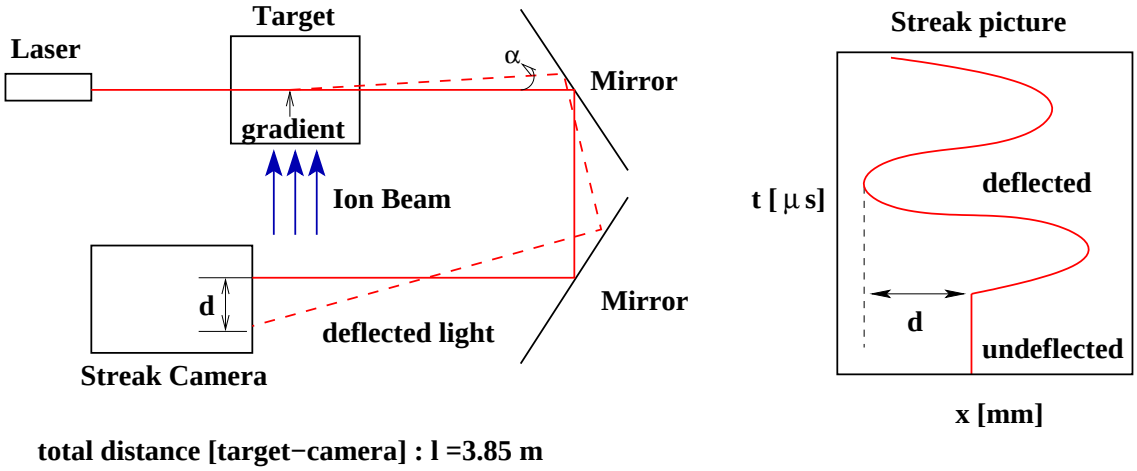

Figure 4.32: Deflection angle measuring device.

detection plane l is known and the streak screen is calibrated in millimeters, the spatial displacement, d, can be easily measured from the pictures and inserted in the relation $d = l \cdot \sin\alpha \approx l \cdot \alpha$ from which the deflection angle α can be calculated and related further to the density gradient.

4.5.2 Experimental results

The method was applied together with the Mach-Zehnder interferometric measurements in the experiment with $^{238}U^{73+}$ ions, bunched in a pulse of 300 ns FWHM and 8×10^8 particles, with a particle energy equal to 300 MeV/nucleon. The same configuration of layered target with metallic absorbents made of Al, Cu, Fe and Pb affixed to a plexiglass block and an Al confiner as in the figure 4.11(a) were utilized. The ranges for each component block of the target are given in table 4.9.

absorbent	$r_{stopping}[mm]$	$r[mm]$	$r_{plexiglass}[mm]$	$x[mm]$
Al	7.60	11	6	4.80
Cu	2.70	6	6	4.90
Fe	2.93	6	6	5.00
Pb	2.84	6	6	3.90

Table 4.9: Ranges of the targets employed in the deflection angle measurements and the laser spot position x in plexiglass.

The laser illuminated the plexiglass at some distance from the boundary and this is the reason for which the oscillations of the laser spot around its initial position (when there is no deflection) are delayed with respect to the shock arrival in plexiglass. These distances are tabulated for each target in table 4.9 (last column) together with the stopping ranges and lengths of each absorbent. When the shock front reaches the position of the laser spot, its deflection occurs towards the shock, where higher gradients are generated, which is in the opposite direction of the ion beam. The back of the shock or a reflection on the boundary between the plexiglass and the Al witness deflects the laser light in the ion beam direction. An experimental streak picture for a shot in a target with an iron absorbent is shown in figure 4.33. A negative displacement d corresponds to a laser deflection opposite to the ion beam direction and to a positive gradient. The dotted lines indicate the beginning and the end of the laser pulse and the vertical solid line represents the position of the laser spot when no

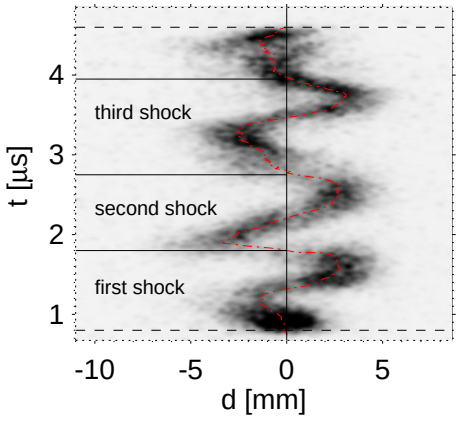

Figure 4.33: Deflections for a Fe-plexiglass-Al target.

gradients are generated. The multiple oscillations of the laser spot in time observed experimentally suggest density changes occurring at time intervals around 1 μs, which show that multiple shocks were present. In this picture, three subsequent shocks are visible; the second shock causes a stronger deflection than the first, fact observed also in the schlieren measurements.

For the evaluation of the deflection angle the displacement was determined by a computer program which calculated the position of a Gauss fit to the laser beam profile, at each time. Due to a limited field of view of the camera, spanned from -10 mm to 4 mm displacement, only angles between 1 mrad and 2.5 mrad could be measured. The eventual reductions of the laser spot intensity in this case are not related to the characteristic strength of the shock, but to the movement of the spot along the streak slit.

In figure 4.34 the displacements in time for the four absorber materials used in front of the plexiglass layer were plotted in order to underline the differences between them. Also collisions between the rarefaction and reflection wave (figure 4.34(a) and (c)) or a reflection and a compression wave (figure 4.34(c), around 3 μs) at the laser spot location are visible. All targets responded similarly to the stress wave load, except for the Pb-plexiglass-target (figure 4.34(d)). A higher deflection of the laser than in the other targets, but at later times, was recorded and the peak exceeded the field of view of the camera. Just as in the interferogram taken for the same shot, an increased stress was present in the plexiglass section, although the propagation velocity of the wave was the same as in the other cases, equal to the speed of sound. The parameter which differs from the other materials is the density and quantity of the expulsed material around the Bragg peak region, which plays an important role, as it was observed in the previous section (comparison between two consequent shots in same conditions, in lead - figure 4.29). An evaluation of the spatial and angular displacements for the four types of targets is summarized in the following:

- for the aluminum absorbent: the laser spot was displaced as much as 6.5 mm away from the initial position in the detection plane, which corresponds to an angle of 1.7 mrad (figure 4.34(a));
- for the iron absorbent: a maximum displacement of 3 mm was measured, yielding an angular displacement of 0.7 mrad (see figure 4.34(b));
- for the copper absorbent: a maximum displacement of 4 mm was measured and an angle of 1 mrad for the first wave and 6 mm, corresponding to 1.6 mrad for the second wave(figure 4.34(c)).
- for the lead absorbent: a maximum displacement of 9 mm for the first wave, corresponding to an angle of 2.3 mrad; for the second one which is much larger, the displacement exceeded the field of view of the camera (figure 4.34(d)).

The plexiglass thickness was of 3 mm which can in this case be considered as a thin layer. To approximate the shock front with a plane front, moving with a constant velocity is consistent with the interferometric observations presented in the previous chapter. Therefore the equation 4.5 simplifies, yielding:

$$\alpha = \frac{1}{n_0} \cdot \frac{dn}{dx} \cdot \Delta y \tag{4.12}$$

where n is the refractive index of plexiglass and Δy = 3 mm is the thickness of the plexiglass crossed by the laser beam. The refractive index changes are very small, so that the changes of the refractive index along this range on y axis will be neglected.

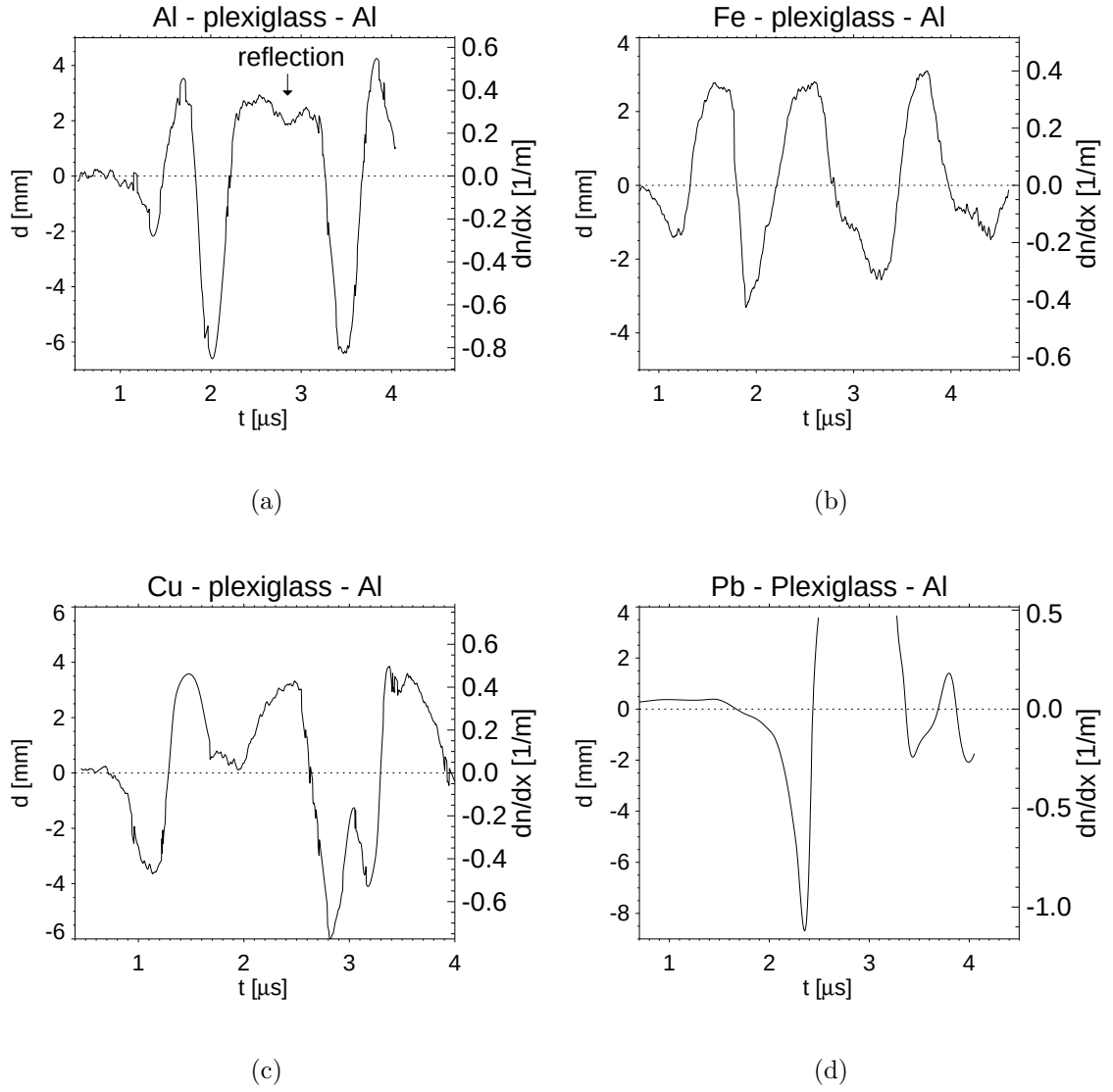

Figure 4.34: Laser spot displacements in time and resulting refractive index gradients measured in plexiglass, for different type of targets (a-d); the negative displacement values correspond to positive gradients induced by the stress waves. The arrow in graph (a) points towards a reflection of a first wave at the rear side of the plexiglass layer.

The profiles of the refractive gradients in time can be further transposed in profiles of refractive index along x, with known velocities from the interferometric measurements. Introducing again the Clausius-Mosotti relation, the density calculated from the approximated refractive index can be obtained and compared with the results from interferometry. Since several approximations were done in these calculations, an absolute value is not the issue here; however, comparing the order of magnitude of the results obtained from two different experimental diagnostics is of great importance.

The density profiles in time and space are plotted in figures 4.35 and 4.36, for targets with different absorbents. The density profiles as resulting from the interferometric measurements were plotted in the same graphic for a direct comparison. Only the results for the first wave were compared, since the situation complicates too much for the following waves which synchronize sometimes with a reflection of the first wave on the boundary

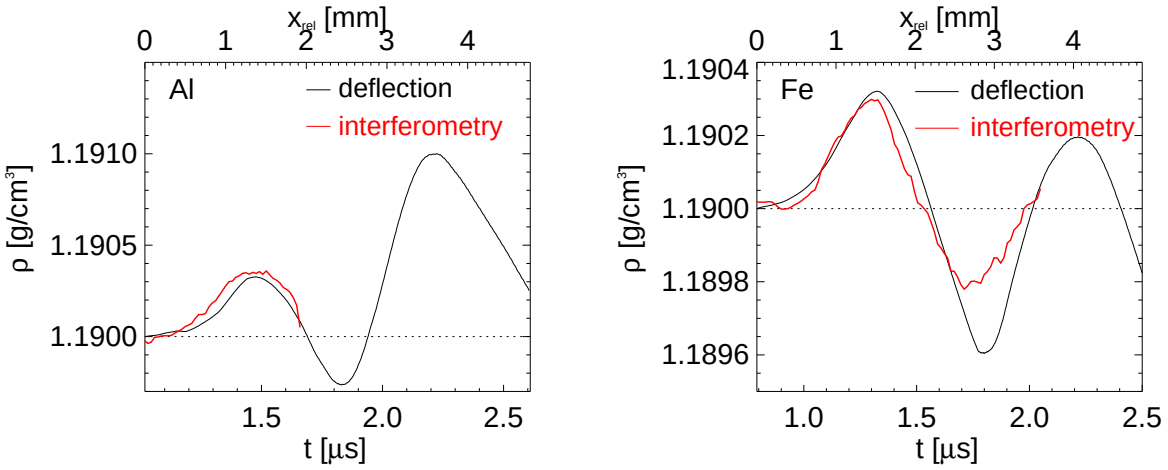

(a) (b)

Figure 4.35: Comparison between the density profiles in time and space as calculated from interferometry and laser deflection for (a) Al-plexiglass-Al and (b) Fe-plexiglass-Al targets. The coordinate x is relative and only the first wave was taken into account for comparison.

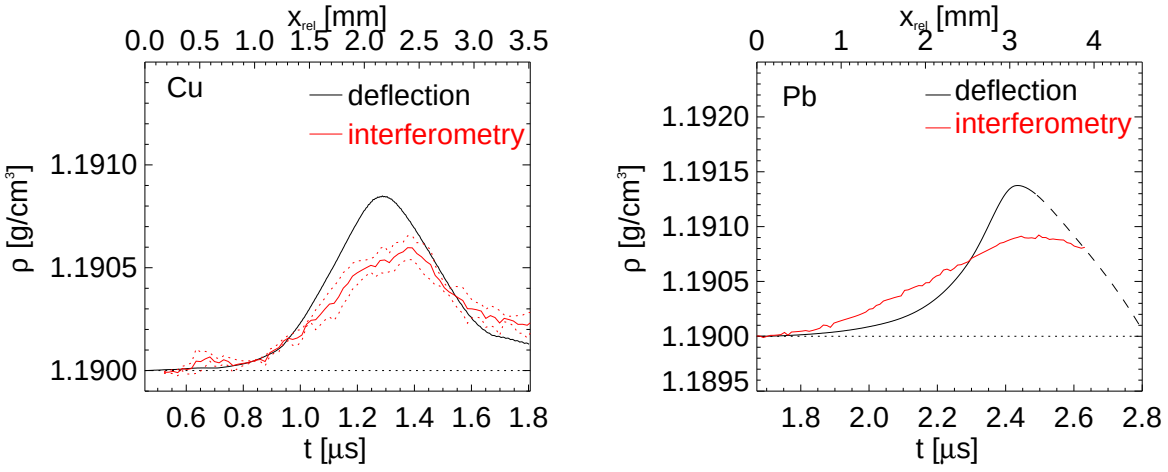

(a) (b)

Figure 4.36: Density profiles obtained from laser deflection measurements for (a) Cu-plexiglass-Al and (b) Pb-plexiglass-Al targets. The dotted lines in (a) show the error range determined by velocity determination in interferometric measurements.

with the Al witness. Aspects like time structure and spatial extent of the wave were in good agreement and they constituted the main benchmarks for the fitting program. In this computational program the velocity of the wave was taken from the interferometric results and used as a translation parameter from the time axis t to the space axis x ($x = v_{shock} \cdot t$, assuming that v_{shock} is constant as long as the wave passes through the laser spot). The gradient as a function of x can be then integrated to obtain the refractive

index and thus the density profile:

$$n(x_{rel} + \text{offset}) = \int_0^{x_{rel}} \frac{dn(x)}{dx} dx. \tag{4.13}$$

The integration was performed numerically, using a five-point Newton-Cotes integration formula [Pre92]. The offset served as a shifting parameter so that the profiles could be superimposed on the interferometric profiles for comparison. This procedure can only be applied at early times, before reflections from the rear side of the plexiglass reach the laser spot. From this time on the deflection is caused by a superposition of gradients moving with positive and negative velocities and a reconstruction of the density profile is not possible. The density curve amplitudes, depending on this parameter, were not always resembling for the two methods, especially in the case of Pb- and Cu-plexiglass targets where the differences are appreciable (figure 4.36). The discrepancy is reasoned by the inaccuracy of the velocity determination for these two shots. In figure 4.36(a) two dotted lines enveloping the interferometric profile show the error bar range, transcended by the laser deflection profile. Even so, the comparison leads to a satisfactory similarity between the outcome of the two methods, fact that grounds the reliability of the results.

Likewise schlieren, the deflection measurement showed that even at very late times (over 60 μs), density gradients comparable in size to those generated at early times are still present.

In future experiments, a better distinction between reflection and rarefaction waves can be obtained by applying the method with two laser beams probing the target at different positions, while the detection is done on the same streak camera.

4.6 Pressure measurements

4.6.1 Principle of the piezo-electric gauges

Pressure measurements coupled with density and wave speed determinations in the uranium beamtime were performed by using piezo-electric pressure gauges. Former experiments with such probes were successfully accomplished at HHT, providing knowledge about time evolution and amplitude of pressure waves induced by heavy ion beams in lead targets [Sto98] and cryogenic crystals [Fun99]. Both studies apply the plane shock wave formalism and the linear relation assumption between pressure and current signal given by the probes, valid for the reported pressure ranges (less than 1 GPa). The same approach is appointed here.

In the center, the transducers contain a film made of polyvinylidene fluoride (PVDF), which is a crystalline polymer with ferro-electrical properties. In a strong alternative electric field PVDF presents a hysteresis loop of the polarization [Bau82]. The preparation process implies bi- or uniaxially stretching of the foil followed by electrical poling at high values of remanent polarization reaching a maximum of 20 to 30 $\mu C/cm^2$. Intensive studies of these sort of transducers showed that they are unusually sensitive to details of stress pulses [Gra87]. More of the PVDF foil properties are described in [Bau85, Ohi76].

A piezo-electric gauge reacts at mechanical tension transforming it into electric charge. If the probe is part of a closed electrical circuit, a pressure wave penetrating the foil will generate a current proportional to the difference of the mechanical tensions σ_1 and σ_2 acting perpendicularly to the two surfaces of the foil:

$$I(t) = \frac{d_{33}Ac}{e}[\sigma_1(t) - \sigma_2(t)], \tag{4.14}$$

where d_{33} is the piezo-electric constant for tension perpendicular to the surface, A is the active area of the sensor, c is the propagation velocity of the stress wave and e is the thickness of the foil. When the wave reaches the foil surface σ_2 equals 0 and the current signal will depend on the rate-of-change of the stress σ_1. During the wave propagation through the foil the current signal follows the increase of the wave with a time resolution of $\Delta t = \frac{e}{c}$, which is the time needed for the wave to cross the foil from one surface to the other. For a wave pulse width greater than Δt, $\sigma_2(t) = \sigma_1(t + \Delta t) = \sigma(t)$. The equation 4.14 becomes

$$I(t) = d_{33}A\frac{d\sigma(t)}{dt} \tag{4.15}$$

The response of the probe depends strongly on its sensitivity S which is usually given in units of Q/F (with F the force acting on the probe surface), hence, independent on the active area A. When the generated charge flows across a resistor R = 50 Ω it results a voltage

$$U(t) = R \cdot \frac{dQ(t)}{dt} = R \cdot S \cdot \frac{dF(t)}{dt} = R \cdot S \cdot A \cdot \frac{d\sigma(t)}{dt}. \tag{4.16}$$

Integrating equation 4.16 from t'= 0 to t, the pressure perpendicular to the foil surface is obtained at the time t:

$$\sigma(t) = \frac{1}{RSA}\int_0^t U(t')dt'. \tag{4.17}$$

Up to 2.5 - 3 GPa pressures, an almost constant proportionality factor between current signal and pressure was found [And90]. Deviations from this linear relation, reported in

[Bau85] depend very much on the gauge parameters, such as foil thickness and polarization.

4.6.2 Experimental results

The pressure sensors were placed between the component plates of the target, either at the front side of the plexiglass block or at the rear side. Only in one case the plexiglass was situated on top of a copper block and the pressure gauge located at the interface between the two materials. This enabled, for few shots, evaluations of the pressures exerted by transversal wave front, for comparison with the longitudinal wave strength. The targets used were as the type described in the interferometry chapter, since the interferometry, laser deflection and pressure measurements were performed simultaneously. The PVDF piezo-electric gauges were provided by the german manufacturer EIC Gmbh. The round shaped sensors, with a diameter of 3 mm have gold deposited electrodes and a thickness of 25 μm. The sensitivity was 27.5 $\pm$ 3 pC/N.

The signals were recorded on an oscilloscope which was connected to the gauge by a 90 m long coaxial cable (RG 58), using an external resistor of 50 Ω. The ion beam current induced always a noise signal of around 1 V which was taken as a time reference (namely, the ion beam current peak). This noise did not disturb much the electrical response of the pressure sensor, since the stress wave reaches the active area of the sensor after a certain traveling time. Also the noise of the plasma lens current was considerably earlier than the stress signal, as it can be noticed for example in figure 4.37. The beam was stopped

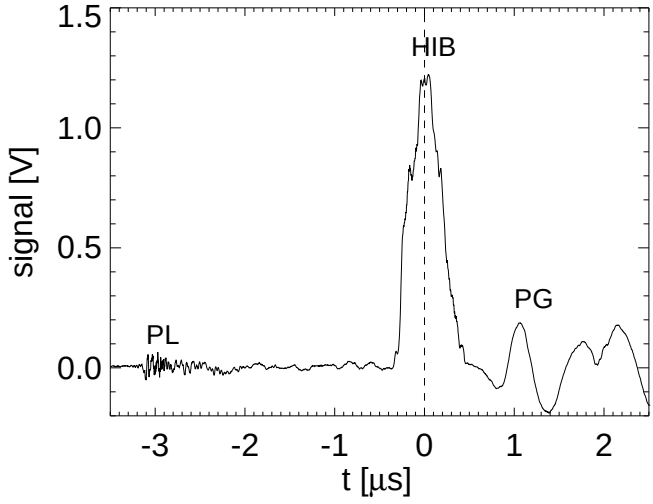

Figure 4.37: The plasma lens current (PL) and ion beam current (HIB), followed by the electrical response of the pressure gauge (PG) in an Al-plexiglass-Al target. The pressure gauge is situated at the interface between the Al absorbent and the plexiglass layer.

in an Al block, just few millimeters away from the pressure gauge, situated in front of the plexiglass layer. The signal was integrated in time and then scaled in pressures by using the relation 4.16. Figure 4.38 shows the time profile and the amplitude of a pressure wave reaching the sensor at around 3 μs after the ion beam peak. It was immediately followed by a second wave with a higher amplitude of around 3 MPa. The signal for a similar

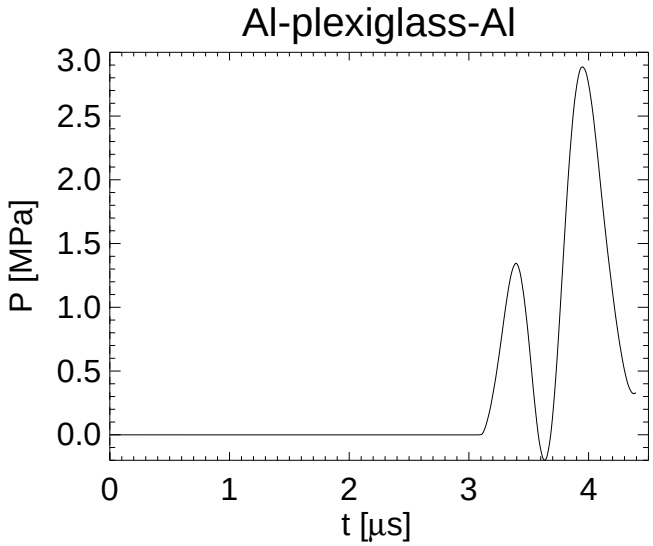

Figure 4.38: Amplitude and temporal behavior of pressure waves in an Al-plexiglass-Al target, obtained by using the signal from a transducer at the rear side of the plexiglass layer of the target. The ion beam pulse had 1×10^9 particles.

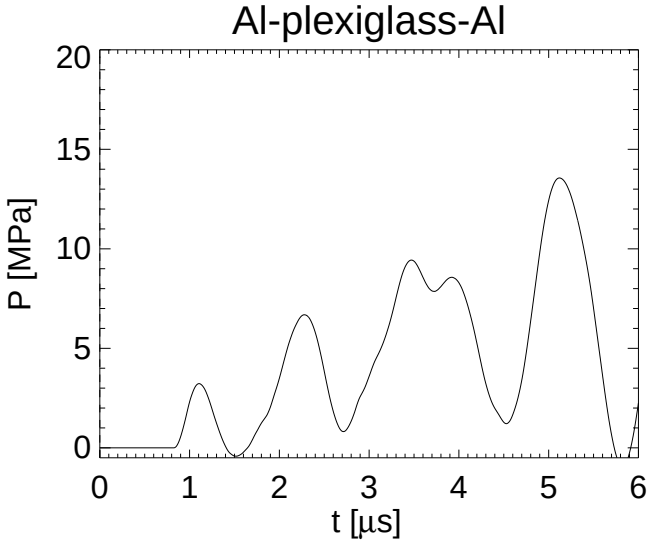

Figure 4.39: Pressure signals recorded during a shot in an Al-plexiglass-Al target, with the transducer in front of the plexiglass layer. The ion beam pulse contained, for this shot, 8×10^8 particles.

target, but having the pressure sensor mounted in front of the plexiglass layer was much higher, reaching pressures of 15 MPa (figure 4.39).

Several shots were executed in the targets at different distances from the center of the pressure gauge, in all directions. The signals showed not only very similar time distribution, but also almost equal amplitudes of the waves, in the case of both measurements, with pressure sensors in front and in the back side of the plexiglass block (figure 4.40). Over some 3 mm the distribution of the pressure proved to be uniform and reproducible from shot to shot. It follows that the stress wave had indeed a large curvature radius,

as it was assumed previously in the density calculations along ranges of 3 mm. In all targets the plexiglass confronted to the multiple wave structure presence which yield an enhancement of pressure peaking at later times, by the time of the second or third wave. Collisions between incoming waves and reflections were visible in some cases, as it can be observed in figure 4.39 around 3.7 μs. The target made of Cu and plexiglass on

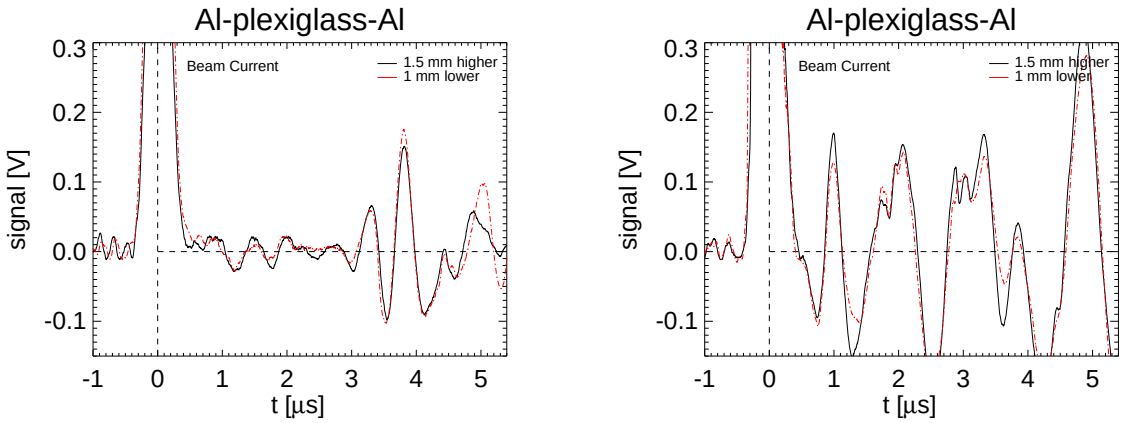

(a) (b)

Figure 4.40: (a) Signals for a target with pressure gauge mounted in front of the plexiglass; (b) signals for a target with pressure gauge mounted in the back of the plexiglass. The shots were executed at different distances from the ion beam axis.

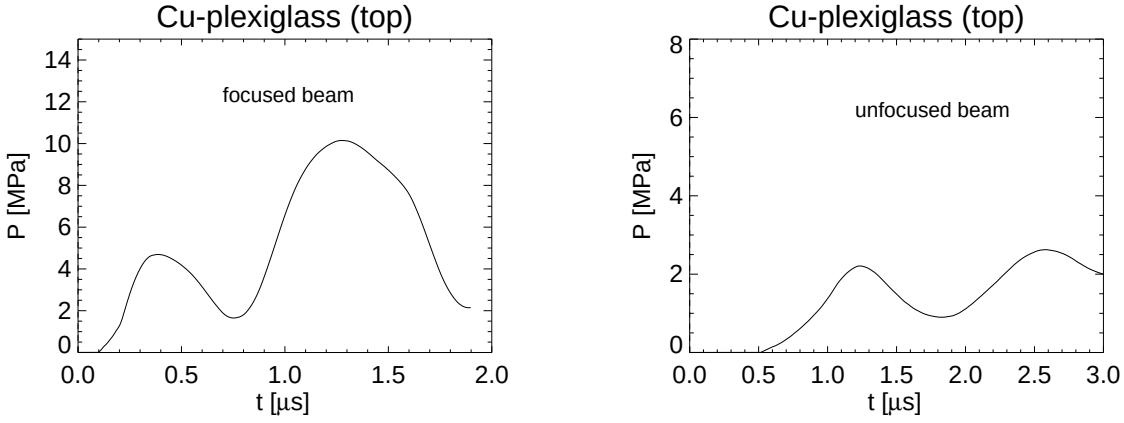

(a) (b)

Figure 4.41: (a) Shot with a focused beam, radial measurement in Cu-plexiglass target; (b) unfocused beam for the same target.

top had no confiner attached and the sensor was located at the interface between the two materials. This was one of the few measurements for radial waves and gave pressure values comparable with those recorded by the the sensors located in front of the plexiglass for longitudinal measurements. The gauge was 2 mm away from the beam axis, on top

of the Bragg peak location. For comparison between pressure amplitudes for different beam intensities, shots with focused ion beam and unfocused ion beam were performed. The difference can be noticed in figure 4.41, in pressure amplitude and wave propagation speed (from a time delay of 0.5 μs for the unfocused beam shot).

A signal depicted from a direct shot in plexiglass, which is shorter than the range of uranium ions, lead to pressure values of around 10 MPa, comparable to the amplitude of the waves generated by the Bragg peak region in the Cu block. The reason of this shot in plexiglass was to get an intuitive understanding of the wave behavior when there is no interface. A more accurate comparison with the case when there is a transit over an interface requires calculations of the power depositions and a precise localization of the Bragg peak. The latter is difficult to achieve for absorber materials such as Cu and Pb where the Bragg peak shift during heating cannot be neglected.

The entire set of data is summarized in table 4.10.

absorbent	$d[mm]$	$N_{beam}[\times 10^8 particles]$	$P_{plexi}[MPa]$	$t_{arrival}[\mu s]$
Al (back)	10.4	10	3.0	3.0
(front)	3.4	8	14.0	1.0
Cu (top)	2.0	7.8	10.0	0.2
Fe (front)	3.0	6.3	6.0	0.8
Pb (front)	3.2	8	9.0	0.7

Table 4.10: The pressures obtained from the PVDF sensors as a response to the stress waves. The number of particles of the ion beam pulse in the corresponding shot and the distance between the sensor and the Bragg peak are given as well, for each type of target.

4.7 Time-resolved spectroscopic investigations of beam-cryogenic crystal interaction

4.7.1 Spectroscopic results in visible range

Time-resolved spectra in the visible range were obtained during an experiment with an $^{40}Ar^{11+}$ ion beam, with a particle energy of 300 AMeV and 0.7 μs long pulses containing around 5.5×10^{10} ions. The targets were Xe cryogenic crystals of 8 mm length, which is smaller than the stopping range of the ion beam, so that an almost uniform deposition of energy in the heated volume is assumed. The measurements were done using a Czerny-Turner grating spectrometer (Jarrel-Ash Monospec 27) with a 275 mm focal length and f/3.8 aperture. A 150 groove/mm plane grating was installed and the apparatus line width of 3.5 nm for a 20 μm entrance slit was determined from a Hg calibration lamp. The blaze wavelength of the spectrometer is at 450 nm, with a strong fall-off of the intensity at around 400 nm. In the scope of a time-resolved detection, a streak camera (HAMAMATSU C280) operated in the 5 μs streak time mode was focused onto the focal plane of the spectrometer. The streak slit determined a time resolution of 200 ns. In order to collect more light from the target, a lens with 90 mm focal length imaged the crystal on the entrance slit of the spectrometer. The whole system was aligned on one of the 45° ports of the target chamber (see figure 3.5 from section 3.4) so that it could acquire all the light emitted from a distance between 1 and 3 cm away from the plasma lens. The cut-off wavelength of the vacuum window of the chamber port, through which the measurements were performed, and the grating limit are situated at 350 nm.

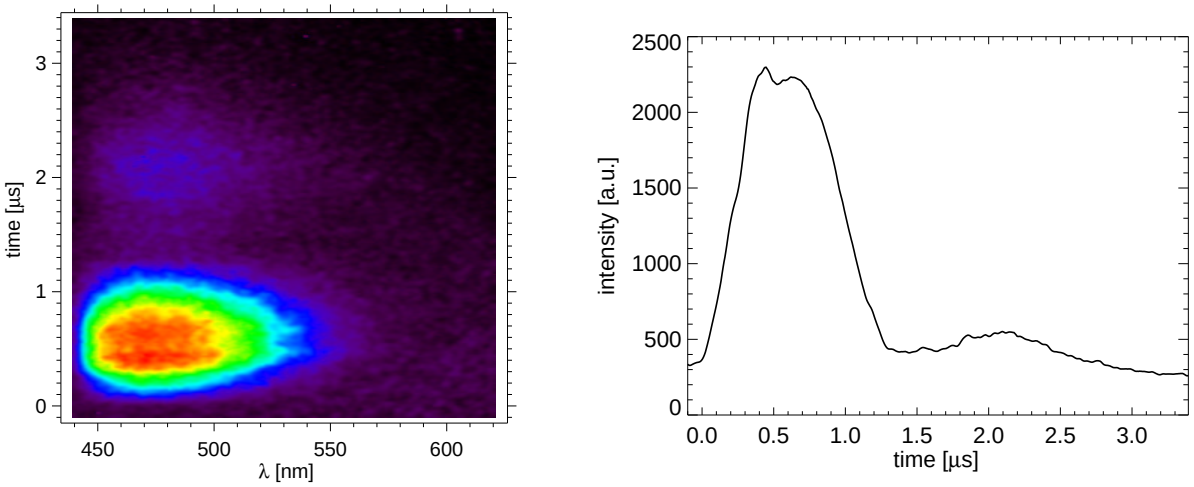

(a) (b)

Figure 4.42: (a) Streak image of a time-resolved spectrum in the 400 nm to 600 nm range from a Xe crystal; (b) profile of the same Xe crystal light emission, integrated over 10 nm.

Figure 4.42 shows a recorded time-resolved spectrum of the radiation emitted by the Xe crystal. In the work of M. Dornik an emission identified as the third continuum of the Xe was observed [Dor96], which has a maximum at 270 nm and a second less pronounced

maximum at 370 nm. In the recorded streak image from the present experiment, the maximum of the observed emission is around 480 nm, due to the increased sensitivity of the spectrometer-camera system in this region. Limitations imposed by the system did not allow measurements below 400 nm. The third continuum of Xe originates from molecular transitions which are explained by different hypotheses in the literature. It is believed, on one hand, that double-ionized molecule transitions $Xe_2^{++} \rightarrow 2Xe^+ + h\nu$ are responsible for this emission [Lan88]. Other works [Bro67, Huf62] claim that the third continuum of Xe is a result of transitions of singly ionized molecules, and a good agreement between experiment and theory was found by Amirov [Ami94]. The emission observed is caused by the third continuum and lasts during the entire pulse duration. After the beam pulse it is followed by a much less intense broad band emission. The causes of the latter were not identified yet, due to insufficient experimental data. The first bright emission reproduces very well the ion beam pulse and it was previously recorded in experiments performed at HHT [Dor96], but time integrated. Both emissions are plotted together in figure 4.43.

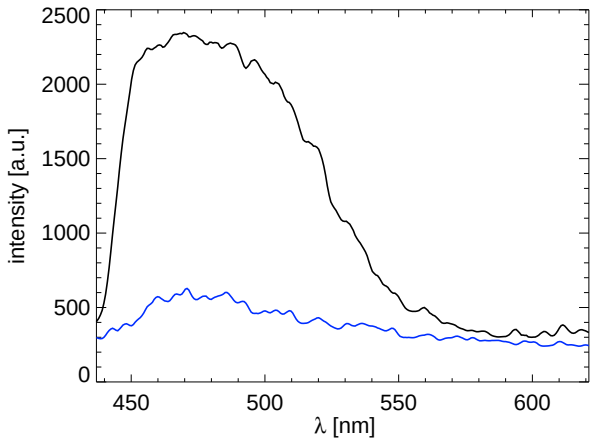

Figure 4.43: The Xe crystal emission (black) during the beam and the low emission (blue) which follows it after the ion beam pulse. The intensity in a.u. was plotted versus the wavelength in nm.

4.7.2 Spectroscopic results in the VUV range

New informations about the temporal evolution of the Xe crystal emission in the vacuum-ultraviolet region were gathered from an experiment with $^{18}O^{8+}$ ion beam (200 AMeV particle energy, 5×10^{10} particles contained in a bunch of 1 μs duration). The spectra were recorded using a Seya-Namioka monochromator (ACTON RESEARCH CORPORATION VM-507) with a 2400 grooves/mm concave grating and 0.2 m focal length. A microchannel plate (MCP) is placed in the focal plane, so that the VUV radiation is converted into visible light that can be then directly visualized by a faster shutter camera (PCO DICAM PRO). The MCP is CsI coated and for the time-resolved measurements was used in a pulsed mode, with a gating of 150 ns. The monochromator was mounted at 45° to the beam axis, directly connected to the target chamber. Since the monochromator and the MCP have to work in good vacuum conditions, a separation from the target chamber during the shots has to be ensured. The increase in pressure is usually caused by the expulsed matter from the target and this can also damage the grating of the

monochromator. The measurements were effectuated at pressures in the order of 1.5×10^{-5} torr, achieved by a turbo-molecular pump which is attached permanently to the case of the monochromator. Thus the high absorption in air of the VUV radiation is avoided as well. To prevent the rise of the pressure inside the monochromator during the heating of the target by the ion beam, a MgF_2 window was mounted in front of its entrance slit. The cut-off wavelength for this material is at around 120 nm, and the limitation in sensitivity of the MCP lies at around 190 nm. The Bragg peak range was not included in the 8 mm long target, and therefore the energy deposition along the target is almost uniform. Several shots were performed with an unfocused beam (no plasma lens) and few with focused beam for comparisons.

The excimer emission in the VUV range is of great importance for characterization of heated rare gas crystals by heavy ion beam. From the beam energy fractions of more than 20% can be converted into radiation. The conditions created within the crystal are favorable to formation of the so-called self trapped excitons [Sch85] which are molecular-like states in the crystal lattice emitting a radiation very similar to the excimer radiation of the gas phase. They form in very short times (of around 10 ps or less), much shorter than their lifetimes (which can be between 1 ns and 100 ns) [Bus88]. During the heating of the crystal, excimer molecules are formed and excited on these meta-stable states $^1\Sigma_u^+$ and $^3\Sigma_u^+$ from where they decay in the unstable ground state $^1\Sigma_g^+$. The resulting emission has a maximum at 172 nm known as the 2.continuum of the Xe_2^* excimer and it is schematically represented in figure 4.44. More details about the excimer emission can be found in [Bus93, Dor96, Rho84].

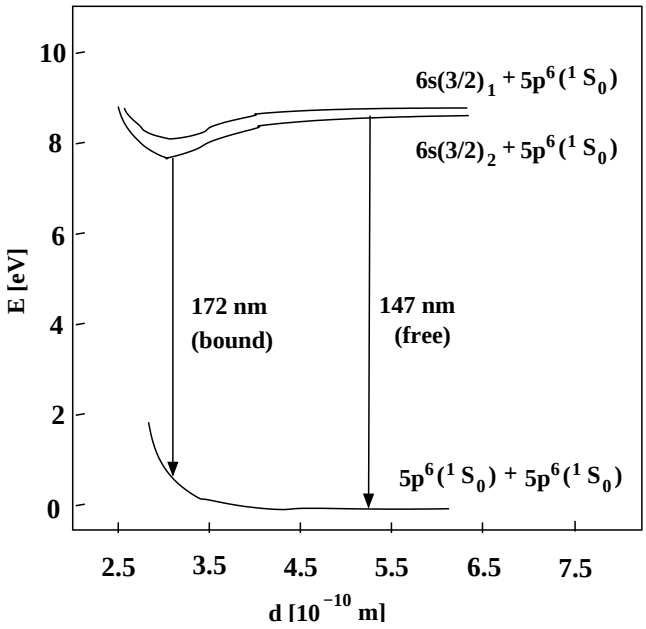

Figure 4.44: The excimer transition scheme for the Xe_2^* molecule. At 172 nm is represented the 2. continuum of the Xe excimer molecule and at 147 nm the lowest resonance line of the atomic Xe.

The results of the measurements consisted in recordings of a spectrum of the Xe excimer molecule with an emission maximum at 170 nm followed by a maximum at 176 nm. The latter was identified as the 2.continuum of the xenon excimers, which is often measured at wavelength shifted from 172 nm, between 164.4 nm [Dos82] and 175.6 nm [Ket79]. The two maxima appear also in the work of M. Dornik, recorded previously in

an experiment at HHT with Ar ions at 300 AMeV, but an explanation of the second peak was difficult to find, because the spectra were time integrated. The assumption from the same work [Dor96] was that the maximum at 170 nm is attributed to a solid state and the maximum at 176 nm to a fluid phase reached by the crystal during the ion beam heating. A time-integrated spectrum obtained in this experiment with O ions is very similar to the one obtained in the cited work (see figure 4.45).

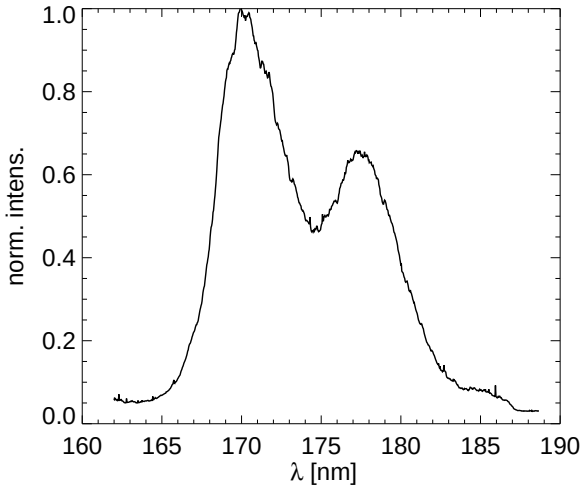

Figure 4.45:

In the present case, the time-resolved measurements showed that the maximum attributed to the fluid state appears actually first. It is assumed then that the 176 nm maximum of the xenon excimer emission is shifting towards lower wavelengths (to 170 nm) at higher power densities due to generation of free excitons at later times. At the beginning of the pulse, the energy of the ions is sufficiently high to form the excimer molecules which emit the radiation centered at 176 nm. As the energy deposition and number of ions in the pulse increase, at some later times, the binding energy of the xenon crystal molecules is surmounted and a large number of excitons released from the crystal lattice along the beam path [Wie01, Dew01]. In fact, since the binding energies of rare gas crystals are not too high, this process occurs around 50 ns or less after the emission of the bound molecules. The intensity of the free excitons radiation is considerably higher than that of the bound molecules, as the spectra at different times from figure 4.46(b) show. In all these shots the beam was not focused by the plasma lens. It was observed that the situation in which the released excimers emit at early times can occur about the beginning of the ion beam pulse if the beam is focused (figure 4.47).

Although the time-resolved measurements at different ion beam energy densities (by focusing or not the beam) showed a plausible explanation of the xenon excimer emissions, further experimental improvements - such as spatial resolution and absolute intensity determinations - supported by theoretical simulations are required to elucidate the case.

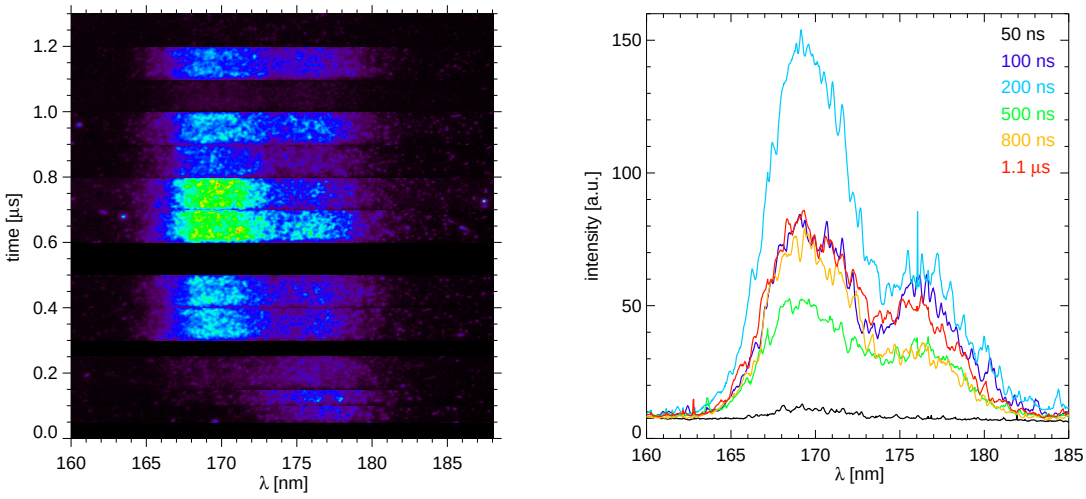

(a) (b)

Figure 4.46: (a) Sequence of pictures of the VUV spectra recorded in different shots, arranged along a time axis showing the delay related to the ion beam pulse. The radiation is emitted during the entire beam duration, which was always the same. There were variations in the ion beam intensity from shot to shot. (b) Spectral profiles at different times, showing a more intense maximum appearing at a shifted wavelength of around 170 nm.

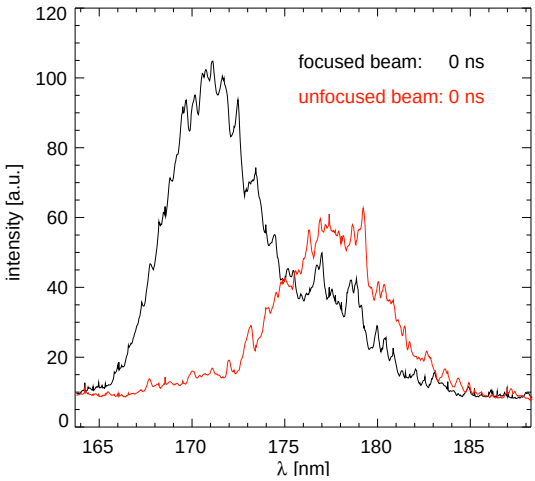

Figure 4.47: Spectral profiles of the Xe excimer radiation, recorded at the beginning of the beam pulse with focused beam (the higher peak) and unfocused beam.

Chapter 5

Conclusions

Experimental investigations on solid matter response to the action of intense heavy ion beams were performed using several diagnostic techniques. In this framework two processes were of main interest, namely the heating of the solid matter by the heavy ion beams, studied by backlighting shadowgraphy as well as time-resolved spectroscopy in the visible and VUV ranges, and the low entropy compression of matter by the generated shock waves. The latter was studied using a schlieren imaging technique, which is especially suited to visualize shock fronts and to measure shock velocities. For these measurements multilayered targets were used, composed of a metallic absorber and a transparent medium (plexiglass) for diagnostics. Quantitative density measurements were achieved from interferometry performed with a Mach-Zehnder device , and cross-checked by a direct laser deflection diagnostics. Pressures were also measured by calibrated PVDF transducers implemented in the targets at the rear side of the absorbent and at the end of the plexiglass block in order to gain informations about the attenuation of the shock.

5.1 Target heating by heavy ion beams

Besides lead targets, cryogenic rare gas crystals (Xe and Ne) were investigated by backlighting shadowgrapy. The target geometries were configured so that the Bragg peak position could be located either within the target (sub-range target), causing a nonuniform energy deposition along the beam axis, or well outside the target (super-range targets) leading to a very homogeneous energy deposition profile. For the sub-ranged lead targets, the matter jets expanded with the same velocity from both free surfaces of the target in the beam direction and opposite to it. A value of about 210 m/s was measured at the beginning of the expansion, decreasing after 10 μs to 147 m/s. For the Kr ion beam and super-ranged targets the expansion velocity, reaching up to 220 m/s close to the Bragg peak region was higher than the axial velocity of the expansion from the front side of the target, which was of 110 m/s. The matter hydrodynamics for both super-and sub-ranged cryogenic rare gas crystals rendered a behavior which proved to be independent on the range. Similar velocities of the matter expanding from both free surfaces of the target were measured. In the case of a sub-ranged Xe crystal heated by a Kr ion beam with 300 AMeV particle energy the expulsed matter velocity was 350 m/s in both directions, decreasing only after 20 μs. A U ion beam with 300 AMeV particle energy interacting with a super-ranged Ne crystal caused the expansion of matter with a velocity of 470 m/s in both directions, also. It was deduced that a uniform heating of the crystal occurred, even for the targets where the Bragg peak region was initially situated inside the target

volume. Due to the hydrodynamic motion of the matter during the heating process, a shift of the Bragg peak took place, which in the case of crystals exceeded the target range. The phenomenon presents interest in both experimental and theoretical studies of cooling processes which lower the ion beam energy deposition. Therefore the results obtained from the backlighting shadowgraphy measurements constitute important benchmarks for the simulation codes used in understanding the interaction between ion beams and matter.

Another cooling process which occurs during the bulk heating of matter is the radiative transport of the ion beam energy. The time-resolved spectroscopic measurements performed in both the visible and VUV range showed that a considerable fraction from the ion beam energy is converted into radiation, although no quantitative measurements were obtained. In the visible range a spectrum emitted by a Xe cryogenic crystal heated by an Ar ion beam with 300 AMeV was recorded by a streak camera providing a time resolution of 200 ns. The emission was identified as the third continuum of Xe, caused most probably by the transitions of singly ionized Xe molecules, according to works reported elsewhere [Ami94]. The intense Xe spectrum, with a maximum at 250 nm was emitted during the entire pulse duration of the ion beam and was followed shortly after the 1.2 μs duration of the beam by a less intense thermal radiation lasting for about 1.5 μs. The thermal emission is useful in direct determinations of the brightness temperature of the target [Sto98]. The measurements in VUV were recorded with a time resolution of 150 ns in an experiment with O ions heating a Xe crystal. In a previous experiment [Dor96] the same emission spectra of Xe excimers were observed, with maxima at 170 nm and 176 nm. These measurements were time integrated and therefore the interpretation of the 176 nm maximum was difficult. It was only assumed at that time that the first maximum occurs while the crystal is in a solid state, before undergoing any phase transition, whereas the maximum centered at 176 nm would constitute the emission of xenon in a fluid state. The assumption was infirmed by the appearance of the 176 nm maximum prior to the maximum centered at 170 nm. The shifting of the second continuum, in this experiment found at 176 nm, towards lower wavelength can be explained by the formation of 'free' excimer molecules of xenon, released from the crystal lattice as the energy deposited by the beam reaches sufficiently high values to overcome the binding energy of the xenon molecules. The intensity of the free excitons emission increases as compared with the radiation emitted by the bounded molecules, since the power deposition of the ion beam rises in time. Both of the excitons bounded and released coexist and emit on the entire ion beam pulse duration. If the beam is focused by the plasma lens onto the crystal, the coexistence assumed above takes place basically from the beginning of the beam pulse, since the power deposition is much higher than in the unfocused beam case. Both maxima were observed at time 0 ns, the more pronounced one being at 170 nm and the lower one at 176 nm, as it would be expected at this very early time, if the enunciated hypothesis is correct.

5.2 Weak shock waves and matter cold compression

The work described hereby was mainly concentrated on defining and characterizing the shock waves generated by the pressures exerted on solid matter in the Bragg peak region. Previous experiments determined that an acoustic wave appears shortly after the entire power is deposited in metallic targets. The pressures measured in the shock front were in the range of GPa [Sto98]. The high current injector installation at the UNILAC lead to

higher intensities of the beam and triggered a new set of measurements of the parameters induced by the shock waves in solid matter at HHT. The committed heavy ion beams generated multiple weak shock waves with supersonic velocities and pressures of up to 100 kbar in metallic absorbents in which the beam was stopped, and above 5 kbar in compressible layers of low acoustic impedance materials affixed to the absorbent. The idea was to use the cryogenic crystals confined between metallic plates to study the EOS of shock-wave compressed matter at low temperatures, with relevance for future beam intensities in the phase transition studies. For the optical diagnostics presently engaged, the cryogenic gas crystals proved insufficiently transparent, therefore they were replaced by plexiglass where the observations of the shocks could be performed.

The dynamics of the generated shocks were visualized time resolved by 1- and 2-D dark-field schlieren. The images obtained displayed the multiple shock structure propagating into plexiglass with velocities above the sound speed which for plexiglass at standard conditions is of 2.6 km/s according to an EOS from Chernogolovka. For different absorber materials (Al, Cu, Fe or Pb) the values of the measured velocities and, consequently, the inferred pressures [Bao84], as well as the time history of the shocks, were different one from another, manifesting a dependence on the absorber material. Highest parameters were obtained for the targets with Al and Fe layers, from which waves propagating in plexiglass with velocities up to 4 km/s were obtained. The induced pressures in the plexiglass were higher than 1.4 GPa, according to the empirical data tables taken from literature. For confirmation and comparisons between different ion beam-target material combinations, several sets of schlieren measurements employing U, Kr and Au ion beams were done and all showed the presence of multiple shock waves. Section 4.2 summarizes the results from the Kr and Au beamtimes. Accurate comparisons between the four absorber materials were limited only by the variations in the ion beam pulse intensity from shot to shot, which could not be neglected. However, an overall conclusion is that the use of Al and Fe as stoppers for a Au ion beam eventuated in the highest values experimentally achieved for the shock velocities and pressures in plexiglass. The drawback of these materials is that they favor the creation of shocks with fronts characterized by smaller curvature radii than in the case of copper or lead. The spherical shocks attenuate faster than plane shocks and the effect rises with the decrease of the curvature radius of the front. In the experiment with the Au beam an improvement of the time resolution of the detection system, which was provided by a streak camera, allowed the determination of the shock propagation velocity in time, in the plexiglass region. The plot showed a much faster attenuation of the speed for the same two materials as absorbents, namely Al and Fe, than for Pb and Cu. Consequently, the pressure decreases faster and the compression of the plexiglass might be not efficient. The causes for the different 'shaping' of the shock front is assumed to be connected to the manner in which the material responds to the ion beam heating. For instance, the Pb absorbent reaches fast its melting temperature and the material disperses leaving a large so-called crater in the Bragg region. At the times when the shock wave forms, the pressure distribution acts as a large surface area 'piston'. The hollow Bragg regions in the Al or Fe absorbent are spatially restricted, exceeding slightly the ion beam diameter. Cross sections made in the used target absorbents confirmed the assumed features of the heated regions resulting at the Bragg peak locations, but further investigations are requisite for study of shock front modelling. In this experiment, the shock front was visualized two dimensionally by schlieren and the radial and longitudinal velocities of the shocks were measured and compared with the results given by the 1D streak pictures.

A second assumption regards the origin of the multiple shock waves, which was motivated by the similarity with the case of the intense shock waves developed by proton beam heating of solid matter [Bau96]. Due to the strong heating inside the target volume where the Bragg peak arises, the material suffers a phase transformation followed by a high increase in pressure and temperature. As the generated shock encounters the first interface with the plexiglass it reflects and returns to the Bragg region where a new interface is generated as result of the changing in the material properties. In lead and copper the melting temperature is reached and the metal becomes fluid. Multiple shocks following one another are thus produced by successive reverberations on the Bragg interface, better spatially defined in the case of aluminum and iron. This would also explain the difference in the time history for the cases of each target, i.e. for Al and Fe the incoming shocks in plexiglass are more frequent and at more constant time intervals. For these targets higher shock velocities, that means higher pressures are obtained after the first shock due to the multiple shock enhanced compression, as theoretically shown by the Hugoniot curve 2.3.

Numerical calculations were carried out by a 2D-hydrodynamic code BIG2 for the experiment with Kr ions and targets with Cu, Pb and Fe absorbents. A good agreement was found for the Cu and Pb targets, both in pressure and velocity of the shock. The maximum value of the pressure generated inside the absorbent, of about 70 kbar, resulted for Pb. The pictures 4.22 resulting from simulations showed the presence of a second compressive wave flowing into the plexiglass only for the target containing a Cu layer. As in the experiment, multiple reflections of the incoming waves on the interface with the Al confiner at the rear side of the target were observed, leading to an increase in pressure. This explained the enhanced intensity of the stripes representing the shock waves in some of the streak pictures from both Kr and Au beamtimes.

The density evaluations were achieved in an experiment with an U ion beam and same target materials, in similar geometries. An imaging interferometry technique was applied, together with an one beam-laser deflection method. The targets were supplied with pressure transducers implemented in between the layers - meaning after the absorber layer or after the plexiglass block. The two locations of the gauges served for evaluations of the shock attenuation on the range of the plexiglass range. Only in some cases the electrical signals could be analyzed in order to obtain the pressures. All three diagnostics signalized the presence of very weak waves, in the sound wave region. The highest velocity of wave propagation in plexiglass was measured for the target with an Al absorbent, around 2.9 ± 0.2 km/s and the lowest velocities were determined for the Cu and Pb absorbents, equal to the speed of sound of the plexiglass. Corresponding to these values, a maximum fringe shift of 0.8 yielded from the 2D interferograms recorded with a framing camera. A maximum fringe shift of 2.5 was obtained for a shot in a Pb-plexiglass target with an ion beam pulse containing around 1×10^9 particles and the density during compression reached the upper value recorded during this experiment. Generally, the plexiglass density increased slightly from the initial one, comparably for all targets, demonstrating a weak compression at least at early times (up to 1-1.5 μs after the beam pulse). In some cases, at later times the plexiglass became dispersive and due to the loss of transparency no information could be extracted. It is very probable that at the times when the reverberations of the shocks start, the compressive field undergoes an enhancement of density and pressure which reaches the limit where the plexiglass becomes opaque or dispersive to the laser light. From the pressure gauges signals unexpectedly low values resulted, which were most probably caused by the large surface of the transducers, inappropriate for accurate measurements of pressures carried by spherical shock fronts. It is also assumed

that the reflections of the stress wave on the interface with the gauge disturbed the wave transit. However, useful informations about the temporal evolution of the shocks and the large attenuation along the plexiglass range in the case of Al target could be extracted. The signals, as well as the interferometry and laser deflection were very sensitive to the presence of multiple shocks. A thorough inspection of all the results and wave profiles, correlated in time, lead to the conclusion that the intensity of the ion beam was not sufficient to create stronger shocks and the pressure increase at some point was due only to reflections on interfaces or wave collisions, as the simulations and schlieren measurements aforementioned pointed out.

Important issues, such as the target material selection from the point of view of acoustic impedances matching, as well as the geometry have to be carefully taken into account in configuring the optimal targets for shock experiments and in modelling more plane shock fronts. The diagnostic tools are also to be reconsidered for the regime of stronger shocks. For higher compression ratios measurements done by reflections on moving surfaces, e.g. VISAR methods or reflective interferometric techniques, are more appropriate. Schlieren can be applied as well, with special conditions for the laser power and wavelength fulfilled. More complex types of schlieren set-ups, such as the double-inclined slit method would probably prove more suitable for quantitative measurements of density gradients induced by the shock propagation through the probe, which can be a cryogenic crystal or a liquid cell. This method can be assisted by a two-beam laser deflection, a method which can provide informations at two distinct locations in the target simultaneously, enabling thus measurements of the shock velocity and arrival time, as well as the possibility to distinguish between rarefactive or compressive waves. In future experiments, the plexiglass will be replaced by cryogenic crystals for which the growing technology will be optimized in order to obtain pure, perfectly transparent crystals on which optical diagnostics and various imaging techniques can be successfully applied.

New perspectives are given by a planned upgrade of the GSI accelerator facility consisting in the construction of a larger synchrotron ring, a project which is currently under discussion [Gsi01]. For the Plasma Physics experiments a beam with 1 AGeV particle energy and an increased intensity by a factor of 1000 compared to the present parameters would be available. According to numerical simulations, power densities of several TW/g for beams focused to spots of around 2 mm and pressures in the Mbar ranges would result, enabling studies of phase transitions, i.e. creation of metallic hydrogen by low-entropy multiple shock compression and a new, unexplored regime of high-energy density in matter.

Bibliography

[Ahl80] S.P. Ahlen, Rev. Mod. Phys. **52**, (1) (1980)

[Ami94] A.Kh. Amirov, O.V. Korshunov and V.F. Chinnov, J. Phys. B **27**, 1753 (1994)

[And90] M.U. Anderson and R.A. Graham, Proceed. PVDF Shocksensor Workshop, Saint Louis,1 (1990)

[Arn88] R.C. Arnold and J. Meyer-ter-Vehn, Z-Phys.D-Atoms, Molecules and Clusters **9**, 65 (1988)

[Asa93] J.R. Asay and M. Shahinpoor: *High-Pressure Shock Compression of Solids*, Springer-Verlag, New York, Berlin, Heidelberg (1993)

[Ash68] N.W. Ashcroft, Phys. Rev. Lett. **21**, 1748 (1968)

[Ban99] R.O. Bangerter, Phil. Trans. R. Soc. Lond. A **357**, 575 (1999)

[Bao84] Bao-Ping Zhang and F. Mueller, High Temperatures-High Pressures **16**, 475 (1984)

[Bas92] M. Basko, Nuclear Fusion, **32** (9), 1515 (1992)

[Bau82] F.Bauer: *Behavior of Ferroelectric Ceramics and PVDF Polymers under Shock Loading*, AIP Conference Proceedings on Shock Waves in Condensed Matter, ed. W.J. Nellis, New York, 251 (1981/1982)

[Bau85] F.Bauer: *Metallurgical Applications of Shock Waves and High Strain Phenomena*, ed. M. Dekker, New York, 1071 (1985)

[Bau96] K. Baumung, H.J. Bluhm, B. Goel, P. Hoppé, H.U. Karow, D. Rusch, V.E. Fortov, G.I. Kanel, S.V. Razorenov, A.V. Utkin and O.Yu. Vorobiev, Laser and Particle Beams **14** (2), 181 (1996)

[Ber91] Julien Bergoz, Handbook of *Fast Current Transformer for Heavy Ion Fusion at GSI* (1991)

[Bog91] E. Boggasch, J. Jacoby, H. Wahl, K.-G. Dietrich, D.H.H. Hoffmann, W. Laux, M. Elfers, C.R. Haas, V.P. Dubenkov and A. A. Golubev, Phys. Rev. Lett. **66** (13), 1705 (1991)

[Bro67] B. Brocklehurst, Trans. Faraday Soc. **63**, 274 (1967)

[Bus93] B. Busch, Dissertation: *Optische Verstärkung in Xenon bei Anregung mit Schwerionenstrahlen*, University of Technology-München (1993)

[Bus88] B. Busch, A. Ulrich, W. Krötz and G. Ribitzki, Appl. Phys. Lett. **53**, 1172 (1988)

[DaS97] L.B. Da Silva et al., Phys. Rev. Lett. **78**, 483 (1997)

[Dec85] G. Decker, R. Deutsch, W. Kies and J. Rybach, Applied Optics **24** (6), 823 (1985)

[Dew01] E. Dewald, internal communications (2001)

[Dor96] M. Dornik, Dissertation: *Experimente zur schwerioneninduzierten Volumenheizung kryogener Edelgastargets*, University of Technology-Darmstadt (1996)

[Dos82] O. Dössel, Dissertation, University of Kiel (1982)

[Due00] U. Dürig, Appl. Phys. Lett. **76**, 1203 (2000)

[Ebe91] W. Ebeling, A. Förster, V.E. Fortov, V.K. Gryaznov and A.Ya. Polishchuk: *Thermophysical Properties of Hot Dense Plasmas*, Teubner (1991)

[Emr] *Methods of Experimental Physics*, vol.18, Part A, edited by R.J. Emrich- Part 2 by W. Merzkirch

[For96] V.E. Fortov, B. Goel, C.D. Munz, A.L. Ni, A.V. Shutov and O.Yu. Vorobiev, Nucl. Sci. Eng. **123**, 169 (1996)

[Fra92] K. Frank, O. Almen, P. Bickel, J. Christiansen, A. Görtler, W. Hartmann, C. Kozlik, A. Linsenmeyer, H. Loscher, F. Peter, A. Schwander and R. Stark, Proceedings of the IEEE **80** (6), 958 (1992)

[Fun99] U.N.Funk, Dissertation: *Aufbau und erster Einsatz einer Kryoanlage zur Herstellung von Wasserstofftargets für Experimente mit Schwerionenstrahl*, University of Erlangen-Nürnberg (1999)

[Gei97] M. Geissel, Diplomarbeit, Technische Hochschule-Darmstadt (1997)

[Gol98] A. Golubev, M. Basko, A. Fertman, A. Kozodaev, N. Mesheryakov, B. Sharkov, A. Vishnevskiy, V. Fortov, M. Kulish, V. Gryaznov, V. Mintsev, E. Golubev, A. Pukhov, V. Smirnov, U. Funk, S. Stöwe, M. Stetter, H.P. Flierl, D.H.H. Hoffmann, J. Jacoby and I. Iosilevski, Phys. Rev. E **57** (3), 3336 (1998)

[Gra87] R.A. Graham, L.M. Lee and F. Bauer: *Response of Bauer Piezoelectric Polymer Stress gauges (PVDF) to Shock Loading*, Proceedings of the Conference on Shock Waves in Condensed Matter, North Holland Physics Publ., Amsterdam, 619 (1988)

[Gri93] G. Grieger and I. Milch, Phys. Bl. **49** (11), 1001 (1993)

[Gsi01] Conceptual Design Report: *An International Accelerator Facility for Beams of Ions and Antiprotons*, GSI, Nov. 2001

[Haw81] R.S. Hawke, A.L. Brooks, A.C. Mitchell, C.M. Fowler, D.R. Peterson and J.W. Shaner, AIP Conference Proceedings on Shockwaves in Condensed Matter **78** (1), 179, ed. W.J. Nellis (1982)

[Hof90] D.H.H. Hoffmann, K. Weyrich, H. Wahl, D. Gardes, R. Bimbot and C. Fleurier, Phys. Rev. A **42** (2313) (1990)

[Hog92] W.J. Hogan, R. Bangerter and G.L. Kulcinski, 'Energy from inertial fusion', Physics Today **42** (sept. 1992)

[Huf62] R.E. Huffman et al., J. Opt. Soc. Am. **52**, 851 (1962)

[Ich82] S. Ichimaru, Rev. Mod. Phys. **54** (4), 1017 (1982)

[Jac90] J. Jacoby, D.H.H. Hoffmann, R.W. Müler, K. Mahrt-Olt, R.C. Arnold, V. Schneider and J. Maruhn, Phys. Rev. Lett. **65**, 2007 (1990)

[Jac02] J. Jacoby, internal communications 2002

[Jah71] F.C. Jahoda, G.A. Sawyer: *Methods of Experimental Physics*, Vol. 9B (R.H. Lovberg and H.R. Griem, eds.), Academic Press, New York (1971)

[Ket79] J.W. Keto, R.E. Gleason and F.K. Soley, J.Chem.Phys. **71**, 2676 (1979)

[Lan88] H. Langhoff, Opt. Commun. **68**, 31 (1988)

[Lau93] W. Laux, Dissertation, Ruprecht-Karls University of Heidelberg (1993)

[Law67] J.D. Lawson:*Some Criteria for a Power Producing Thermonuclear Reactor*, Proceedings of the Physical Society B70, 6 (1967)

[Loe94] T. Löwer and R. Sigel, Phys. Rev. Lett. **72**, 3186 (1994)

[Lom94] I. Lomonosov, A.V. Bushman and V.E. Fortov, High-Pressure Science and Technology, AIP Press, New York, part I, Eds. S.C. Schmidth et al., 117 (1994)

[Lov] *Methods of Experimental Physics*, vol.9, Part B, edited by R.H. Lovberg and H.R. Griem- Part 11 by F.C. Jahoda and G.A. Sawyer

[Lun99] S.M. Lund, O. Boine-Frankenheim, G. Franchetti, I. Hoffmann and P. Spiller, Proceed. PAC Conf., New York, 1785 (1999)

[Lyn91] G.R. Lynch and O.I. Dahl, Nucl. Instr. Meth. B **58**, 6 (1991)

[Mao94] H. Mao and R. Hemley, Rev. Mod. Phys. **66**, 671 (1994)

[McM60] H.O. McMahon and W.E. Gifford, Repts. Prog. Phys. **26**, 269 (1963)

[McQ70] R.G. McQueen et al., *High Velocity Impact Phenomena*, ed. R. Kinslow, Academic Press, New York (1970)

[Mit91] A.C. Mitchell, J. Appl. Phys. **69** (5), 2981 (1991)

[Msc99] M. Steck, K. Blasche, H. Eickhoff, B. Franczak, B. Franzke, L. Gröning and T. Winkler: *Improved performance of the GSI heavy ion accelerator complex with cooled synchrotron beams*, Proceed. PAC Conf., New York (1999)

[Mst99] M. Steck, L. Gröning, K. Blasche, H. Eickhoff, B. Franczak, B. Franzke, T. Winkler and V.V. Parkhomchuk: *Electron cooling assisted beam accumulation in the heavy ion synchrotron SIS by repeated multiturn injection*, Proceed. PAC Conf., New York (1999)

[Neu95] U. Neuner, Dissertation: *Die Plasmalinse zur Feinfokussierung hochenergetischer Schwerionenstrahl*, University of Erlangen-Nürnberg (1995)

[Nol86] R. Noll, C.R. Hass, B. Weikl and G. Herziger, Appl. Optics **25** (5), 769 (1986)

[Ohi76] H. Ohigashi, Journal of Applied Physics **47** (3) (1976)

[Pai76] H.J. Pain: *The Physics of Vibrations and Waves*, 2nd edition, Wiley, New York (1976)

[Pet91] Th. Peter and J. Meyer-ter-Vehn, Phys. Rev. A **43** (4), 1998 (1991)

[Pin89] K. Pinkau, U. Schumacher and G.H. Wolf, Phys. Bl. **45** (2), 41 (1989)

[Pre92] W.H. Press, S.A. Teukolsky, W.T. Vetterling and B. Flannery: *Numerical Recipes, the art of scientific computing*, 2nd Edition, Cambridge University Press (1992)

[Red01] R. Redmer, Phys. Bl. **57** (6), 25 (2001)

[Rho84] C.R. Rhodes: *Excimer Lasers*, Springer, Berlin (1994)

[Rot97] M. Roth, Dissertation: *Experimentelle Bestimmung des Energieverlustes schwerer Ionen in laseerzeugten Plasmen*, University of Technology-Darmstadt (1997)

[Sch85] N. Schwentner, E.E. Koch and J. Jortner: *Electronic Excitations in Condensed Rare Gases*, Springer Tracts in Modern Phys. 107, Springer, Berlin (1985)

[Sch01] T. Schlegel, internal communication - 2001

[SES83] SESAME Report on the Los Alamos Equation-Of-State Library, Report no.LALP-83-4, T4 Group LANL, Los Alamos (unpublished) (1983)

[Seg65] E. Segre: *Nuclei and Particles*, Ch. 2, Benjamin: New York (1965)

[She59] F.A. Baum, K.P. Stanyukovich and B.I. Shekhter; *Explosion Physics*, Fizmatgiz, Moscow (1959)

[Spi94] P. Spiller, Dissertation: *Untersuchungen zum transport und zur Fokussierung intensiver, hochenergetischer Schwerionenstrahlen zur Erzeugung hoher Energiedichte in Materie*, University of Giessen (1994)

[Spi99] P. Spiller, K. Blasche, O. Boine-Frankenheim, M. Emmerling, B. Franczak, I. Hoffmann, S. Lund and U. Ratzinger, Proceed. PAC, New York (1999)

[Ste93] M. Stetter, J. Christiansen, U. Neuner, S. Stöwe, R. Tkotz, T. Wagner, E. Boggasch, A. Tauschwitz, D.H.H. Hoffmann and P. Spiller, Il Nuovo Cimento **106**A (11) 1725 (1993)

[Ste96] M. Stetter, U. Neuner, S. Stöwe, M. Dornik, D.H.H. Hoffmann, R. Kowalewicz, P. Spiller and A. Tauschwitz, Fus. Eng. Des. **32-33**, 503 (1996)

[Sto94] S. Stöwe, Diplomarbeit, University of Erlangen-Nürnberg (1994)

[Sto98] S. Stöwe, Dissertation: *Schwerioneninduzierte Hydrodynamik in Bleitargets*, University of Erlangen-Nürnberg (1998)

[Tah00] N.A. Tahir, A. Kozyreva, A. Shutov, P. Spiller and D.H.H. Hoffmann, Phys. Rev. E **61** (2), 1975 (2000)

[Tah01] N.A. Tahir, D.H.H. Hoffmann, A. Kozyreva, A. Tauschwitz, A. Shutov, J.A. Maruhn, P. Spiller, U. Neuner, J. Jacoby, M. Roth, R. Bock, H. Juranek and R. Redmer, Phys. Rev. E **63**, 016402-1 (2001)

[Tah01b] N.A. Tahir, A. Kozyreva, P. Spiller, D.H.H. Hoffmann and A. Shutov, Phys. Plasmas **8** (2), 611 (2001)

[Tau93] A. Tauschwitz, Dissertation: *Die stromtragende Plasmalinse, eine effektive Möglichkeit zur Fokussierung hochenergetischer Teilchenstrahlen*, Technische Hochschule-Darmstadt (1993)

[Var01] D. Varentsov, P. Spiller, U.N. Funk, D.H.H. Hoffmann, A. Kozyreva, N.A. Tahir, C. Constantin, E. Dewald, J. Jacoby, U. Neuner, S. Udrea and R. Bock, Nucl. Instr. Meth. B **174**, 215 (2001)

[Wei96] S.T. Weir, A.C. Mitchell and W.J. Nellis, Phys. Rev. Lett. **76** (11) (1996)

[Wes96] J. Wesson: *Tokamaks*, 2nd edition, The Oxford engineering science series; 48, Oxford University Press, Oxford (1996)

[Wet96] H. Wetzler, Dissertation: *Dichtediagnostik an einem z-Pinch-Argonplasma durch Emissionspektroscopie und hochenergetische Schwerionenstrahlen*, University of Technology-Darmstadt (1996)

[Wie01] J. Wieser, A. Ulrich, E. Dewald: internal communications

[Wig35] E. Wigner and H.B. Huntington, J. Chem. Phys. **3**, 764 (1935)

[Wol95] B. Wolf: *Handbook of Ion Sources*, edited by Bernhard Wolf, CRC Press (1995)

[Zel67] Ya.B. Zel'dovich, Yu.P. Raizer, *Physics of Shock Waves and High-Temperature Hydrodynamic Phenomena*, vol. II, Academic Press, New York (1967)

[Zie96] J.F. Ziegler, J.P. Biersack and U. Littmark: *The Stopping and Ranges of Ions in Solids*, Pergamon, New York (1996)

Acknowledgements

At the end of my work, some old memories about my first contact with GSI came into my mind. It is still vivid the sensation that I got when entering the ESR hall, where the HHT cave is located, during the visiting tour patiently guided by my colleagues, Matthias Geissel and Stefan Stöwe - who were so nice to answer my questions. I was deeply impressed and I had a feeling that something very special is going on there. After more than 3 years spent at GSI, with Plasma Physics Group, I still believe this. And I am grateful to all the people that gave me the opportunity to participate in the very interesting exploration of properties of dense plasmas generated by the matter interaction with heavy ion beams.

First of all, I would like to thank to Professor Dr. Dr. h.c. Dieter H.H. Hoffmann, for he made everything happening. For the wonderful guidance, care and help offered during my work, which are of great value to me. For the encouragements and advices, and, most of all, for keeping alive my passion for physics. Herzlichen Dank für alles!

I would also like to thank:

To Dr. Eduard Dewald, for all the help, guidance in my formation as a physicist and fruitful discussions, for his tremendous enthusiasm which enriched the progress of my work and, not at least, for the wonderful, and precious friendship.

To Christoph Niemann for participating during our experiments and for his unconditioned support during my whole work, for the encouragements and for helping me so much in the analyses of the results.

To Serban Udrea, for his helping hand in so many, various situations, for sharing the good or bad moments during the long, long beamtime nights, for all the practical, as well as moral support at work and for his wonderful friendship.

To Joachim Jacoby, for being always a helpful coordinator and guide, for the very fruitful discussions and corrections to papers and to my thesis and for the help during my work.

To the entire HHT team, for the interesting things that I have learned, the great help in my experiments and the wonderful time spent together: Dmitry Varentsov, Dr. Ulrich Neuner, Dr. Ulrich Funk, Dr. Jochen Wieser, Dr. Stefan Stöwe.

To Dr. Naeem Tahir, for the useful discussions, for the simulations of our experiments, for the very helpful corrections to my paper and to my thesis.

To Dr. Theodor Schlegel, for his interest in my work, for the large amount of time spent to simulate and to help me understand the experimental data and the physics behind, for corrections to papers and all the information he gave me.

To Dr. Alexander Shutov, for the new things I have learned during our nice collaboration, for his hard work to simulate the experiments, which I deeply appreciate.

To Anna Kozyreva for her theoretical support and work on simulations and for helping me with the German homeworks.

To Dr. Peter Spiller, for the good suggestions he has made, for the interesting discussions, for all the nicely aligned beams and the support to my work.

To Dipl.-Ing. Henry Wahl, for offering me technical support and advices when I needed them mostly!

To the entire Plasma Physics Group, for being wonderful colleagues, for all the support and advices, and for everything else that I have not mentioned (not due to a lack of gratitude)!

I am also very grateful to our collaborators, Dr. M. Kulish, Dr. A. Golubev, Dr. V. Turtikov and the entire russian team for the very interesting discussions and ideas, and for all their unconditioned, friendly help during the beamtimes.

I could not have performed my experiments on time, or at all, without the help of the TU Workshop, as well as the GSI Workshop people, to whom I am very thankful for the good work in making the targets, of such great importance for all the work described hereby.

... At last, not least, my very special thanks to Mom and Dad!

Curriculum Vitae

Name:	**Carmen Georgeta Constantin**
Birth date / place:	February 7, 1972 / New York City, USA
Citizenship:	Romanian, American

EDUCATIONAL PROFILE:

since Aug. 98:	PhD student at the University of Technology, Darmstadt and the Gesellschaft für Schwerionenforschung, Darmstadt, Germany
1990-1996:	B.Sc./M.Sc. at the Faculty of Physics, University of Bucharest, Romania Jun.1996: Diploma work at the Institute of Astronomy, Bucharest, Romania Thesis: *'Spectroscopic Effects of Mass Transfer Process in Stellar Close Binary Systems '* Advisors: Prof. Dr. Mircea Rusu and Dr. Al. Dumitrescu
1986-1990:	High-School for Mathematics and Physics Gh. Lazar, Bucharest, Romania
1978-1986:	primary and secondary school in Bucharest

Hiermit erkläre ich, daß ich die Arbeit selbständig und nur mit den angegebenen Hilfsmitteln angefertigt und nicht schon früher eine Promotion versucht habe.

7. Februar 2002 Carmen Constantin